NEXT GENERATION APC ANALOGS FOR MULTIMODALITY IMAGING AND THERAPY OF CANCER

By

Ray Zhang

A dissertation submitted in partial fulfillment

of the requirements for the degree of

Doctor of Philosophy

(Cellular and Molecular Biology)

At the

UNIVERSITY OF WISCONSIN – MADISON

2017

Date of final oral examination: 5/26/17

The dissertation is approved by the following members of the Final Oral Committee:

Jamey P. Weichert, Associate Professor, Department of Radiology

John S. Kuo, Associate Professor, Department of Neurological Surgery

Ronald R. Burnette, Professor, Department of Pharmaceutical Sciences

Amy M. Fowler, Assistant Professor, Department of Radiology

Anjon Audhya, Associate Professor, Department of Molecular and Cellular Pharmacology

Scott B. Reeder, Professor, Department of Radiology

ACKNOWLEDGEMENTS

It has been a great pleasure and learning experience working in the labs of Prof. Jamey Weichert and Prof. John Kuo the past four years. Your advice, guidance, and support have furthered by professional development as a young budding graduate of the sciences. You guys have been invaluable resources and mentors that have encouraged and inspired me to pursue scientific inquiry. You have taught me essential skills including critical thinking, experimental design, and perseverance that have laid the foundation for my professional life. I also have had the pleasure of knowing Prof. Jamey Weichert and Prof. John Kuo on a more personal basis, and you have also taught me important lessons outside the laboratory environment that are equally as important as I strive to be a future role model and mentor myself.

I would also like to extend my gratitude to the members of my committee, Dr. Ronald Burnette, Dr. Anjon Audhya, Dr. Amy Fowler, and Dr. Scott Reeder, who have also been invaluable assets for all my thesis work and my professional development. You are all role models that I highly respect and look up to.

I would like thank my collaborators and colleagues who have helped me along the way, and whom I've had gotten to know very well these past four years. Professionally, they have been vital resources, and I could not have elevated my work to the level that it is now without your help. I would like to acknowledge Anatoly Pinchuk, Reinier Hernandez, Joseph Grudzinski, Paul Clark, Justin Jeffrey, Tej Mehta, Ashley Weichmann, Christina Brunquell, Alan McMillan, Kelli Hellenbrand, Alex Schroeder, Marc Longino, and Maria Banach. You guys are all amazing researchers, and I cannot have done it without you.

Last but not least, I would like to thank my family and close friends for their support throughout this career path. To my parents, for their kind support and making me the person who I am today, and my little brother Daniel, who has been always there to cheer me on. To all of my friends who have been supportive of my journey and have helped me through

tough times. To all my colleagues and administrative staff of the MD/PhD program, who have helped me through 6 of these long 8 years here at UW.

ABSTRACT

Small molecule alkylphosphocholine analogs have shown great potential as diagnostic PET agents and targeted radiotherapy agents for many different types of cancers. The first generation radioidonated APCs displayed prolonged tumor-selective retention in over 55 *in vivo* rodent and human cancer and cancer stem cell models. Remarkably substitution of the radioiodone with bulkier fluorophores did not affect the tumor-targeting properties of these APC analogs. Due to this initial observation, we proceeded to synthesize and validate next generation APC analogs for multi-modality imaging and therapy of cancer through substitution of bulkier substituents in place of the radioiodine. As part of the thesis work, we have strove to understand how the structure of these compounds affect many of their *in vivo* properties (Chapter 2). We have synthesized and validated near-infrared fluorescent APCs (Chapter 3), dual modality PET/fluorescent APCs (Chapter 3), and APC chelates (Chapter 4) that greatly extend the multimodality imaging and therapy potential of these APC analogs. Importantly, we have shown that the broad uptake and retention for numerous cancer types of these new APC analogs are maintained in these new APC analogs. Through continued synthesis, validation, and interrogation of APCs' mechanism of cancer targeting, we are realizing the potential of APCs as a platform of cancer delivery.

LIST OF ABBREVIATIONS

APC	Alkylphosphocholine
FDG	Fluoodeoxyglucose
PET	Positron emission tomography
SPECT	Single photon emission computed tomography
GBM	Glioblastoma Multiforme
ADME	Absorption, distribution, metabolism, and excretion
BODIPY	Boron-dipyrromethene
IR775	Infrared 775 fluorophore
MR/MRI	Magnetic Resonance/Magnetic Resonance Imaging
DOTA	1,4,7,10-tetraazacyclododecane-1,4,7,10-tetraacetic acid
FDA	Food and Drug Administration
NIR/NIRF	Near-infrared/Near-infrared fluorescence
APL	Alkylphosopholipids
PK	Pharmacokinetics
PBS	Phosphate Buffered Saline
UV	Ultraviolet
RCSB	Research Collaboratory for Structural Bioinformatics
SEM	Standard error of the mean
logD	Partition coefficient at pH 7.4

EDTA	Ethylenediaminetetraacetic acid
ANOVA	Analysis of variance
HDL	High density lipoprotein
LDL	Low density lipoprotein
HSA	Human serum albumin
FA	Fatty acid
MRT	Mean residence time
AUC	Area under the curve
CL	Clearance
GTR	Gross total resection
CT	Computed tomography
FOV	Field of visualization
FGS	Fluorescence guided surgery
5-ALA	5-aminolevulinic acid
HRMS	High resolution mass spectrometry
PpIX	Protoporphyrin IX
GSC/CSC	Glioma stem cell/Cancer stem cell
DL	Dual-labeled
EPR	Enhanced permeability and retention
NCT	National clinical trial
TEM	Transmission electron microscopy

NOD/SCID	Nonobese diabetic/severe combined immunodeficient
Gd	Gadolinium
STEM	Scanning transimission electron microscopy
SPGR	Spoiled gradient
Dotarem	Gadoterate meglumine
Multihance	Gadobenate Dimeglumine
TRT	Targeted Radiotherapy
MALDI	Matrix-assisted Laser Desorption and Ionization

FIGURE AND TABLE LEGENDS

images of the animals at 48hr and 96 hr. Yellow arrows indicate tumor. (C) Biodistribution of ^{177}Lu in various organs at 48hr and 96 hr. (D) Tumor volumes days after injection of the single bolus dose. Data are mean tumor volumes ± SEM. P values for tumor growth curves determined by one-way repeated-measurement ANOVA.

TABLE OF CONTENTS

Chapter 1: Introduction

1.1 Previous Generation Alkylphosphocholine analogs for Molecular Imaging and Targeted Radiotherapy

^{124}I-NM404, ^{131}I-NM404 are related novel small molecule, cancer-targeting APC analogs. These APC analogs share a common targeting moiety that is selectively retained by tumor cells of many different histologies linked to a functional moiety fashioned for diagnostic imaging or therapy (Figure 1.1). The lead compound NM404 was selected from over 30 radioiodinated phospholipid ether analogs from 4 different structural classes including an APC class[1]. NM404 was initially exhibited the highest tumor signal to background ratio in rodent cancer models, and excellent *in vivo* stability against deiodination due to the positioning of the iodine on the aromatic ring[1]. APC derivatives localize to cellular and intracellular membranes via uptake into cholesterol-rich plasma membrane lipid raft domains overexpressed in cancer cells[2,3]. The relative deficiency of phospholipid catabolizing enzymes in tumor versus normal cells results in prolonged tumor retention, in contrast to APC clearance by normal tissues. APCs are being further evaluated in multiple early phase human clinical imaging and radiotherapy trials, after extensive testing and demonstration of prolonged selective retention in over 60 in vivo rodent and human cancers and cancer stem cell models[2,4,5]. Additionally, NM404 exhibits improved specificity for cancer and not inflammatory foci, in contrast to other agents such as fluorodeoxyglucose (FDG), which is often taken up by rapidly dividing cells in areas of inflammation and wound healing[2,6,7]. Currently, two radioinodinated NM404 analogs have recently undergone five multi-institutional human imaging and therapy clinical trials, – ^{124}I-NM404 for positron emission tomography (PET)

imaging, and ^{131}I-NM404 for therapy and single photon emission computed tomography (SPECT) imaging (NCTs?). Preliminary data from a multi-institutional Phase II trial for Glioblastoma Multiforme (GBM) imaging with ^{124}I-NM404 is currently being evaluated[4,5].

Due to the broad, selective, and specific uptake of NM404 in numerous types of cancers, and its small molecule cost and scalability, NM404 bears tremendous potential as a cancer delivery platform. However, unlike larger antibody-drug conjugates, small perturbations in structure of these small molecules can drastically affect its tumor-targeting properties, pharmacokinetics, and other "ADME" (absorption, distribution, metabolism, and excretion) properties. Therefore, in order to realize the full potential of APC compounds for cancer imaging and therapy, synthesis and validation of new APC analogs are necessary. To this end, we have developed and corroborated *in silico* models that predict the ADME characteristics of these small molecules in order to optimize these properties of newer APC analogs (Chapter 2).

1.2 Diapeutics in Personalized Medicine

"Theranostics" are defined as diagnostic tests that inform treatment choice and clinical outcome. To improve patient outcomes, theranostics would ideally be used in therapy decision-making to predict treatment efficacy and response, and change clinical management by avoiding unnecessary risks and associated costs of ineffective care[8,9]. Optimizing therapeutic efficacy and safety is especially warranted in treating primary brain tumors or brain metastases, where tumor cells are infiltrating or adjacent to vital functional brain tissue, and deleterious side effects carry significant morbidity and mortality. Therefore, theranostics can have transformative implications in managing brain tumor patients. APC analogs have a cancer-selective retention mechanism mediated by an

identical cancer-targeting chemical backbone, exhibit broad specificity for tumor cells in multimodal imaging and therapy, and could predict, inform, and monitor therapy outcomes[10].

While, theranostic strategies often rely on technologies and techniques that are radically different to inform clinical decisions, the identical tumor-targeting backbone of all three APC analogs confers a shared mechanism of uptake and retention, and a special subset of theranostic agents "diapeutics"[10]. Due to their identical uptake and retention mechanisms, ^{124}I-NM404 and its companion radioisotere ^{131}I-NM404 have the same pharmacological half-life, tissue biodistribution, and cancer-selective retention characteristics. This commonality ensures that the synergistic use of these agents reliably and specifically target the same cancer cells in diagnosis and staging, treatment planning and dosimetry, and potentially subsequent clinical follow-up and monitoring of treatment response.

To illustrate the power potential advantage of diapeutic agents, consider a patient with a brain malignancy: ^{124}I-NM404 is administered initially for whole body or global for initial diagnostic assessment of cancer lesion(s) and staging. Postoperative uptake of APC PET imaging tracer can be used to calculate personalized dosimetry for the targeted radiotherapy agent ^{131}I-NM404. Follow-up APC PET imaging may further inform patient management by through possibly detection of tumor recurrence. As this example demonstrates, due to the identical cancer-targeting mechanism of diapeutic APCs, this suite of APC analogs can be used at multiple clinical phases, potentially maximizing effectiveness and simultaneously minimizing complications during surgery and radiotherapy on a patient to patient basis.

However, the arsenal of APCs can be further expanded to improve and extend the diapeutic potential of APCs for cancer imaging and therapy. Only covalently-linked radioiodinated APC analogs have been synthesized and validated. Covalently-linked radioisoteres suffer from the drawback of expensive and laborious synthesis and labeling procedures, and relatively low abundance of radioisotopes (^{18}F, ^{15}O, ^{13}N, ^{11}C, iodine) that can be attached[11]. ^{124}I and ^{131}I were selected in order to match the decay half-life of the radioisotope with the biological half-life of the APC compound. Due to these limitations, other APC analogs such as chelatable APCs, and fluorescent APC analogs may extend the diapeutic potential of APC analogs in cancer imaging and therapy (Chapter 3 and 4).

1.3 New Generation APC Analogs for Multimodality Imaging and Therapy of Cancer

In order to broaden the application of APCs in diagnostic imaging and therapy of cancer, fluorescently labeled APC analogs by conjugating BODIPY (Boron-dipyrromethene) or a near-infrared fluorophore to the alkylphosphocholine backbone were first tested (Chapter 3). Remarkably, substitution of iodine with a large optically active functional groups (e.g. BODIPY, IR-775) does not alter APC's tumor selectivity[12]. IR775-1404 or 1502 demonstrated uptake and retention in orthotopic GBM models of human cancer, as well as breast, colon, and prostate cancer[13-15]. The fluorescently-active APC analogs can be used for real-time subcellular trafficking (BODIPY) and intraoperative margin detection (IR-775).

Due to the initial success of the next generation APC analogs, other APC analogs including dual-modality APCs, and APC chelates were synthesized and validated in order to extend the applications of APC analogs and further their diapeutic potential. The APC chelates represent a new versatile platform for multi-modality imaging and therapy, as

multiple radiometals for MR (Magnetic resonance) imaging, PET (^{64}Cu, ^{68}Ga, ^{86}Y, ^{89}Zr, ^{111}In), Single photon emission computed tomography (SPECT) and radiotherapy (^{90}Y, ^{177}Lu, ^{225}Ac, ^{213}Bi, ^{188}Re, ^{212}Pb) can be facilely chelated onto the APC. As a proof-of-concept, we synthesized a MR active agent Gd-DOTA-APC (1,4,7,10-tetraazacyclododecane-1,4,7,10-tetraacetic acid) for targeted MR imaging of cancer (Chapter 4). We demonstrate that other radiometals such as ^{64}Cu can be stably appended for diagnostic PET imaging. Such an approach can overcome the limintations of covalently-linked APC analogs such as relatively few radioisotopes and time-consuming synthesis and labeling procedures.

Chapter 2: In silico Modeling and Screening of APC Analogs

2A Introduction:

Drug binding to serum proteins impacts the rate of clearance and uptake into target tissues, as only the unbound drug is taken up metabolic or target tissues[16,17]. Consequently, a high affinity for plasma proteins may be beneficial or detrimental depending on the use of the drug. Very high binding affinity may be detrimental if there are off-target effects, as long systemic circulation may increase the exposure time and lead to dose-limiting toxicities such as myelosuppression commonly seen with long circulating antibody therapies[18-21]. Very low levels of binding may result in rapid clearance, and low levels of uptake in the target tissues.

The plasma binding properties of drugs are of vital importance because they affect the pharmacokinetic properties of the drugs such as rate of uptake and clearance, which in turn impacts the drugs' efficacy and safety. Even after demonstrating efficacy preclinically, only a small percentage of anticancer drugs (5%) become Food and Drug Administration (FDA) approved[22]. Non-optimal pharmacokinetic profiles are the main contributor to drug attrition (39%)[23,24]. Therefore, *in silico* modeling that is predictive of pharmacokinetic behavior based on chemical composition and physicochemical properties represents a powerful and economical approach to designing future analogs with more favorable characteristics[25-27]. Importantly, lead compound optimization of pharmacokinetic properties will significantly improve the successful development of these anticancer compounds[22]. *In silico* modeling can identify lead compounds more quickly than classical methods. As such, a specific methodology to study the protein binding and serum partitioning was developed in order to facilitate drug optimization of APC analogs

and related compounds. We characterize the serum protein binding for diagnostic and therapeutic APC analogs using a multifaceted approach of in silico docking analysis, and corroborative partitioning and pharmacokinetic studies in order to gain insight into better next generation drug design. In addition, we describe the development of a novel in silico methodology that is specific to characterizing human serum albumin binding to lipophilic compounds. This methodology may be useful in designing lipophilic drugs that have better pharmacokinetics and safety profiles, and offer insights into pharmacological strategies that alter the pharmacokinetics of lipoprotein-bound drugs.

Alkylphosphocholine analogs are a novel class of compounds that exhibit long plasma half-lives due to slow clearance rates from tight binding to serum proteins. These APC analogs have strong clinical potential because they exhibit broad-spectrum tumor-targeting and possess multimodal diagnostic imaging and therapy potential[1,2,5,10,12,28]. Currently, a suite of APC analogs are in preclinical and clinical development for diagnostic positron emission tomography (PET) imaging, near-infrared (NIR) intraoperative detection, and targeted radiotherapy for multiple cancer types, and more analogs are under development for other diagnostic imaging modalities[4,13,14]. The serum protein binding characteristics are not well understood for this class of agents and warrant further investigation. A better understanding of how these structures affect protein binding may yield important insights into smarter drug design of diagnostic imaging and therapy agents that have pharmacokinetic tailored profiles. These analogs may be used to develop predictive models and establish important behaviors for similar lipophilic compounds.

The binding of APC analogs and structurally related Alkylphospholipids (APL) analogs to serum proteins have been reported in scientific literature[29-31]. However, the

purported binding sites and partitioning characteristics have not been well characterized. APC analogs bear a striking resemblance to endogenous fatty acids. The binding of fatty acids to plasma proteins have been well characterized, and they predominantly bind to several distinct sites on albumin[32-36]. Moreover, crystal structure analyses of monounsaturated fatty acids, polyunsaturated fatty acids, and fatty acid-like molecules such as lysophosphatidylcholine display binding to these same pockets despite structural dissimilarities between these classes of compounds[29,37]. These binding sites are well conserved between mammalian species, although it has been reported that fatty acids bind to these pockets with less affinity on murine serum albumin[38]. These data suggest that the binding of these fatty acid-like molecules are in well-conserved binding pockets, and minor alterations of these compounds do not affect gross binding characteristics. Moreover, evidence suggests as fatty acid chain length increases, more partitioning is observed into the lipoprotein layer[39,40]. Taken together, these data supports the hypothesis that there may be an indirect correlation between albumin binding to these high affinity pockets and lipoprotein binding for these structurally similar classes of compounds.

We hypothesized that these APC analogs exhibit similar binding properties to fatty acids, and further explored their partitioning characteristics. We used a combination of in silico docking methods, experimental binding assays, partitioning assays, and pharmacokinetic (PK) studies to interrogate the structure-binding relationship and attempt to predict residence times of these agents based on albumin binding affinities. The methodology developed herein may facilitate drug optimization of not only this class of compounds, but also lipophilic compounds which display similar characteristics.

2B Materials and Methods

APC analogs

NM404 (18-(p-Iodophenyl)octadecylphosphocholine), 1501 (18-[p-(4,4-difluoro-4-bora-3a,4a-diaza-s-indacene-8-yl)-phenyl]-octadecyl phosphocholine), 1502 (1,3,3-trimethyl-2-[(E)-2-[(3E)-3-(2-[(2E)-1,3,3-trimethyl-2,3-dihydro-1H-indol-2-ylidene] ethylidene}-2-[4-(18-([2-(trimethylazaniumyl)ethyl hosphonato]oxy)octadecyl)phenyl] cyclohex-1-en-1-yl]ethenyl]-3H-indol-1-ium), were provided by Cellectar Biosciences, Inc. (Madison, WI). Their synthesis was previously reported[1]. Roughly 0.05mg/mL of the APC analogs were used for plasma partitioning studies. The analog ^{124}I-NM404 was radiolabeled via an isotope exchange reaction previously reported[41].

Ultracentrifugation

Fresh murine plasma was obtained from athymic nude mice , and fresh human unfrozen plasma was purchased from Zenbio (Cat #: SER-PLE10ML), and incubated with APC analogs compounds obtained from Cellectar Biosciences Inc, in separate glass tubes and incubated and shaken for 4h at 37°C. Samples were transferred to ultracentrifuge columns (Beckman Cat#: 344090) and tubes were spun at 250g for 8 hrs in Beckman Coulter L-60 Ultracentrifuge[42-44]. Samples were then carefully removed and the three phases were separated and imaged using Xenogen IVIS Imaging System 100 for fluorescence or the 2480 Automatic Gamma Counter from PerkinElmer for radioactivity or the to determine signal intensity in each layer.

Native Gel Electrophoresis

Fresh human unfrozen plasma was purchased from Zenbio (Cat #: SER-PLE10ML), and incubated with different APC compounds in separate Eppendorf tubes and incubated and shaken for 4hrs at 37°C. Samples were mixed with sample buffer (BioRad Cat#: 161-0738) and were run in non-denaturing conditions and in Tris-Glycine gels (Biorad Cat#: 456-1024, 161-1158). All gels were run under the same voltage and for the same duration. The position of the signal and the band intensities were determined using the Xenogen IVIS Spectrum imaging system under the well plate setting for fluorescence signals, and also BioScan AR2000 for radioactivity signals. Bands were then Coommassie stained (Protea SB-G250X). SeeBlue Plus2 Prestained standard from life technologies (Cat#: LC5925), mouse albumin from Sigma-Aldrich (Cat#: A3139), low-density human lipoprotein from Sigma-Aldrich (Cat#: L7914), high-density human lipoprotein from Sigma-Aldrich (Cat#: L8039), human gamma-globulins from Sigma-Aldrich (Cat#: G4286), human alpha1-acid glycoprotein from Sigma-Aldrich (Cat#:G9885), fatty acid free human serum albumin from Sigma-Aldrich (Cat#: A3782) were used as standards.

Albumin Spectrofluorescence Assay

Excitation scans and emission scans of fatty acid free human plasma albumin (Cat# A3782) in phosphate buffered saline were obtained at 37°C using the Tecan Safire II 44. Myristic acid (Cat # M3128) at different molar concentrations were allowed to bind to human plasma albumin and monitored via kinetic analysis mode at the emission

wavelengths determined from previous experiment on the Tecan Safire II. After 10 minutes, APC was injected and monitored via kinetic analysis mode on the Tecan Safire II.

Equilibrium Dialysis

Rapid equilibrium dialysis device (Cat # 90006) and well inserts (Cat # 89810) were purchased from ThermoScientific[45]. Fatty acid free human serum albumin from Sigma-Aldrich (Cat#: A3782) was dissolved in Phosphate buffered saline (PBS) and placed in the equilibrium dialysis chamber, and PBS was added to the collection well. The device was allowed to incubate on a shaker at 37°C during which small aliquots were taken from the collection well. Samples were analyzed via NanoDrop 200c for ultraviolet (UV) detection or 2480 Automatic Gamma Counter for radioactivity to determine concentration.

In Silico Docking Studies

Crystal structures of human serum albumin containing stearic acid were obtained from the Research Collaboratory for Structural Bioinformatics (RCSB) Protein Databank[33]. The ligands were removed from the albumin crystal structure using gedit version 2.30.2, while new APC ligands were created using Marvin v15.9.14.0 (2015) from ChemAxon and converted to the appropriate format using OpenBabel v2.3.1. The APC ligands were docked to albumin globally and also specifically to the sites previously occupied with fatty acids or similar lipophilic molecules using Autodock Vina v1.1.2[46,47]. Figures and videos were made with PyMol v1.7.6. Nonspecific binding energies were

quantitated by docking the APC ligands to human plasma albumin with ligands occupying the fatty acid binding sites. This particular methodology was employed because these compounds partition to lipoproteins, which signifies that non-specific surface binding molecules have more access to lipoproteins in plasma, but not buried proteins in the binding sites. Due to the similarities of docking conformations, the average binding affinities and SEMs were calculated after normalizing to non-specific binding energies.

Pharmacokinetic modeling

Concentration versus time data for NM404, 1501, and 1502 were analyzed by non-compartmental analysis to determine clearance, mean residence times, area under the curve, and area under the first moment curve. Calculations were normalized to the starting doses of compounds.

Log D determination

124I-NM404, 1501, and 1502 were added to octanol (Sigma-Aldrich 472328) and allowed to equilibrate overnight. Equal volumes of distilled water constituted at pH 7.4 were added and the mixture was rotated at room temperature shielded from light for 48hrs. The octanol and water phases were separated and analyzed using the gamma counter for 124I-NM404 or Tecan Safire II for optically active 1501 and 1502 to determine relative concentrations.

Pharmacokinetic Studies

All studies were performed in athymic, nude mice, with body weights ranging from 20-26g. Eighteen nude athymic mice were used for studies assessing the pharmacokinetic impact of different functional moieties. APC analogs for injection were prepared and formulated as previously reported[1]. Injected dose was normalized to the mass of radiolabeled compound and bodyweight of the animal in order to maintain consistency of injected mass dose between animals in comparative studies. Optical analogs, 1501 and 1502, were intravenously injected into mice at quantities of 2.6μmoL/kg, which is within the range of dosage used for past animal studies[12].

All mice were housed in a temperature-controlled room with a 12hr light/dark cycle, and were fed a standard rodent chow containing 6.2% fat, mostly polyunsaturated (Tekland Global 18% Protein Rodent Diet, Envigo). Free access to food and water was permitted prior to experiments. Prior to studies, blood was collected from each mouse to normalize for background fluorescence signal and radioactivity signal. The mice were injected with different APC compounds via tail-vein injection. Small amounts of blood were collected via maxillary puncture into EDTA vials. Concentrations of compound were determined using Tecan Safire II spectrophotometer or using the 2480 Automatic Gamma Counter from PerkinElmer.

Statistical Analyses

Statistical analyses were performed with Microsoft Excel version 15.0.4779.1002 or GraphPad Prism 5.0. Ten simulations for each fatty acid pocket were performed for

each APC analog, and repeated measures ANOVA, and paired t-Tests were calculated to determine differences in docking between APC analogs. All p-values <0.05 were considered significant.

Numbers of experiments and mice used are indicated. A total of 18 nude athymic mice were used for pharmacokinetic studies assessing the impact of the functional moiety.

2C Results

APC analogs share a similar targeting moiety, but differ in their functional moiety

The structures of the APC analogs are shown in figure 2.1. The targeting group consists of an alkyl chain and a phosphocholine polar head. NM404 derivatives including ^{124}I-NM404, ^{131}I-NM404, 1501, and 1502 share a targeting alkylphosphochline moiety consisting of 18 carbon alkyl chain (Figure 1). Altering the functional moieties affords different diagnostic and therapeutic qualities.

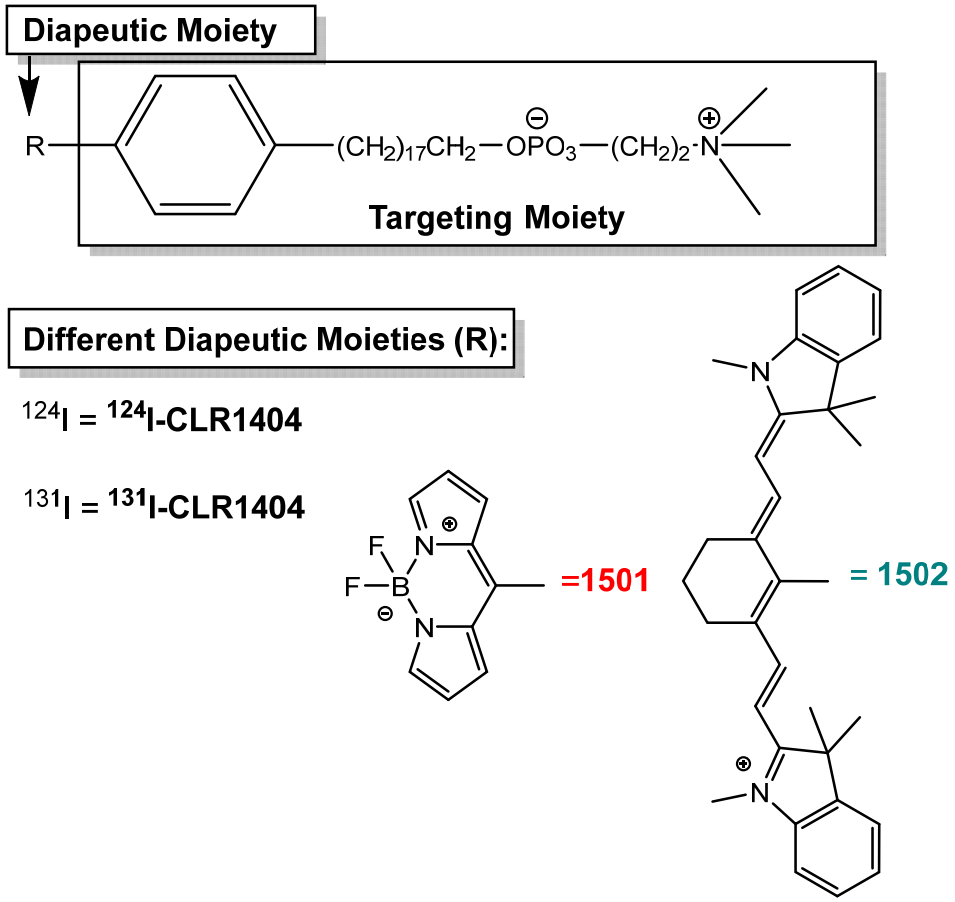

Figure 2.1. Structures of different analogs of alkylphosphocholine analogs. (A) Structures of 1501, 1502, and NM404.

APC analogs bind primarily to the serum albumin and lipoproteins

Partitioning studies using human plasma indicate binding of APC analogs primarily to two distinct layers after ultracentrifugation. Fresh, unfrozen human plasma was incubated with different APC analogs (100nM) at 37°C for 4 hours with stirring. The samples were then either ultracentrifuged or separated via native gel electrophoresis to look at partitioning of these compounds to different components of plasma (Figure 2.2A)[42]. These analogs primarily bound to the protein layer and the low density lipoprotein

layer, but very little remained in the free layer (Figure 2.2A). Native gel electrophoresis indicates binding of the APC analogs to high density lipoprotein (HDL) and low density liproprotein (LDL), and the main protein component albumin (Figure 2.2B). No appreciable binding was seen to alpha-acid glycoprotein, gamma globulins, or erythrocytes (data not shown). Furthermore, equilibrium dialysis revealed high affinity (96%) binding of ^{124}I-NM404 to fatty acid-free human serum albumin (HSA). These data suggest that this class of compounds binds predominantly to human serum albumin, but may incorporate into lipoproteins as well.

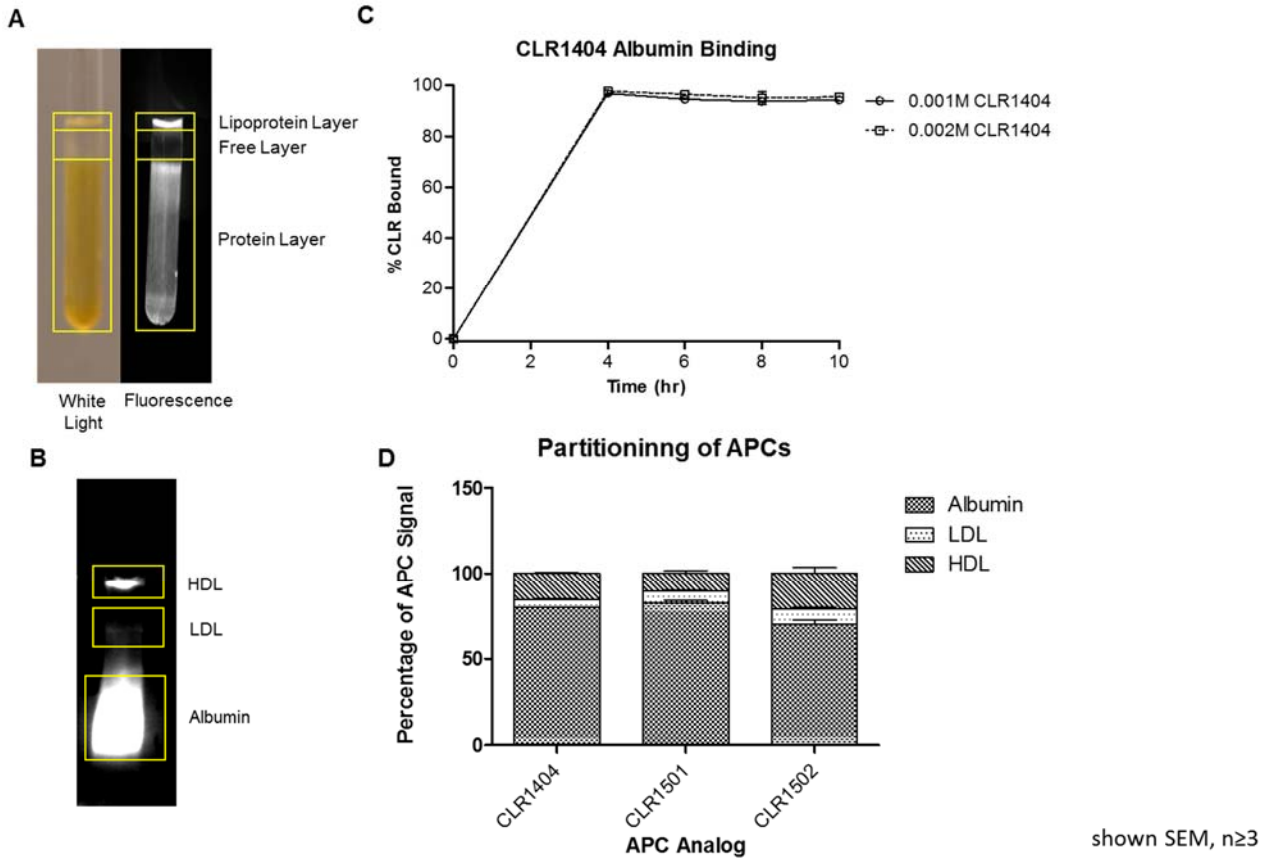

Figure 2.2. Partitioning of alkylphosphocholine analogs to plasma proteins. (A) Ultracentrifugation of 1502 reveals binding predominantly to lipoproteins and proteins in human plasma. (B) Native gel electrophoresis reveals 1502 binding predominantly to albumin in human plasma. (C) Equilirium dialysis reveals that NM404 is highly bound (96%) to human serum albumin. (D) Partitioning of APC analogs to lipoproteins using native gel analysis.

Native gel analysis was then performed on all three APC analogs (Figure 2.2D). Quantification of fluorescence (1501 and 1502) and radioactivity (NM404) revealed significant differences in partitioning between 1502 and the other two analogs. Significantly more LDL and HDL binding was observed with 1502 as compared to the other two analogs (Table 2.1). Furthermore, albumin binding was significantly lower with 1502 (69.88%) compared to NM404 (79.99%, p=0.01) and 1501 (82.64%, p=0.03).

APC Analog	HDL	LDL	Albumin
NM404	15.42 ± 0.41	4.60 ± 0.28	79.99 ± 0.22
1501	10.25 ± 1.25	7.11 ± 0.41	82.64 ± 1.62
1502	20.90 ± 2.57	9.21 ± 0.86	69.88 ± 3.32

Table 2.1. Native gel electrophoresis of APC analogs in human plasma. Quantitation of fluorescence (1501 and 1502) and radioactivity (NM404) signals in bands corresponding to HDL, LDL and albumin on native gel.

In order to assess the effect of the increasing lipoprotein concentration on partitioning, we incubated fresh unfrozen plasma with APC analogs and different concentrations of intralipid. Intralipid is a FDA approved essential fat formulation composed of 20% Soybean Oil, 1.2% egg yolk phospholipids, 2.25% Glycerin, and Water. The main fat constituents are linoleic acid (44-62%), oleic acid (19-30%), palmitic acid (7-14%), α-linolenic acid (4-11%) and stearic acid (1.4-5.5%)[48]. Due to its safety and its chylomicron-like constitution, it was used in this experiment to determine the effect of chylomicron or lipoprotein rich plasma on partitioning of APC analogs. Preliminary experiments with 1501 and 1502 and intralipid demonstrated increased partitioning of the APC analogs to the lipoprotein fraction when these compounds were incubated in fresh unfrozen human plasma in the presence of increasing intralipid concentrations of 0%, 10%, and 20% vol/vol (v/v). For 1501, the lipoprotein percentage of fluorescence intensity

(measured in the units of radiance efficiency) increased from 7.33% with no intralipid to 14.40% with 20% v/v intralipid (Supplemental Figure 2). Concomitantly, the albumin-binding percentage decreased from 85.93% with no intralipid to 79.32% with 20% intralipid added.

A

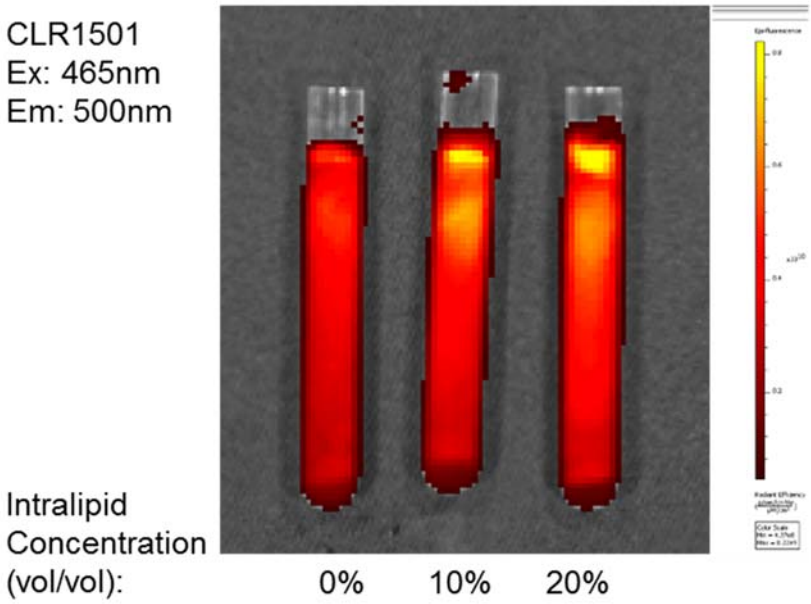

B

Intralipid (v/v%)	0	10	20
Lipoprotein	7.33	11.82	14.40
Free	6.74	8.24	6.28
Protein	85.93	79.94	79.32

Figure 2.3. Lipoprotein partitioning increases with increasing lipoprotein concentration in human plasma incubated at 37°C. (A) 1501 fluorescence intensity in the lipoprotein layer increases with increasing lipoprotein concentration. (B) Quantitation of fluorescence signal in the three layers as intralipid concentration increases.

In silico docking analysis reveals APC analogs bind to same seven fatty acid binding sites corroborated by albumin spectrofluorescence assays

Crystal structures of long chain fatty acids show binding primarily to seven distinct sites on human plasma albumin (Figure 2.3A)[33]. Moreover, binding of monounsaturated and polyunsaturated fats are well conserved to these seven binding sites (Figure 2.3A and Supplemental Videos V1). APCs and fatty acids (FAs) share striking structural similarities, which include a polar head group, and hydrophobic alkyl chain (Figure 2.3B).

NM404 was docked globally onto human plasma albumin with fatty acids removed to determine the most favorable binding pockets. Global docking analysis revealed binding of NM404 to the seven distinct binding pockets of human plasma albumin (Figure 2.4B). Furthermore, the most favorable docking orientations in these different pockets were conserved between APCs and crystal structure binding of FAs to these pockets (Figure 2.5). The carboxylic oxygen group of fatty acids coordinate to the basic residues on the surface of the protein, much in the same way that the phosphate group on NM404 coordinate with the same basic residues on albumin.

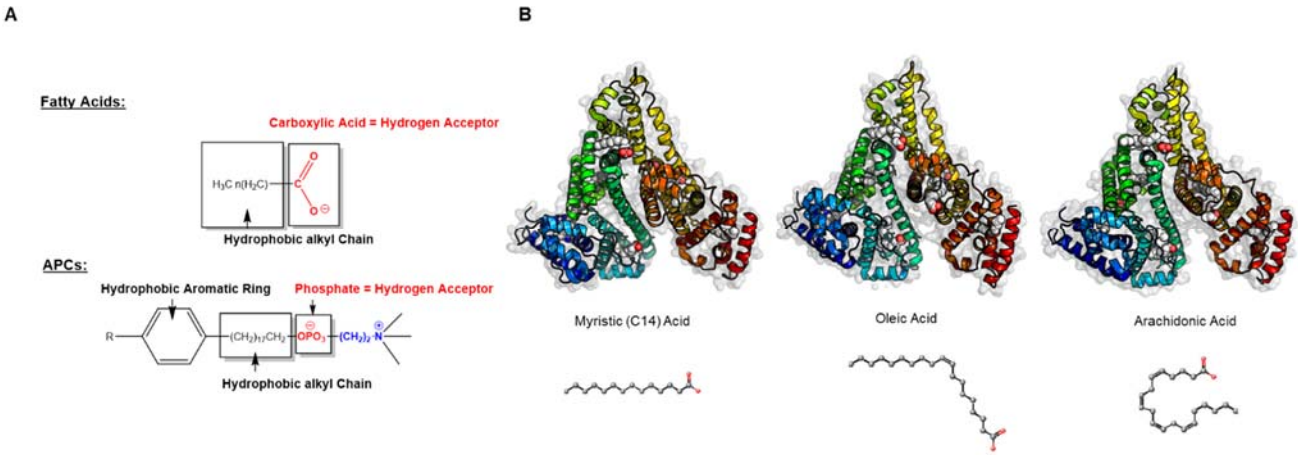

Figure 2.4. Structural analysis of fatty acids and alkylphosphocholine analogs reveal similarities. (A) APCs and fatty acids bear striking similarities in chemical structure. (B) Crystal structure analaysis reveals well-conserved binding sites for fatty acids to human seru albumin despite variations in chemical structures between different classes of fatty acids. Long-chain fatty aids, monounsaturated fatty acids, and polyunsaturated fatty acids bind to 7 specific sites on human serum albumin.

To corroborate these findings, albumin spectrofluroscence assays were performed to determine shared binding sites. Briefly, tyrosine and tryptophan residues on human plasma albumin can be excited and emit a natural fluorescence, which is quenched by close ligand contact[29]. The tryptophan and tyrosine residues exhibited peak excitation at 280nm, and the tyrosine residues exhibited another peak excitation at 295nm (Supplemental figure S2). Emission was measured at 339nm. Some of these residues are found within the fatty acid binding pockets of the protein. In the presence of myristic acid (C14 fatty acid), a significant decrease in quenching was observed upon addition of different molar equivalents of NM404 (Supplemental figure S2). These differences were significant even at 10 molar equivalents of NM404, suggesting that these high-affinity FA pockets may have been occupied. Moreover, the kinetics of binding are very fast, as the quenching was observed immediately after injection and remained stable for 2hr (data not shown). Taken together, these studies suggest that the same pockets and binding orientations are shared between fatty acids and APC analogs.

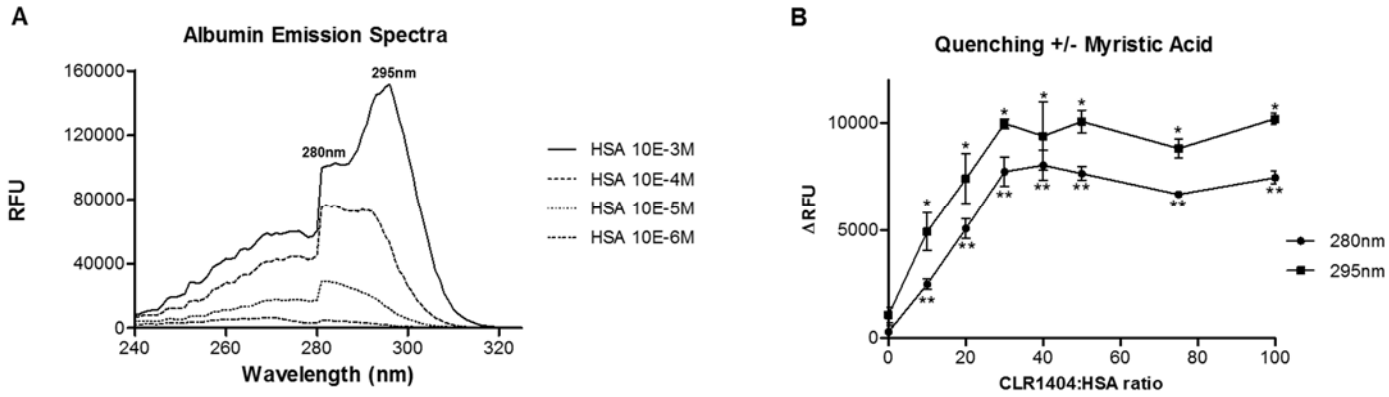

Figure 2.5. Albumin spectrofluorescence reveals abrogation of NM404-induced quenching in the presence of myristic acid. (A) Excitation spectra of tyrosine and tryptophan residues on human serum albumin. (B) Myristic acid irreversibly quenches albumin fluorescence, decreasing CLR-1404 – induced quenching.

Different Functional Moieties Impact Albumin Binding and Inform Biological Half-Lives of APC analogs

Using in silico docking, we analyzed the binding of stearic acid (C18 fatty acid), 1501, 1502, and NM404 to the seven distinct fatty acid pockets on HSA (Figure 2.4). Our results show similar docking energies between 1501 and NM404, but not 1502 (Figure 2.5A). The bulkiness of the near-infrared fluorescence probe of 1502 reverses many of the docking orientations, namely FA sites 2, 4, and 5 (Figure 2.4E, 2.4F, Supplemental video V3), such that the zwitterionic phosphocholine of 1502 is buried into the hydrophobic pocket of these binding sites, creating unfavorable electrostatic interactions. 1502 exhibited significantly lower docking energies for all except fatty acid site 7 compared to NM404 (Figure 2.6A). Many of these energies were close to 0 kCal/moL suggesting that binding to these sites were energetically comparable to nonspecific binding. The average docking energies and standard errors for all 7 binding sites of stearic acid, NM404, 1501, and 1502 are -1.75±0.164, -1.97±0.23, -1.80± 0.40, and -0.82± 0.32 kCal/moL respectively (Figure 2.6B). Repeated measures ANOVA revealed a difference between the binding energies between stearic acid, NM404, 1501, and 1502 ($p=0.0063$). The average docking energy for 1502 to the binding sites were significantly lower compared to stearic acid ($p=0.0082$), NM404 ($p=0.0018$), and 1501 ($p=0.0047$) using a pairwise t-Test.

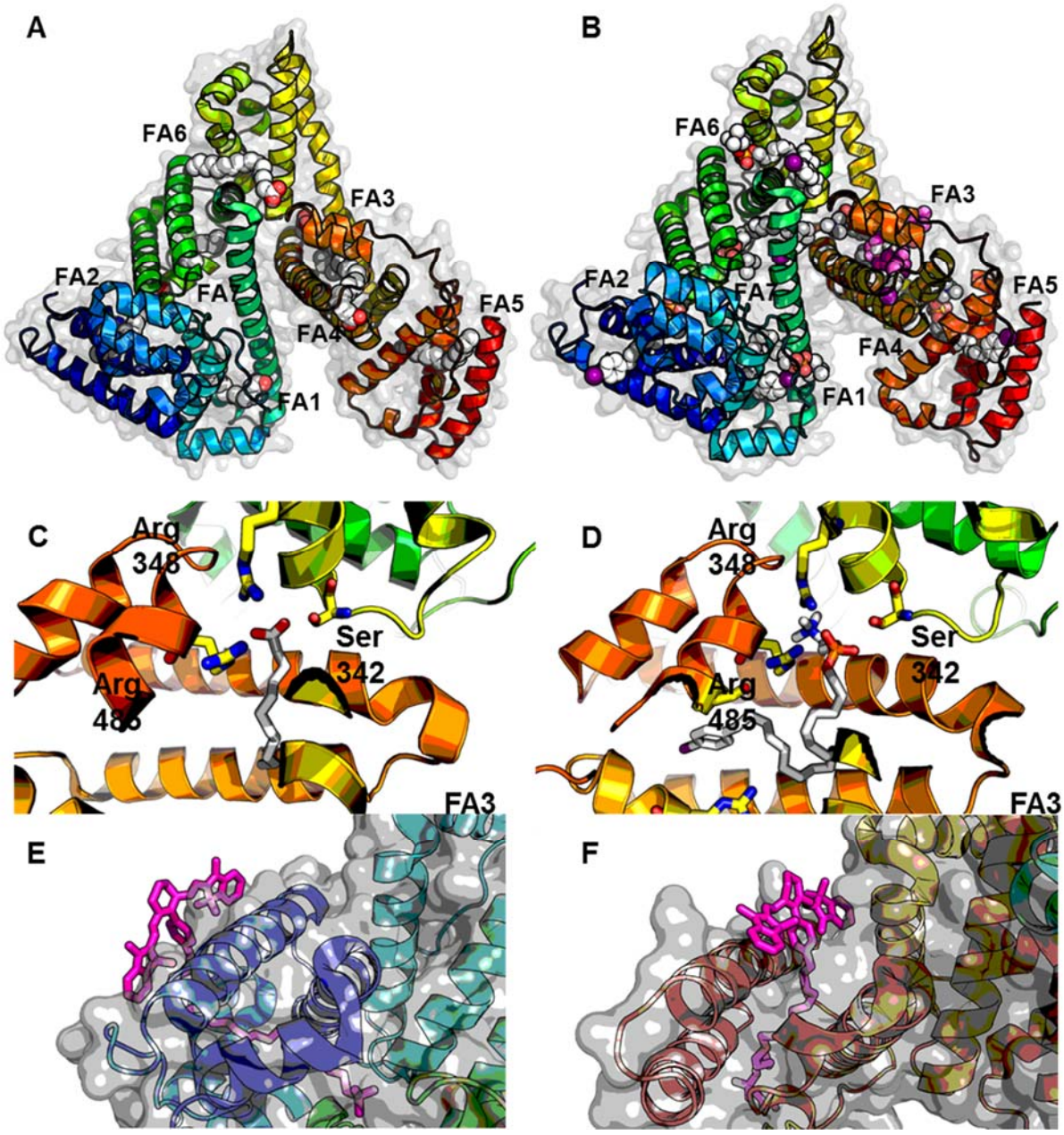

Figure 2.6. *In silico* docking shows shared binding sites and similar orientation of binding between fatty acids and APC analogs (A) Crystal structure shows 7 high affinity sites of fatty acid binding to human serum albumin. (B) *In silico* docking of NM404 shares same 7 high-affinity docking sites as fatty acids. (C-D) Stearic acid shares similar docking orientation as NM404 in numerous fatty acid pockets, including fatty acid site 3. (E-F) 1502 docks in reverse orientation due to steric bulk of functional moiety such that zwitterionic phosphocholine is buried in the hydrophobic pocket, creating very energetically unfavorable interactions.

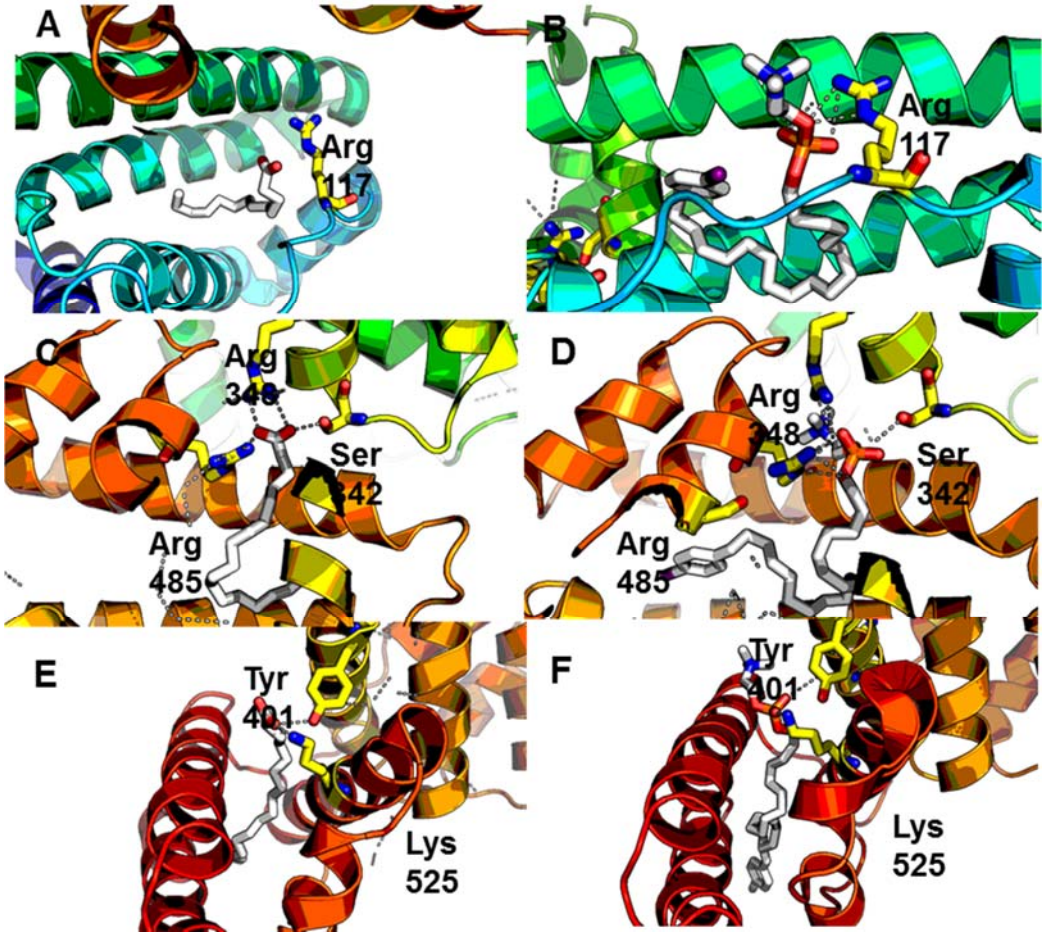

Figure 2.7. Crystal structure comparison of stearic acid in (A) FA1, (C) FA3, and (E) FA5, and lowest affinity *in silico* docking states of NM404 (B, D, F). The same basic residues coordinate the high-affinity binding of the two compounds. Sites 6 and 7 do not have an orientation of binding.

To assess if these docking energies may have relevant impact on clearance, we assessed the mean residence times of these compounds in nude, athymic mice by collecting small amounts of blood (10μL) through maxillary punctures and plotting blood concentration over time (n=6). Non-compartmental modeling was employed and calculations were normalized to the starting dose. 1502 demonstrated significantly shorter mean residence time (MRT) of 33.95 hr compared to 99.25 hr for NM404, and 236.07 hr for 1501 (Table 2.2). Clearance values were highest for 1502 (0.08 L/hr) compared to NM404 (0.02 L/hr) and 1501 (0.01 L/hr) as well (Table 2). Area under the

curve (AUC) and area under the first moment curve were also calculated for these APC analogs (Table 2.2).

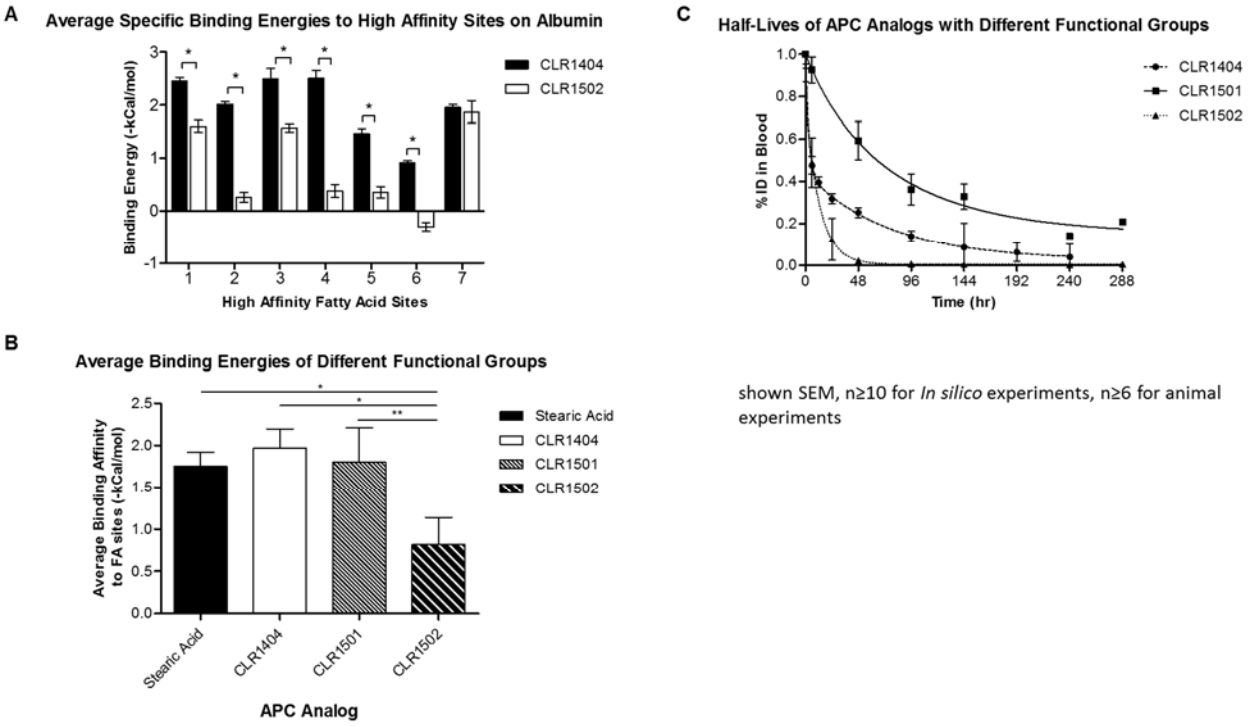

Figure 2.8. *In silico* docking energies correlate with *in vivo* distribution half-lives of APC analogs of different functional moieties. (A) Binding energies of stearic acid and different APC analogs of all 7 binding sites. (B) Average energies of all 7 sites of stearic acid and APC analogs. (C) Biological half-lives were determined via blood draws in naïve nude athymic mice.

Interestingly, the average logD values and standard error of the three compounds were measured and determined to be 2.07±0.006, 4.59±0.11, and 4.66±0.54 for NM404, 1501, and 1502, respectively. As 1502 is the most lipophilic based on these measurements, lipophilicity alone may not be the best predictor of albumin binding (Table 2.2).

Compound	AUC (hr)	AUMC (hr^2)	MRT (hr)	CL (L/hr)	log D	Docking Energy (-kcal/moL)
NM404	43.66	4333.63	99.25	0.02	2.07	1.97
1501	159.64	37686.99	236.07	0.01	4.59	1.80

1502	13.16	446.66	33.95	0.08	4.66	0.82

Table 2.2. Non-compartmental modeling reveals faster clearance and shorter mean residence times for 1502. Non-compartmental analyses were performed on mouse plasma data of the APC analogs.

2D Discussion

The expensive and time-consuming process of synthesis and testing of different compounds can be minimized if predictive modeling can be employed and successfully validated in an effort to effectively screen compounds with the most favorable properties. In cancer drug development, only 5% of preclinical effective drugs make it through FDA approval, and the overwhelming majority fail primarily due to poor pharmacokinetic properties[21-23]. To this end, we have developed and corroborated an in silico modeling methodology that predicts pharmacokinetic behavior based on the structure of APC analogs and hydrophobic binding pockets on human serum albumin. Our methodology not only allows us to design future analogs with more tailored pharmacokinetics, but also provides pertinent and comparative insights into behaviors of similar lipophilic compounds. This may be a powerful approach to screen for lead compounds with optimal pharmacokinetics may minimize chances of failure further down the drug development pipeline.

APC analogs are versatile delivery agents that can be purposed for multi-modality imaging and therapy. Many of these agents are undergoing evaluation in clinical trials or nearing clinical trials testing. The long plasma half-lives of these synthetic APC analogs and similar compounds may have diagnostic imaging and therapeutic implications. Long delays between administration and imaging that achieves sufficient contrast may

decrease the utility of imaging agents, and long distribution kinetics may result in off-target toxicities for therapeutic agents. Therefore, an understanding of the relationship between drug structure and pharmacokinetic properties of these agents can be leveraged to determine feasible strategies for optimizing drug design for faster tumor uptake and clearance from the body.

Due to the structural similarities between fatty acids and APC analogs, an interrogation of plasma protein binding and partitioning may reveal important pharmacokinetic parameters which may be useful for future drug design or strategies to alter the pharmacokinetics. FAs bear striking resemblance to APCs structurally, as both share a polar head group and long hydrophobic tail. In silico binding studies and partitioning studies reveal similar binding characteristics between these two distinct classes of compounds. Namely, the same binding pockets for FAs on albumin are also favorable sites of binding for APC analogs. Also, as chain length increases for FAs, there appears to be less binding to these binding sites and more partitioning to the lipoprotein fraction[39,40]. Our results suggest that the same is seen with increasing size of APC analogs. Addition of bulkier diapeutic moieties impair the ability 1502's ability to bind albumin, increasing its partitioning onto lipoproteins. Moreover, hypoalbuminaemia decreases the binding of lysophosphatidylcholine, a FA-like molecule, to albumin and increases binding to lipoproteins[49]. These data suggest that the lipoprotein-bound fraction is affected by both the concentrations of albumin and concentrations of the compound. Our experiments further suggest that lipoprotein binding can also be affected by specific albumin-binding affinity and the concentration of the lipoprotein fraction.

Namely, lower binding affinities and higher lipoprotein concentrations increase partitioning to the lipoprotein fraction.

In addition, the binding affinity to these pockets on albumin correlates with the biological mean residence times of these agents. These data suggest that in silico binding affinities may have a correlation to biological half-lives of these agents and can be used for drug design purposes to predict residence times of new compounds. Because our in silico methodology specifically interrogates the hydrophobic pockets on albumin, and normalizes binding to the surface of albumin, our methodology is suited to study partitioning. The rationale behind our model is that these APC analogs have a very small unbound fraction, and that lipoproteins scavenge the free APC analogs and the weakly bound drugs at the surface of albumin. Our pharmacokinetics studies suggest that in silico modeling may be a more sensitive predictor of albumin binding and residence times compared to physicochemical measurements such as logD, which are fairly non-specific[25]. Although these in silico affinities correlate with experimental binding parameters, further work is necessary to characterize the binding affinities directly amongst the different APC analogs.

Our studies have demonstrated that APC analogs also bind to the lipoproteins, which has significant implications on their pharmacokinetics. As the bulkiness of the diapeutic moieties of these APC analogs increases in size, partitioning to the lipoprotein fraction(s) also increase, in agreement with studies performed with fatty acids of increasing alkyl chain lengths[38-40]. Because lipoprotein binding is thought to be unsaturable, it is unlikely that a significant fraction of these APC analogs can exist as free compound in the blood[25,49-52]. This was demonstrated with the exogenous administration

of intralipid, which increased the lipoprotein fraction at the expense of the protein-bound fraction, but did not significantly alter the free fraction. Lipoprotein-bound APC analogs may have faster clearance than the albumin-bound APC analogs, and may thus have an impact on the half-lives of these agents. This may be because lipoproteins have a much faster clearance than albumin, which circulate for about 19 days before being catabolized by the liver[53]. Lipoprotein-binding drugs such as cyclosporine demonstrate increased bioavailability and faster clearance with high fat diets suggesting that the lipid profile may modulate clearance of lipoprotein-bound drugs[50,54]. These results suggest that increased binding to lipoproteins may increase the rate of clearance of these compounds, and that free drug concentrations and hepatic extraction may not have a significant impact on the pharmacokinetics of these APC analogs. Therefore, clinically relevant parameters such as lipid profile and dietary fat intake may impact the pharmacokinetics of these agents. Future studies monitoring diet and metabolism of these compounds will provide interesting observations as to how these parameters may impact the pharmacokinetics of APC analogs.

To the best of our knowledge, these studies illustrate for the first time the purported binding sites of alkylphosphocholines onto human serum albumin. Moreover, we have established structure-binding and structure-partitioning trends that may be of use to future drug design of alkylphosphocholines and other classes of small molecules that display structural similarities. This methodology can be immediately applied to FDA approved APL analogs, and other lipophilic compounds.

Future work will encompass the effect of lipid profile on the tumor uptake and clearance of these agents, strategies to enhance tumor to background contrast, strategies

to manipulate the pharmacokinetics of these agents, and experiments to assess the binding affinities to the different binding pockets for APC analogs.

Chapter 3: Fluorescent and Fluorescent/PET APC Analogs for Intraoperative Surgical Illumination of Tumor Margins

3A Introduction

Surgical resection of cancer remains the cornerstone of oncological therapy. Positive resection outcomes have been correlated with local recurrence and significantly decreased long-term survival in many types of cancers [55,56]. In both low-grade gliomas and high grade glioblastomas, patients with gross total resection outcomes (GTR) have improved long term survival outcomes compared to patients with subtotal resection outcomes (13 months v. 8 months for high grade gliomas, and 15 years v. 9.9 years for low grade gliomas)[57-59]. Furthermore, the presence of residual tumor (defined as "positive margin") has been reported as high as to 65% of high grade gliomas, highlighting the need for better intraoperative distinction between malignant and non-malignant tissue[60]. While positive margins are associated with increased rates of local recurrence and worse clinical outcomes compared with GTR, overzealous resection can eliminate or compromise adjacent vital tissue, resulting in poor functional outcomes.

Traditionally, surgeons have relied upon subjective assessments during resection and ablative procedures (for example, of subtle tactile and visual tissue differences) to distinguish cancer tissues from the adjacent tissues intraoperatively[55,56]. Improvements in cancer imaging technology are now aiding surgeons in visualizing cancer in the operating room. Several intraoperative modalities including ultrasound, fluoroscopy, CT, and MRI have all been harnessed to improve resection outcomes and facilitate surgeries. These intraoperative imaging modalities can be used to provide additional information about anatomical localization as well as depth of cancer and vital structures, and tissue

shift during operation. However, these intraoperative imaging modalities lack targeted agents for cancer detection, are limited in their sensitivities of contrast detection, and offer distinctly different and non-superimposable field of view (FOV) from that of the surgical cavity.

Over the past few years, developments in fluorophores, cancer targeting strategies, and devices for fluorescence detection have poised fluorescence-guided surgery (FGS) as a new intraoperative imaging modality that may revolutionize the field of oncological surgery. Fluorescence imaging exhibits several favorable characteristics that are conducive for clinical implementation, which include real-time detection capabilities with a superimposable field of view, an abundance of cancer targeted fluorophores, high sensitivity of detection, an excellent safety record with clinically-used probes[61-64], a lack of ionizing-radiation exposure, lower costs and much less cumbersome detection instrumentation compared with other intraoperative imaging modalities[65-67]. Importantly, the ability to couple fluorophores to a variety of available targeting molecules enables the application of this modality to numerous clinical indications, especially in the field of oncology in which targetable biomarkers are currently being characterized and validated in many cancer types. In addition to improving primary outcomes such as long term survival, FGS may also improve the safety of surgeries by highlighting vital structures, and decrease surgery times and patient exposure to anesthesia.

One of the first successful demonstrations of clinical applications of FGS was a randomized phase III clinical trial in Europe that completed in 2006, comparing fluorescence-guided surgery with the fluorescent precursor 5-aminolevulinic acid (5-ALA) followed by radiotherapy, and standard microsurgery followed by radiotherapy[60]. In cells

with high metabolic activity such as cancer cells, 5-ALA is processed via the haeme-synthesis pathway to produce fluorescent protoporphyrin IX, which exhibits a fluorescence absorption peak of 405 nm, and an emission peak in the red visible light range (635 nm). This study demonstrated that use of the intraoperative fluorescent agent in surgery improves safe maximal resection (66% v. 32%) and progression-free survival by 6 months without a decline in performance status in glioblastoma patients [60]. FGS with 5-ALA is approved in Europe and adopted internationally in countries like Japan and Australia, and is currently in phase III evaluation in the United States in GBMs at multiple academic centers under the name of the BALANCE trials.

Fluorescence-guided imaging involves the administration of a cancer-selective fluorophore and imaging with a fluorescence excitation and detection device at an optimal time-point to achieve contrast. Due to recent improvements in photophysical characteristics, fluorophores with excitation and emission spectra in the near-infrared (NIR) wavelength range (700–900 nm) have attracted the most attention owing to their improved depth-penetration range (millimeters) compared with fluorophores that are excited and emit fluorescence at shorter wavelengths. NIR fluorophores are especially suited for *in vivo* applications because background fluorescence and scattering from water and chromophores are minimized in the NIR wavelength range[28] (Figure 3.1). Within the past 3 years, NIR cancer-targeted fluorophores have initiated clinical trials testing[28] (Table 3.1).

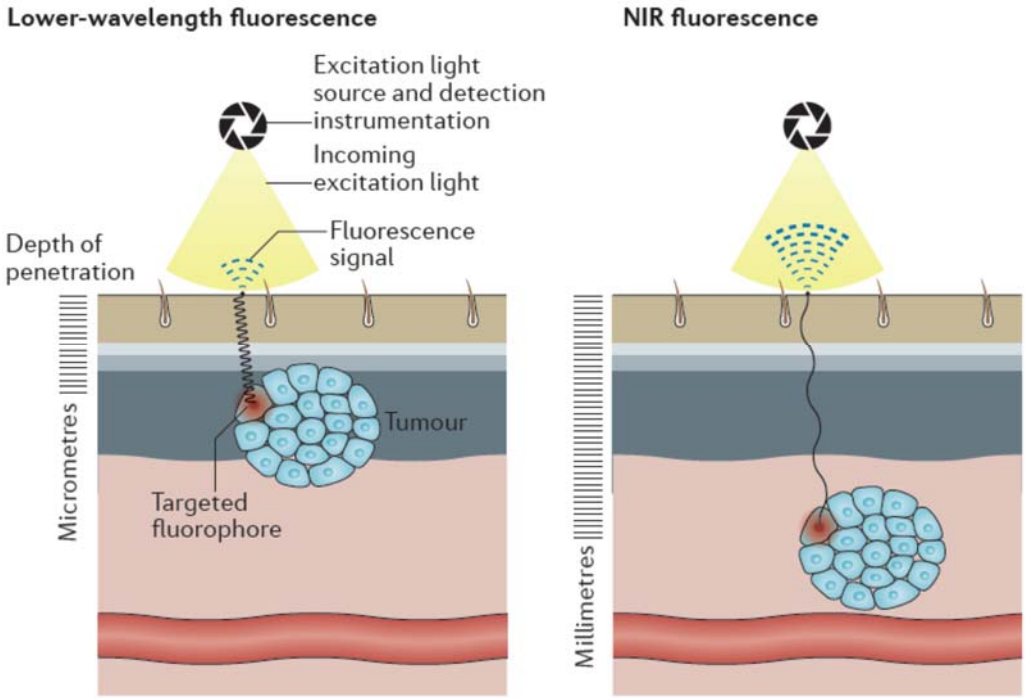

Figure 3.1. NIR fluorescence is more suitable for *in vivo* imaging applications than visible-light fluorescence. Near-infrared (NIR) fluorophores (700-900nm) have deeper tissue penetration and lower background fluorescence than visible-light fluorescence, resulting in enhanced signal-to-noise-ratios. The detection depths achievable with the currently available instrumentation ranges from millimeters with NIR fluorescence to micrometers with visible-range fluorescence.

CONTRAST AGENT	LIGAND	DYE	TARGET	CANCER TYPE	STATUS	CLINICAL TRIALS IDENTIFIER
Antibody						
Bevacizumab-800CW	Bevacizumab	IR-800CW	VEGF	Breast Cancer	Phase 1	NCT01508572
				Breast Cancer	Phase 2	NCT02583568
				Adenomatous Polyposis Coli	Phase 1	NCT01691391
				Rectal Cancer	Phase 1	NCT01972373
				Esophageal Cancer, esophageal dysplasia	Phase 1	NCT02129933
Cetuximab-800CW	Cetuximab	IR-800CW	EGFR	Head and Neck Cancer	Phase 1	NCT01987375
Panitumumab-800CW	Panitumumab	IR-800CW	EGFR	Head and Neck Cancer	Phase 1	NCT01998373
ProstaFluor	huJ-591	IR-800CW	PSMA	Prostate Cancer	Phase 0	NCT01173146
MDX1201-A488	MDX1201	Alexafluor488	PSMA	Prostate Cancer	Phase 0	NCT02048150
Small peptide						
BLZ-100	Chlorotoxin peptide	ICG	Annexin 2	Sarcoma, Soft Tissue	Phase 1	NCT02464332
				Pediatric Central Nervous System Tumors	Phase 1	NCT02462629
				Solid Tumors	Phase 1	NCT02496065
				Adult Glioma	Phase 1	NCT02234297
GE-137	c-Met ligand	Cy5	c-Met 122	Colon polyps and cancer	Phase-1	2010-019197-33
Activatables						
LUM015	GGRK peptide	Cy-5	Cathepsin	Sarcoma, Soft Tissue, Breast Cancer	Phase 1	NCT01626066
AVB-620	Activatable Cell Penetrating Peptides	Cy5, Cy7	Proteases	Breast Cancer	Phase 1	NCT02391194
Small Molecule						
E17	Folate	Fluorescein isothiocyanate	Folate Receptor	Breast Cancer	Phase 1	NCT01994369
				Lung Cancer	Phase 1	NCT01778920
				Primary Hyperparathyroidism	Phase 1	NCT01996072
				Renal Cell Carcinoma	Phase 0	NCT01778933
				Ovarian Cancer	Phase 1	NCT02000778
OTL38	Folate	Cy7	Folate Receptor	Ovarian Cancer	Phase 2	NCT02317705
				Renal Cell Carcinoma	Phase 1	NCT02845609
				Pituitary Adenomas	Phase 1	NCT02629549
				Neoplasms	Phase 1	NCT02602119
Multi-modality						
Indium-111-DOTA-Girentuximab-IRDye800CW	Girentuximab	IR-800CW	Carbonic Anhydrase IX	Renal Cell Carcinoma	Phase 1	NCT02497599

Table 3.1. Fluorescence-guided surgery in clinical trials. CNS, central nervous system; EGFR, epidermal growth factor receptor; FR, folate receptor; ICG, indocyanine green; IND, investigational new drug study; MET hepatocyte growth factor receptor; PSMA, prostate-specific membrane antigen; VEGF, vascular endothelial growth factor.

Weichert *et al* has recently extended small molecule platform agents for cancer imaging to include fluorescent analogs for intraoperative surgical illumination of cancer margins. In 2014, Weichert *et al* reported a new class of small molecules for PET imaging and targeted radiotherapy that demonstrates broad spectrum tumor targeting potential in

over 60 preclinical cancer models and in early human clinical studies[2]. Through numerous structure activity relationship studies, 1404 was selected from among 30 similar phospholipid ether and alkylphosphocholine compounds as the best tumor-imaging agent. Due to the broad-tumor targeting potential of 1404, two fluorescent analogs 1501 and 1502 with the same targeting backbone as 1404, but different fluorophores, were synthesized for subcellular localization studies and FGS respectively. 1501 with a BODIPY tag was used in subcellular localization studies and 1502 with a NIR fluorophore IR-775 was validated in several preclinical rodent models of cancer for FGS.

Subcellular localization studies with 1501 offered insight into the mechanism of APC's cancer specificity. In co-culture, cancer cells uptake of 1501 was 6-10 fold greater compared to normal fibroblasts. Like other APC analogs, disruption of the lipid rafts with methyl-beta-cyclodextran prior to treatment with 1501 resulted in abrogation 1501 fluorescence by over 60%[2]. These key studies suggest that lipid-rafts play a significant role in the selective uptake in cancer cells, and work by other groups suggest that lipid rafts are overexpressed on cancer cells.

Swanson *et al* compared the fluorescent analogs 1501, 1502 and 5-ALA in mice with stereotactically implanted GBMs[12]. Both 1501 and 1502 demonstrated high tumor to normal brain contrast ratios of 7.23 and 9.28 respectively, with 1502's tumor to normal brain contrast being significantly higher than 5-ALA at 4.81 (Figure 3.2). In the mice with orthotopic GBM xenografts injected with 1501, flow cytometry analysis of normal brain cells and tumor cells demonstrated that 1501 fluorescence was 14.8 times higher in tumor cells than normal brain cells. Histological analysis of the tumor margins illustrated that fluorescence from 1501 was observed in the tumor, but not beyond the tumor margins.

These studies illustrate the cancer selectivity of 1501 and 1502 in GBMs, and the potential of 1502 as an intraoperative fluorescent agent. Other studies with 1502 have also illustrated 1502's ability to illuminate tumors in preclinical colon cancer, breast cancer, and prostate cancer models [13,14,68]. Because of 1502's excitation and emission are in the NIR range, higher tissue penetrance and improved tumor to normal contrast can be achieved using this newer generation NIR-labeled APC compared to 1501 and 5-ALA. Importantly, 1502 represents a broad-spectrum cancer selective NIRF agent that has tremendous potential to improve surgical resection outcomes in multiple cancers. The small molecule platform offers important advantages to other larger carriers which include small molecule simplicity and cost, and improved extravasation into cancer cells compared with agents such as antibodies.

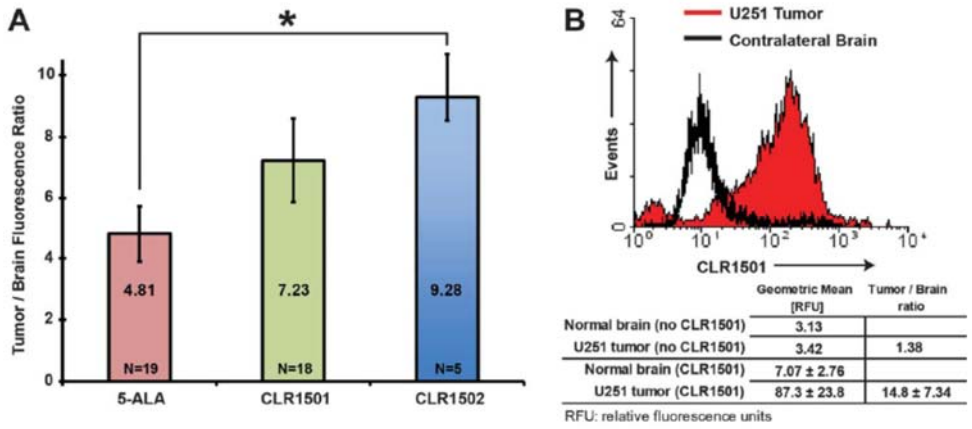

Figure 3.2. (A) 1501, CLR502, and 5-ALA tumor-to brain fluorescence ratios for U251-derived orthotopic xenograft. (B) Flow cytometetry of 1501-positive cells from U251-dervied orthotopic xenograft compared with normal brain. RFU, relative fluorescence units.

However, there are many limitations of NIRF as a new imaging modality. Limited depth penetration ultimately restrict NIRF imaging to superficial cancers, while limitations in robust quantitation limit the diagnostic sensitivity and specificity of detecting

malignancies as no standard reference values are in place for surgeons to accurately distinguish tumor from non-tumor [55,69]. These issues may significantly impede the translation of NIRF imaging as a modality into the clinic, and preclude its use for the bulk of all cancers, which are non-superficial. A deeper understanding of the limitations of NIRF are thus warranted in order for this modality to progress for future clinical translation.

As imaging modalities all have unique strengths and limitations, combining multiple imaging modalities is a possible strategy to overcome the limitations of single modalities by synergizing the benefits of both modalities. Combining fluorophores with radioactive tracers will enable quantitative detection, unlimited depth of detection, and high spatial resolution for in vivo applications. Additionally, this would permit careful characterization of the NIRF modality using PET as a quantitative gold standard. The knowledge acquired with this unique dual-labeled agent would be of substantial use, as very little research with regards to the quantitation of NIRF and its limitations affecting its quantitation has been performed with this new modality still in its infancy.

Also of clinical importance, the dual-modality agent with both NIRF and PET imaging capabilities would permit detection of non-superficial cancers and metastases, greatly enhancing prospective clinical indications. This agent would also allow primary localization of these lesions for staging and diagnoses, and context-permitting, surgical excision of these sites without additional anatomical imaging aside from PET/CT. Furthermore, identical pharmacokinetics, biodistribution and toxicity profiles greatly simplifies the administration and use of tandemly labeled agent. Because of these benefits, the dual-modality approach proves a synergistic means to not only study and better understand the limitations of NIRF, but also in the process, create an agent that

successfully overcomes NIRF's limitations, positioning the modality for future clinical application. The aim of this work was to create a PET/NIRF APC analog.

3B Materials and Methods

Chemical Synthesis

All chemicals were purchased from Sigma Aldrich Chemical Co. (Milwaukee, WI). Thin-layer chromatography was performed using DC-Alufolien Kieselgel 60 F254 plates (E. Merck, Darmstadt, Germany). Visualization was achieved by UV light at 254nm. Melting points were collected using a MEL-TEMP II Capillary Melting Point apparatus. Proton and C13 NMR data were collected on a Varian Unity-Inova 500 MHz NMR Spectrometer. Chemical shifts are reported in parts per million (ppm) relative to tetramethylsilane (TMS), and spin multiplicities are given as s (singlet, d (doublet), t (triplet), q (quartet), m (multiplet), or br m (broad multiplet). High-resolution mass spectra were obtained on a Bruker MaXis Ultra-High Resolution Quadrupole Time-of-Flight MS at the Analytical Instrumentation Center of UW School of Pharmacy.

RZ-7, RZ-9 (3) 2,4-diiodobenzoic acid

2-amino-4-iodobenzoic acid (970mg/3.8mmol) was added to 20mL H_2O:HCl (v/v). Mixture was stirred in a methanol ice bath at 0°C. Sodium nitrite (656mg/9.5mmol) was slowly titrated into the mixture. Reaction proceeded for 30 min at 0°C, and then potassium iodide (3.90g/23mmoL) was added to the reaction mixture. The reaction was allowed to proceed at room temperature overnight. The reaction was washed with water until the pH became neutral, and then purified via silica column chromatography. Yield: 270mg (67.8%). MP: 183.0°C. ^{1}H-NMR (500 MHz, $CDCl_3$): 8.39, 7.73, 7.61 (d, 1H each, $I_2C_6H_3$).

High resolution mass spectrometry (HRMS): calculated for $C_7H_4I_2O_2$-H (M^+ + H) 372.8217, found 372.8218.

RZ-10 (4) (2,4-diiodophenyl)methanol

Borane (8.5mL) was added to a solution of (2,4-diiodophenyl)methanol (1.52g, 4.25mmol) in THF (3mL), and allowed to react overnight at 4°C. The reaction was quenched with sodium bicarbonate, and extracted with ethyl acetate, and dried over sodium sulfate. Evaporation of solvent resulted in a yellow solid. MP: 95.3°C. Yield: 1.44g (94.1%). ^{1}H-NMR (500MHz, $CDCl_3$): 8.14, 7.69, 7.19 (d, 1H each, $I_2C_6H_3$). ^{13}C-NMR (125MHz, $CDCl_3$) 146.72, 142.64, 137.80, 129.95, 98.20, 93.66, 77.58, 77.32, 77.07, 69.05.

RZ-11 (5) 1-(bromomethyl)-2,4-diiodobenzene

PS-Ph_3 was added to (2,4-diiodophenyl)methanol (1.44g, 4.00mmol), and the mixture was dissolved in 12mL of THF. Tetrabromomethane (1.72g/5.2mmol) was slowly added to the reaction, and the reaction was stirred at room temperature overnight. Mixture was resuspended in hexane and separated via silica column. Product was eluted with 1:99 dichloromethane:hexane, which formed a white powder upon evaporation of solvent. Yield: 1.31g (77.5%). ^{1}H-NMR (500MHz, $CDCl_3$) 8.20, 7.65, 7.18 (d, 1H each, $I_2C_6H_3$). ^{13}C-NMR (125MHz, $CDCl_3$) 147.51, 139.41, 137.99, 131.56, 100.84, 94.70, 94.68, 77.27, 77.01, 76.76, 37.743. HRMS: calculated for $[C_7H_5I_2]^+$ (M^+) 342.8475, found 342.8472

RZ-4 Synthesis (6) 2-carboxy-5iodobenzene-1-diazonium

Mesylate (3.2g/10.17mmol) was dissolved in 65mL butanone, and heated to 90°C. Sodium Iodide was added to the reaction. Reaction proceeded for 2.25 hours. The organic layer was extracted with ethyl acetate, and the extract was washed with H_2O. Sodium thiosulfate was used to remove the excess iodine, and the extract was then dried with sodium sulfate. Yield: 4.066g (94.2%). ^{1}H-NMR (500MHz, $CDCl_3$) 4.12 (q, 2H, $CO_2CH_2CH_3$), 3.19 (t, 2H, ICH_2) , 2.28 (t, 2H, CH_2CO_2Et), 1.82 (m, 2H, ICH_2CH_2), 1.61 (m, 2H, $I(CH_2)_{14}CH_2$), 1.25 (m, 27H, $(CH_2)_{12}$, OCH_2CH_3).

RZ-12 (7) ethyl 18-(2,4-diiodophenyl)octadecanoate

Reaction was performed under vacuum due to sensitivity of cross-coupling step to moisture. 19-iodonoadecan-3-one (0.85g/2.01mmol) was dissolved in DMA (0.4mL). Zinc (196mg/3.02mmol) in suspension in DMA (3.0mL) was added via cannula to $I(CH_2)_{16}CO_2Et$, and mixture was immersed in oil bath at 54°C. The reaction mixture was allowed to stir overnight and checked via TLC for completion. A mixture of RZ-11 (1.28g/3.02 mmol), $NiCl_2$-glycine (44mg/0.20mmol) and i-Pr-PyBox (79mg/0.26mmol) was added to the mixture under nitrogen via cannula. The reaction mixture was stirred for the first 10 minutes and then allowed to proceed at room temperature for 48hrs. A yellow precipitate formed and was extracted with ethyl acetate. After crystallization with acetonitrile, yellow crystals formed. Yield: 1.29g (54.5%). MP: 48.0°C. ^{1}H-NMR (500MHz, $CDCl_3$) 8.12, 7.55, 6.92 (d, 1H each, $I_2C_6H_3$), 4.12 (q, 2H $CO_2CH_2CH_3$), 2.63 (t, 2H, $ArCH_2$), 2.28 (t, 2H CH_2CO_2Et), 1.61 (m, 2H, $ArCH_2CH_2$), 1.54 (m, 2H, $CH_2CH_2CO_2$),

1.25 (m, 29H, $(CH_2)_{13}$, $CO_2CH_2CH_3$). ^{13}CNMR (125MHz, $CDCl_3$) 173.92, 146.64, 145.15, 137.18, 130.72, 101.47, 90.99, 77.27, 77.01, 76.76, 60.14, 40.36, 34.41, 30.07, 29.68, 29.67, 29.66, 29.64, 29.61, 29.56, 29.47, 29.42, 29.28, 29.25, 29.16, 25.00, 14.27. HRMS: calculated for $C_{26}H_{42}I_2O_2$ $^+$H (M^+ + H) 641.1347, found 641.1345. Calculated for $C_{26}H_{42}I_2O_2$ +Na (M^+ + Na) 663.1166, found 663.1167.

RZ-13 (8) 18-(2,4-diiodophenyl)octadecanoic acid

Potassium hydroxide (293.4mg/4.14mmol) was added to ethyl 18-(2,4iiodophenyl)octadecanoate (663.0mg/1.04mmol) and dissolved in THF (9mL) and water (1mL). The mixture was immersed in an oil bath at 50°C and reaction was allowed to proceed overnight. The reaction was quenched with HCl and extracted with ethyl acetate. The extract was washed with water until the pH became neutral, and then dried with sodium sulfate. Yield: 628mg (99.1%). MP: 84.1°C. ^{1}H-NMR (500MHz, $CDCl_3$) 8.12, 7.55, 6.92 (d, 1H each, $I_2C_6H_3$), 2.63 (t, 2H, $ArCH_2$), 2.35 (t, 2H CH_2CO_2H), 1.63 (m, 2H, $ArCH_2CH_2$), 1.54 (m, 2H, $CH_2CH_2CO_2H$), 1.25 (m, 26H, $(CH_2)_{13}$) ^{13}C-NMR (125MHz, $CDCl_3$) 179.45, 146.64, 145.16, 137.19, 130.72, 101.47, 90.99, 40.36, 33.93, 30.08, 29.68, 29.67, 29.65, 29.64, 29.60, 29.56, 29.45, 29.42, 29.25, 29.07. HRMS: calculated for $C_{24}H_{38}I_2O_2$ + Na (M^+ + H) 635.0853, found 635.0847.

RZ-14 (7) 18-(2,4-diiodophenyl)octadecan-1-ol

18-(2,4-diiodophenyl)octadecanoic acid (606mg/0.99mmol) was dissolved in 3mL THF, and BH_3 (3mL) was added to the reaction. The reaction proceeded at 4°C overnight.

The reaction was quenched with sodium bicarbonate, extracted with ethyl acetate, and then dried with sodium sulfate. The mixture was resuspended in acetonitrile and crystrallized. Yield: 592.0mg (100.0%). ^{1}HNMR (500MHz, $CDCl_3$) 8.12, 7.55, 6.92 (d, 1H each, $I_2C_6H_3$), 3.62 (t, 2H, CH_2OH), 2.63 (t, 2H, $ArCH_2$), 1.57 (m, 2H, $ArCH_2CH_2$), 1.25 (m, 28H, $(CH_2)_{14}$), ^{13}C-NMR (125MHz, $CDCl_3$) 146.63, 145.16, 137.18, 130.72, 101.47, 90.99, 63.12, 40.36, 32.82, 30.07, 29.69, 29.68, 29.67, 29.63, 29.62, 29.61, 29.55, 29.44, 29.41, 29.25, 25.75. HRMS: calculated for $C_{24}H_{40}I_2O$ +Na (M^+ + Na) 621.1061, found 621.1051.

RZ-15 (11) 18-(2,4-diiodophenyl)octadecyl 2-(trimethylazaniumyl)ethyl phosphate

Triethylamine was distilled to remove moisture. In a reaction flask, 18-(2,4-diiodophenyl)octadecan-1-ol (567mg/0.948mmol) was dissolved in 4 mL toluene. Distilled triethylamine (200uL/1.33mmol), was added to the reaction flask, along with Cl-oxo-dioxaph (100uL/1.04mmol). A white precipitate formed immediately upon addition of Cl-oxo-dioxaph. Reaction proceeded 1hr at room temperature with stirring. Reaction mixture was filtered and solvent evaporated. The compound was redissolved in chloroform, and transferred via cannula into a pressure tube. The tube was flushed with nitrogen to remove moisture. Dried lithium bromide (107mg/1.23mmol) was dissolved in 3mL acetonitrile and transferred to the pressure tube via cannula. The tube was submerged in an oil bath at 70°C, and the reaction was allowed to proceed overnight with stirring. The resulting brown mixture was filtered and precipitated with 50mL acetonitrile to obtain a light yellow powder. The compound was purified using silica column chromatography. Pure compound was obtained using a 65:25:4 $CHCl_3$:MeOH:H_2O

elution mixture. Yield: 479.5mg (66.3%). ^{1}H-NMR (500MHz, $CDCl_3$) 8.12, 7.58, 6.96 (d, 1H each, $I_2C_6H_3$), 4.23 (m, 2H, $PO_4CH_2CH_2NMe_3$), 3.87 (q, 2H, $CH_2N(CH_3)_3$), 3.60 (m, 2H, CH_2PO_4), 2.66 (t, 2H, $ArCH_2$), 2.20 (s, 9H, $N(CH_3)_3$), 1.64 (m, 2H, $ArCH_2CH_2$), 1.56 (m, 2H, $CH_2CH_2PO_4$), 1.28 (m, 28H, $(CH_2)_{14}$). HRMS: calculated for $C_{29}H_{52}I_2NO_4P$ + H (M^+ + H) 764.1800, found 764.1805. Calculated for $C_{29}H_{52}I_2NO_4P$ +Na (M^+ + Na) 786.161562, found 786.1623.

RZ-17 (12) 2-[(E)-2-[(3E)-2-[3-iodo-4-(18-{[2-trimethylazaniumyl)ethyl phosphonato]oxy}octadecyl)phenyl]-3-{2-[(2E)-1,3,3-trimethyl-2,3-dihydro-1H-indol-2-ylidene]ethylidene}cyclohex-1-en-1yl]ehenyl]-1,3,3-trimethyl-3H-indol-1-ium chloride hydroiodide

18-(2,4-diiodophenyl)octadecyl 2-(trimethylazaniumyl)ethyl phosphate (102mg/134mmol), IR-775 (204mg/392mmol), Bis(neopentyl glycolato)diboron (91mg/342mmol), and Pd-PEPPSI-Pr (2.7mg) were added to the reaction flask. All reagents were dried and flushed with nitrogen. Reagents were dissolved in gas-free methanol (2.5mL), and trimethylamine was added to mixture. The reaction proceeded at 35°C for 24hr. The product was purified using silica column chromatography. Pure compound was obtained using a 65:25:4 $CHCl_3$:MeOH:H_2O elution mixture. Yield: 22.0mg (15.1%). ^{1}H-NMR (500MHz, $CDCl_3$) 7.14-7.44 (m, 14H, Ar-H) 4.23 (m, 2H, $PO_4CH_2CH_2NMe_3$), 3.87 (q, 2H, $CH_2N(CH_3)_3$), 3.60 (m, 2H, CH_2PO_4), 3.23 (s, 9H, $N(CH_3)_3$), 2.80 (t, 2H, $ArCH_2$), 2.70 (t, 4H, C_6H_6), 2.08 (m, 2H, C_6H_6), 1.73 (m, 2H, $ArCH_2CH_2$), 1.63 (m, 2H, $CH_2CH_2PO_4$), 1.26 (m, 31H, $(CH_2)_{14}$), 1.22 (s, 12C, NC_7H_9). HRMS: calculated for $C_{29}H_{52}I_2NO_4P$+H (M^+ + H) 764.1800, found 764.1805. Calculated

for $C_{29}H_{52}I_2NO_4P$ +Na (M^+ + Na) 786.161562, found 786.1623. HRMS: calculated for $C_{61}H_{88}IN_3O_4P^+$ (M^+) 1084.5552, found 1084.5550.

Fluorescence Characterization

1501 (18-[p-(4,4-difluoro-4-bora-3a,4a-diaza-s-indacene-8-yl)-phenyl]-octadecyl phosphocholine) and 1502 (1,3,3-trimethyl-2-[(E)-2-[(3E)-3-(2-[(2E)-1,3,3-trimethyl-2,3-dihydro-1H-indol-2-ylidene]ethylidene)-2-[4-(18-([2-trimethylazaniumyl)ethyl phosphonato]oxy)octadecyl)phenyl]cyclohex-1-en-1-yl]ethenyl]-3H-indol-1-ium) were provided by Cellectar Biosciences, Inc (Madison, Wisconsin). Protoporphyrin IX (PpIX) was purchased (P8293, Sigma-Aldrich, St. Louis, Missouri). 1501,1502, and PpIX were diluted in ethanol at 4 mg/mL. Ethanol solvent was chosen to avoid the unwanted spectral shifts seen with dimethyl sulfoxide. Fresh unfrozen human plasma was also used to see the effects of plasma protein interaction with fluorescent APCs on their fluorescence properties. 1501, 1502, Iodo-1502, Di-Iodo-1502, and Iodo-Di-1502 were then analyzed in experimental triplicates with the Tecan Safire2 microplate reader to obtain fluorescence excitation and emission spectra. The following spectra collection parameters were used: 1-nm increments, 10-nm bandwidth, 10 counts per wavelength, and gain of 90. Fluorescence spectra were normalized to peak values.

Orthotopic and Flank Xenograft Models of GBM

All studies were performed under approved protocols by the University of Wisconsin-Madison Institutional Review Board and the Animal Care and Use Committee.

For flank models, female nude (nu/nu) athymic mice (n=3) were inoculated subcutaneously with U87 cells suspended in Matrigel into the right flanks (10^6 cells). For orthotopic models, nonobese diabetic severe combined immunodeficient (NOD SCID) mice, U251 glioblastoma line, and our patient-derived 22TGBMand Glioma stem cells (GSC) lines were used. GSC lines (22CSC, 33CSC,105CSC) were isolated and validated for multipotent differentiation and tumor initiation via orthotopic xenografts in our laboratory as previously reported[70]. In brief, cells passaged in vitro were enzymatically dissociated into single-cell suspensions, with between $2 \cdot 10^5$ and 10^6 cells suspended in 5 mL of phosphate-buffered solution (PBS).

Imaging of Brain sections

Paraformaldehyde perfusion-fixed brains were bisected at the tumor injection site. The IVIS Spectrum system (Perkin-Elmer/Xenogen, Waltham, Massachusetts) was used to visualize the brains with measurements of average radiance obtained from a standardsized region of interest in the tumor compared with contralateral normal brain to calculate a ratio of average radiance. The following excitation/ emission combinations were used: 1501, 500/540 nm; 1502, 745/800 nm; and 5-ALA, 430/640 nm. After IVIS imaging, the brains were embedded in paraffin, sectioned, stained with hematoxylin and eosin, and imaged with an EVOS XL Core bright-field microscope (Advanced Microscopy Group, Bothell, Washington) to verify tumor xenograft. It is important to note that because of technical constraints of the IVIS system, 5-ALA excitation was performed at 430 nm (range, 415-445 nm), not at the reported optimum of 402 nm.

PET/Fluorescence Imaging

Iodo-1502-injected mice were imaged 48 hours after injection with the Fluobeam 800 (Fluoptics, Grenoble, France), which is a hand-held imaging system designed for detecting *in vivo* near-infrared fluorescence (excitation laser wavelength of 780 nm and a charge-coupled device camera with filters to detect wavelengths > 800 nm), and the Siemen's MicroPET/CT system. Fluorescence imaging was conducted on mice before euthanasia and after euthanasia on the flank xenografts after surgical resection. White-light photographs were also obtained.

3C Results

Synthesis of Dual-Labeled Compound Iodo-1502

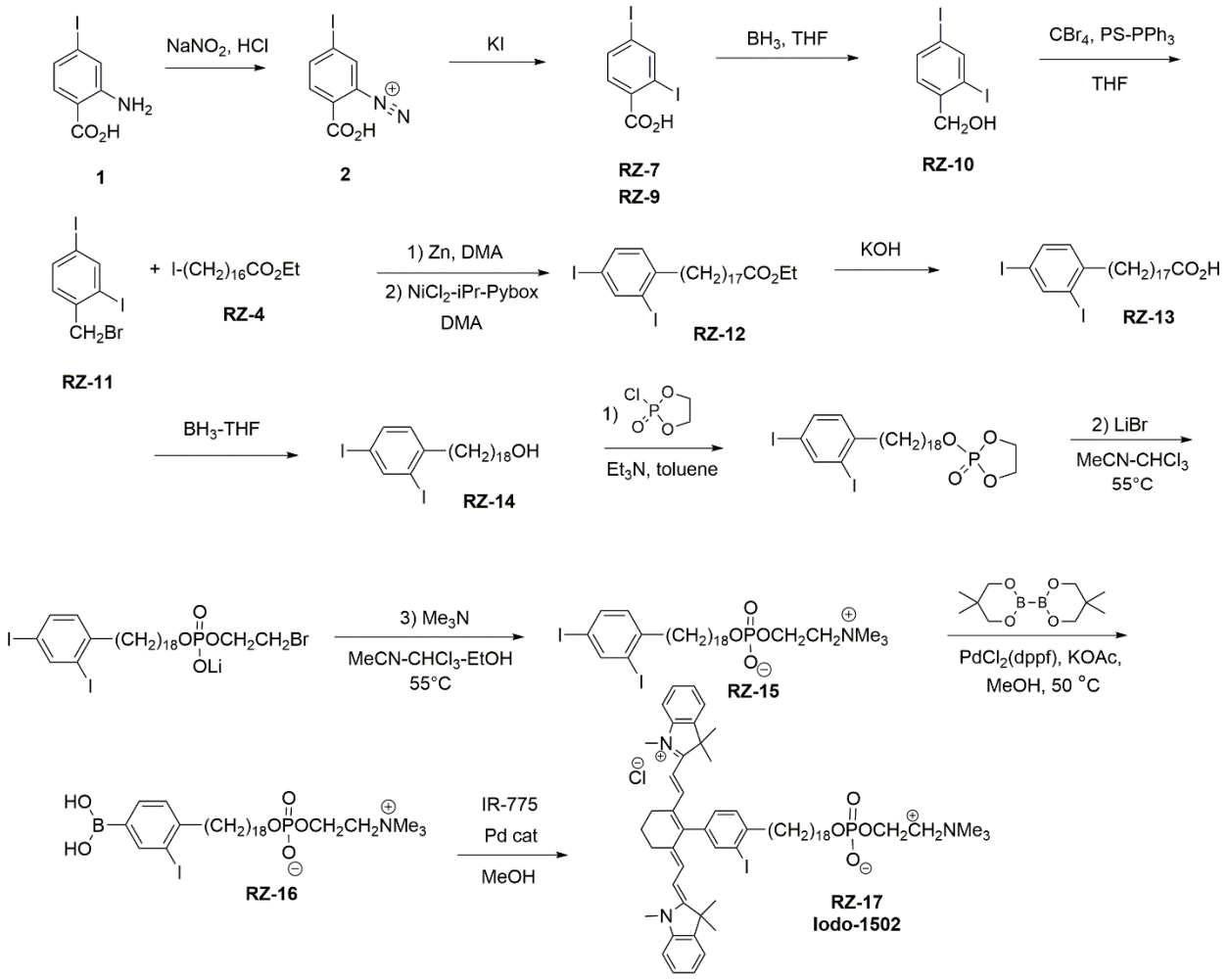

Figure 3.3. Synthetic scheme of Iodo-1502.

Iodines were introduced in the *para* and *orthogonal* positions of the aromatic ring starting from 2-amino-4-iodobenzoic acid. Briefly, the *ortho* amine was treated with sodium nitrite under acidic conditions to produce the diazonium ion, which was subsequently substituted with iodine using potassium iodine using a Sandmeyer reaction (Figure 3.3). The alkylphosphocholine backbone was subsequently conjugated in a series of steps analogous to those described previously[1]. The *para*-positioned iodine was selectively boronated through steric hindrance of the *ortho*-iodine. Isotope exchange of

the non-radioactive iodine with ^{124}I was performed as described previously[41] to yield to final product.

Substitution of iodine radiotracer with NIRF dye IR775 does not impact broad-spectrum cancer targeting properties.

^{124}I-NM404 , ^{131}I-NM404 , and the near-infrared fluorescent analog 1502 are a novel class of small molecule cancer-targeting agents called alkylphosphocholine analogs. These APC analogs share a targeting moiety composed of a phosphocholine head, hydrophobic tail, and an aromatic ring that delivers these agents to the sites of malignancy, and a functional moiety fashioned for diagnostic imaging or therapy (Figure 2.1). Having been extensively tested, and shown to display prolonged selectivity and retention in all but 3 of over 60 in vivo rodent cancer, human cancer, and cancer stem cell models, ^{124}I-NM404, the PET imaging agent is now being further evaluated in multiple human clinical imaging trials. We have demonstrated that tumor selectivity has been retained in preclinical prostate, colon, breast, GBM, and GBM stem cell rodent models with the near-infrared agent 1502 (Figure 3.4)[4,12,13,15,71]. These studies illustrate that substitution of iodine with optically active NIRF dye yields similar tumor selectivity and retention, suggesting bulk tolerance of functional payloads. In addition, the tissue distribution of 1502 and the iodinated APC analogs appears to be similar with the highest uptake in the tumors and liver. These results suggest retention of cancer targeting despite substantial structural alteration of the functional moiety. In designing the dual-labeled compound, the same basic structure of 1502 will be retained and an iodine will be added in the *ortho* position of the aromatic ring. This minimal structural perturbation should not

affect the cancer targeting, biodistribution characteristics, or pharmacokinetics of the dual-labeled agent significantly, and we hypothesize that this novel agent should behave very similarly to 1502 due to the observation that there is substantial structural tolerance of the functional moiety.

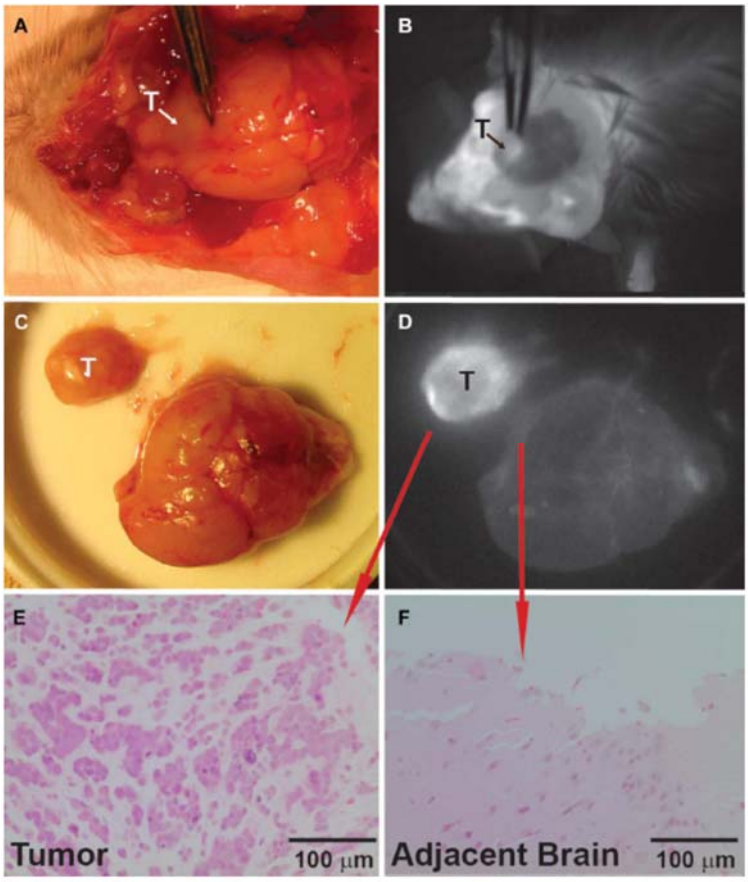

Figure 3.4. (A) White Light and (B) 1502 fluorescence of 22CSC-derived orthotopic xenograft (A-B) during craniotomy and (C-D) after resection. (E-F) Histological validation demonstrating excellent macroscopic tumor delineation from normal brain (hematoxylin and eosin). CSC, cancer stem cell.

Dual-modality Iodo-1502 demonstrates same photophysical properties as 1502

The introduction of the iodine in the *ortho* position of the aromatic ring may change the fluorescence properties of the new fluorescent agent from its parent analog 1502. In

order to assess the impact of the iodine on the fluorescence, fluorescence scanning was performed on 1502 and Iodo-1502 in human plasma at 1mM concentration. The fluorescence excitations and emissions of Iodo-1502 remained the same as that of its parent analog 1502 (Figure 3.5).

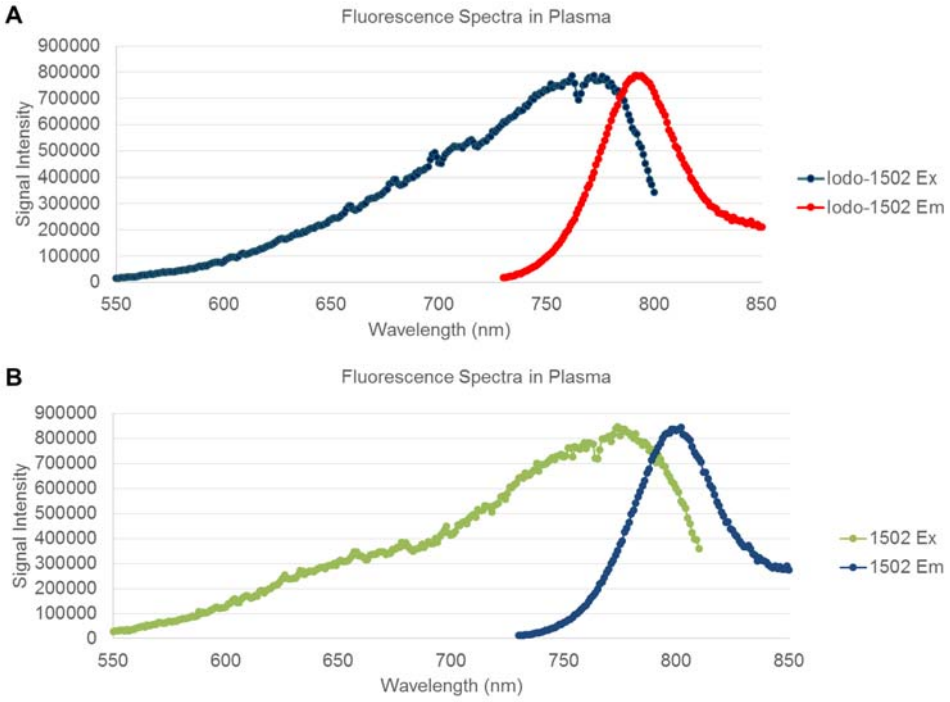

Figure 3.5. Fluorescence excitation and emission of (A) Iodo-1502 and (B) 1502 in human plasma at 25°C.

Dual-modality Iodo-1502 agent exhibits tumor targeting in flank xenografts and orthotopic GBM stem cell models of cancer

The iodo-1502 compound was synthesized, purified, and radiolabeled. Preliminary studies with the novel agent Iodo-1502 demonstrates tumor-targeting in a flank xenograft model of rodent cancer (Figure 3.6). These preliminary *in vivo*

experiments validate our hypothesis that addition of an *ortho* iodine onto the aromatic ring does not impact the in vivo behavior of these APC analogs to a significant degree. Our studies demonstrate the feasibility of studying NIRF agents with our DL APC analog Iodo-1502.

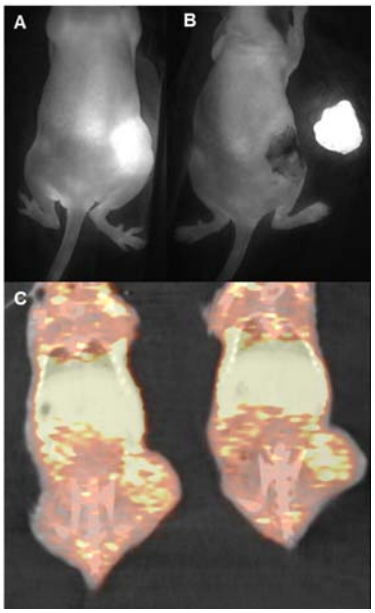

Figure 3.6. Fluorescence and PET/CT Imaging of Iodo-1502 in a flank U87 model. (A-B) Fluorescence images of a flank U87 xenograft (A) before, and (B) after resection (48hrs). (C) MicroPET/CT images of the same animals at 48hrs post-administration.

Synthesis of other Dual-Labeled Compounds

Although the *ortho*-positioned iodine imparts a unique selectivity for the boronation reaction and subsequent isotope exchange, the synthetic yield from RZ-16 to RZ-17 is fairly low (15.1%). The radiolabeling efficiency of the remaining *ortho*-positioned iodine is very low as well, resulting in very limited quantities of labeled PET/fluorescent compound that prohibit further quantitative studies of the fluorescence modality.

Due to this challenge, other dual-labeled fluorescent/PET APC analogs were synthesized and further characterized (Figure 3.7). The iodines were placed on the fluorophore to be more accessible for radiolabeling. Preliminary results show that iodine placement on the fluorophore shifts the excitation and emission into longer wavelengths and narrows the Stoke's shift in ethanol and human plasma at 1mM. Future work will include radiolabeling, purification, and *in vivo* validation of these new analogs.

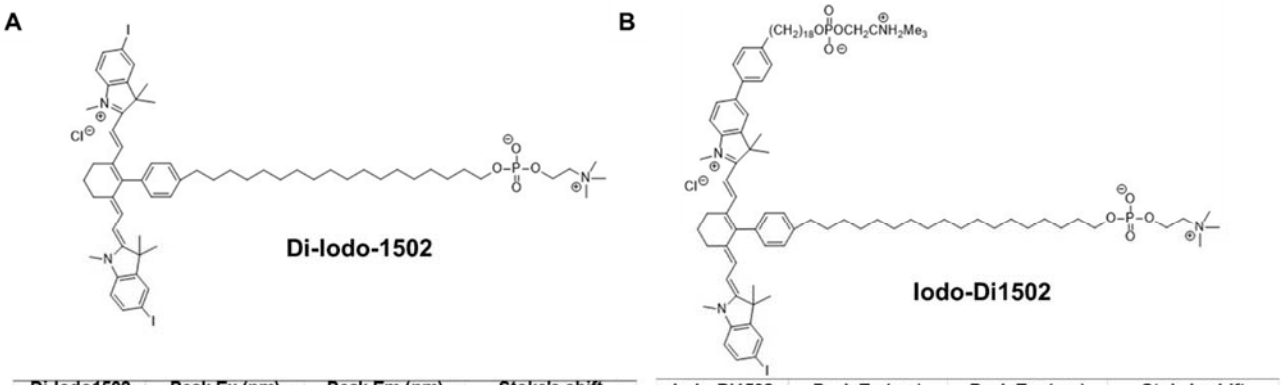

Di-Iodo1502	Peak Ex (nm)	Peak Em (nm)	Stoke's shift
EtOH	762	796	34
Plasma	779	801	22

Iodo-Di1502	Peak Ex (nm)	Peak Em (nm)	Stoke's shift
EtOH	773.5	809	35.5
Plasma	792.5	809	16.5

Figure 3.7. (A-B) Structures of Di-iodo-1502 and Iodo-Di1502. (C-D) Peak fluorescence excitation and emissions were determined in plasma.

3D Discussion

In summary, we have synthesized and validated a NIR targeted fluorophore that can be used to intraoperatively illuminate a broad array of different cancers. Substitution of the iodine with larger fluorophores still retains APC analogs' tumor selectivity and retention as illustrated by 1502's ability to target numerous cancer models[12,13,15,71]. In addition, 1502 exhibits significantly higher contrast (9.28 v. 4.81, $p<0.1$) than existing agents like 5-ALA. In order to quantitatively understand fluorescence as a modality, we combined fluorescence and the quantitative gold standard PET into one agent through

minimal perturbation of 1502's chemical structure. We have shown proof-of-concept tumor targeting with the first dual-modality PET/fluorescence APC analog in flank xenograft models of GBM.

This project aims to investigate the quantitative behavior of the new NIRF modality, and to understand its key limitations by combining the NIRF tracer with a quantitative PET tracer into a single targeted cancer agent. Subsequent experiments with the new dual-modality PET/fluorescent compounds will attempt to quantitatively model the NIRF modality, and understand key limitations of this new modality for *in vivo* applications of cancer detection and imaging such as quenching of fluorescence signal at higher concentrations. Significant progress in this field of imaging will be achieved if quantitative cutoffs of fluorescence imaging can be determined for NIRF agents experimentally, and if key limitations of *in vivo* use are understood. An important outcome from these findings will hopefully yield quantitative models that may be applied not only to this targeted NIRF agent, but also other NIRF agents as well, facilitating clinical translation. In addition, this project will provide translational impetus for the use of dual-labeled PET/NIRF agents in the clinic.

The steric hindrance of the *ortho*-positioned iodine in Iodo-1502 resulted in low yield and lower radiolabeling efficiency. Therefore, we have synthesized new PET/fluorescence compounds with the same APC backbone, however with the radiolabeled iodines on the aromatic ring. The iodine positioning on the fluorophore shifts the excitation and emission properites of the Di-Iodo-1502 and Iodo-di-1502 to increasing wavelengths, and decreases the Stoke's shift. Further work will need to address the effect on the fluorescence quantum yield, and molar absorptivity on these new agents as

the fluorescence spectra has beens impacted. Additionally, radiolabeling and purification will also need to be assessed, and these PET/fluorescent APC analogs will need to be tested *in vivo* to confirm tumor targeting.

Chapter 4: APC Chelates for Targeted Magnetic Resonance Imaging and Multimodality Imaging and Therapy Platform

4A Introduction

Early detection and characterization of cancers continues to be a major challenge in the field of oncology. The development of robust imaging-based biomarkers has great potential to impact cancer patient survival and prognosis. Currently, in the field of clinical oncological imaging, positron emission tomography/computed tomography (PET/CT) with fluorodeoxyglucose remains the standard diagnostic imaging modality to detect and stage cancers due to its high sensitivity of detection[7]. However, the spatial resolution of PET is limited, with resolution on the order of millimeters, and PET/CT exposes patients to ionizing radiation in both the PET and CT portions of the exam[72-74]. Soft tissue and bone lesions at or below the resolution limit of PET can be missed or morphologically ambiguous on PET/CT imaging[75]. Despite its relatively high soft-tissue contrast and improved spatial resolution compared to PET, magnetic resonance imaging (MRI), has more limited applications in cancer staging[74]. The soft tissue contrast of magnetic resonance imaging (MRI) is unparalleled compared to PET and CT, and offers clinicians invaluable anatomical and morphological information for treatment planning and patient monitoring purposes[73]. This performance translates into improved diagnostic accuracy in head and neck, brain, spinal cord, breast, liver, bone, pelvic, and muscuoskeletal imaging[74-76]. However, malignancies can be more difficult to distinguish from normal tissues in MR imaging due to the lack of molecularly targeted MR contrast agents for cancer. The historical mismatch between the spatial resolution of an imaging modality (high in MRI/CT/radiography/ultrasound, low in PET/optical) and the sensitivity of the

imaging modality to molecular targeted agents (low in MRI/CT/radiography/ultrasound, high in PET/optical) has dampened the utility of MRI for oncological staging[74]. Importantly, if the low sensitivity of MRI to targeted contrast agents can be addressed, MRI would boast high spatial resolution, soft tissue contrast, and molecular sensitivity. This would greatly improve diagnostic accuracy, in particular in soft tissue regions. Additionally, with improved cancer staging performance of MRI, patient exposure to ionizing radiation exposure from PET/CT could be eliminated.

Owing to the low detection sensitivity of MRI, cancer-targeted MR contrasts agents with higher relaxivities are required to achieve detection. Currently, the majority of clinically approved contrast agents for MR are paramagnetic gadolinium chelates. These agents increase T1-weighted signal intensity by accelerating the longitudinal relaxation of surrounding water protons. However, lesion enhancement using these non-targeted agents is through the transient accumulation of contrast agent in tumor vasculature via the enhanced permeability and retention (EPR) effect. Therefore, uptake more accurately reflects aberrations in vascularity, permeability, and morphology rather than molecular differences between cancerous and normal tissue. Gd^{3+}-based clinical imaging agents exhibit relatively low relaxivities (<7 $mM^{-1}s^{-1}$)[77].

There has been substantial interest in developing targeted contrast agents for MRI to provide high-resolution imaging better matched to detecting smaller malignancies[78,79]. Recently, researchers have developed liver targeted MR contrast with sub-millimeter resolution of liver metastases, illustrating the potential for higher resolution imaging with targeted MR than can be provided by other modalities such as PET[80]. However, there have been no tumor-targeted FDA-approved MR contrast agents due to the many

challenges in developing these agents, including the low sensitivity of detection of MR to contrast agents and hence the relatively high doses and high relaxivity needed for imaging, and the lack of sufficiently highly expressed targetable markers[81,82]. Receptor-targeted MR agents have been explored, but have been disappointing due to the insufficient amount of uptake sufficient for MR contrast enhancement. Receptor-targeted MR agents have the additional drawback of altering cancer phenotype through receptor saturation[78]. Alkylphosphocholine analogs, however, can overcome many of the challenges associated with developing targeted MR agents due to their unique mechanism of selective uptake and retention[2]. APCs are selectively taken up through caveolae, lipid rafts that contain cholesterol and sphingolipids, which are overexpressed on cancer and cancer stem cells[2,3,83]. Their receptor-independent and unsaturable uptake may allow sufficient concentrations for contrast enhancement in cancer cells. In addition, our APC analogs have demonstrated avidity for cancer cells without uptake in benign lesions or inflammatory foci[15]. Of note, our radioidonated APC analogs have undergone human safety testing, demonstrate minimal toxicity in normal patients, and are in phase In order to exploit a wide variety of metal isotopes for image and therapy, we synthesized and characterized a new class of APC chelates for cancer targeted MRI, demonstrated their intracellular uptake and subcellular localization profile, and evaluated their multi-modality imaging and therapy potential.

Alkylphoshocholine analogs have demonstrated selective uptake and retention in over 60 rodent models of human cancer[2]. Radioiodoinated APC analogs can be used in a theranostic fashion for PET imaging and targeted radiotherapy (TRT). Furthermore, fluorescent analogs generated from the substitution of the iodine with bulkier cyanine

near-infrared fluorophores still yield tumor-targeted imaging agents for real-time margin illumination for intraoperative resection[12-14]. Importantly, these analogs have been shown to specifically target carcinoma, and not benign lesions or areas of inflammation, highlighting the versatility of these agents for diagnostic imaging and therapy agents[2].

We have recently extended our arsenal of APC analogs for multimodality imaging and therapy to include a new class of APC analogs, the APC chelates. The synthesis and successful tumor targeting of APC chelates would demonstrate an important step in creating one of the first targeted MR agents for broad-spectrum imaging of multiple cancer types. These new APC chelates address a historical mismatch between the spatial resolution of an imaging modality and the biologic activity of an imaging agent. Whereas PET has greater sensitivities but poor resolution, MR would provide the potential for higher-resolution imaging of smaller tumors better matched to the intracellular uptake of APCs. In this report, we highlight one of the first broad-spectrum targeted MR contrast agents for cancer imaging that exhibits high relaxivities compared with commercial agents. Importantly, we demonstrate for the first time high intracellular uptake of a targeted MR agent in tumor cells using transmission electron microscopy (TEM). These experiments not only suggest a non-saturable uptake mechanism for uptake of our APC-chelates, but also offer a method to more thoroughly describe the unique mechanism of selective uptake of this novel class of cancer-targeted compounds. We also report a novel methodology of Matrix-assisted laser desorption and ionization – time of flight (MALDI-TOF) mass spectrometry as a means of detecting the chemical speciation of our compound and commercial Gd chelates. This method is quite powerful and unique and resolving small molecules and their metabolites while preserving chemical speciation

information. Finally, we can derive the benefits of multimodality imaging through the APC chelates due to the myriad of chelatable radiometals that can be used for different modalities of imaging. As a proof-of-concept, we demonstrate this through the simultaneous PET/MR imaging using both targeted PET and MR APC chelates, ^{64}Cu-DOTA-APC and Gd-DOTA-APC, in rodent models of human cancer. The creation of our targeted MR agent may be a pivotal step towards earlier detection and treatment of cancer that may improve the survival and prognoses of cancer patients.

4B Materials and Methods:

Animals

All animal studies were performed in compliance with protocols approved by the University of Wisconsin-Madison Institutional Animal Care and Use Committee. All studies were performed on flank tumor bearing nude mice, nonobese diabetic/severe combined immunodeficient (NOD/SCID) mice with orthotopic GBMs (n=8), a flank bearing U87 nude athymic rat (n=1), nude athymic mice bearing A549 (n=3), PC3 (n=4), HT29 (n=3), TNB (n=4), and Miapaca (n=3). Briefly, cell lines were cultured and one to two million cells were injected into the right flank of twelve nude athymic mice, and grown to a diameter of 5-10mm2. For orthotopic models, stereotactic injection of one to two million U87 or glioblastoma stem cells (line 12.1) in the right striatum of immunodeficient NOD/SCID mice. APC analogs for injection were formulated as previously reported[1].

Chemical synthesis

All chemicals for Gd-DOTA-APC synthesis were purchased from Aldrich Chemical Co. (Milwaukee, WI). Thin-layer chromatography was performed using DC-Alufolien Kieselgel 60 F254 plates (E. Merck, Darmstadt, Germany). Visualization was achieved by UV light. NMR data were collected on Varian Unity-Inova 500 MHz NMR Spectrometer. Chemical shifts are reported in parts per million (ppm) relative to tetramethylsilane (TMS), and spin multiplicities are given as s (singlet), d (doublet), t (triplet), q (quartet), m (multiplet), or br m (broad multiplet). High-resolution mass spectra were obtained on a Bruker MaXis Ultra-High Resolution Quadrupole Time-of-Flight MS at the Analytical Instrumentation Center of UW School of Pharmacy.

(2) tribenzyl 2,2',2''-(1,4,7,10-tetraazacyclododecane-1,4,7-triyl)triacetate

Cyclen (2.00g,11.6mmol) and sodium acetate trihydrate (5.22g,38.3mmol) was suspended in 24mL DMA and cooled to -15°C in a methanol ice bath. A solution of $BrCH_2CO_2Bn$ (6.00mL, 38.3mmoL) in DMA (12.0mL) was added via cannula. Cooling was then removed and the mixture was stirred at RT for 72hr. The reaction was quenched with potassium bicarbonate, extracted with ethyl acetate, and washed with water. Stepwise silica column chromatography with $CHCl_3$:hexane (1:1), $CHCl_3$:hexane (2:1), $CHCl_3$:MeOH (97:3), and finally with $CHCl_3$:MeOH (97:3) eluted pure compound. Dried product is a yellow oil. Yield: 4.866g (60.1%). ^{1}H-NMR (500MHz, $CDCl_3$) 7.34 (m, 15H, ArH_5), 5.14 (s, 6H, OCH_2Ar), 3.49 (s, 4H NCH_2CO_2), 3.42 (br s, 2H NCH_2CO_2), 3.94 (s, 4H, (CH_2NHCH_2)), 2.87 (m, 12H, NCH_2CH_2N). HRMS: calculated for $C_{35}H_{45}N_4O_6$ (M^+) 617.333, found 617.334, calculated for $C_{35}H_{44}N_4O_6$ (M^++Na) 639.315, found 639.315.

(3) dibenzyl 2,2'-(4-(2-(benzyloxy)ethyl)-10-(2-(tert-butoxy)-2-oxoethyl)-1,4,7,10-tetraazacyclododecane-1,7-diyl)diacetate

Tribenzyl 2,2',2''-(1,4,7,10-tetraazacyclododecane-1,4,7-triyl)triacetate (or DO3A-tribenzylic acid ester) (4.82g, 6.90mmoL) was dissolved in acetonitrile (70mL). tert-Buty-bromoacetate (1.21mL, 8.28mmoL) and potassium carbonate (2.38g, 17.3mmol) were added to the solution. The reaction proceeded at room temperature with stirring for 24hr. The reaction mixture was filtered and purified with silica column chromatography using a stepwise gradient of $CHCl_3$:MeOH (99.25:0.75), $CHCl_3$:MeOH (98:2), $CHCl_3$:MeOH (95:5), and $CHCl_3$:MeOH (90:10). Dried product is a yellow oil. The product was dissolved in chloroform and treated with 1.20 equivalents (1.25g, 9.97mmol) of potassium carbonate to yield the HBr salt. Yield: 5.28g (94.5%). ^{1}H-NMR (500MHz, DMSO-d6) 7.34 (m, 15H, ArH_5), 5.14 (m, 6H, OCH_2Ar), 3.92 (m, 2H NCH_2CO_2), 3.73 (d, 4H NCH_2CO_2), 3.40 (s, 4H, $((CH_2)_2NHOtBu$), 3.08 (m, 12H, NCH_2CH_2N), 1.45 (d, 9H, $O(CH_3)_3$). HRMS: calculated for $C_{41}H_{54}N_4O_8$+H (M^++H) 731.401, found 731.400, calculated for $C_{41}H_{54}N_4O_8$+Na^+ (M^++Na) 753.383, found 753.383.

(4) (4,7,10-Tris-benzyloxycarbonylmethyl-1,4,7,10-tetraaza-cyclododec-1-yl)-aceticacid (tris-benzyl-DOTA)

Dibenzyl 2,2'-(4-(2-(benzyloxy)ethyl)-10-(2-(tert-butoxy)-2-oxoethyl)-1,4,7,10-tetraazacyclododecane-1,7-diyl)diacetate (4.33g, 5.92mmol) was dissolved in chloroform (28mL), and 4M hydrochloric acid in dioxane (10mL, 40.00mol) was added. Mixture was stirred at RT overnight under nitrogen. A white precipitate formed as the reaction proceeded. The mixture was filtered to remove impurities. Yield: 4.15 g (98.7%). 1H-

NMR (500MHz, DMSO-d6) 7.34 (m, 15H, ArH_5), 5.14 (br m, 6H, OCH_2Ar), 4.03 (m, 6H NCH_2CO_2Bn), 3.83 (s, 2H, NCH_2CO_2H) 3.3 (br m, 16H, NCH_2CH_2N), HRMS: calculated for $C_{37}H_{46}N_4O_8+H^+$ (M^++H) 675.339, found 675.337, calculated for $C_{37}H_{46}N_4O_8+Na^+$ (M^++Na) 697.321, found 697.320.

(6) ethan-1-ylium-2-yl (18-(4-(2-(4,7,10-tris(2-(benzyloxy)-2-oxoethyl)-1,4,7,10-tetraazacyclododecan-1-yl)acetamido)phenyl)octadecyl) phosphate compound with trimethylamine (1:1) 2-(4,7,10-tris(2-(benzyloxy)-2-oxoethyl)-1,4,7,10-tetraazacyclododecan-1-yl)acetic acid (1.48g, 2.08mmol) and 18-(4-aminophenyl)octadecyl (2-(trimethylammonio)ethyl) phosphate22 (914mg, 1.74mmoL) were suspended in 50.0mL chloroform. Triethyl amine (866µL, 6.25mmol) and the co3upling agent COMU (891mg, 2.08mmol) were added to the reaction mixture. Reaction proceeded overnight at RT with stirring. The reaction turned yellowish orange within minutes, and appeared a clear yellow solution the next morning. The product was extracted with $CHCl_3$:MeOH:H_2O (8:8:7.2), and the organic layer was dried with sodium sulfate, and filtered. The product was purified using silica column chromatography using a stepwise gradient $CHCl_3$:MeOH (9:1), $CHCl_3$:MeOH (9:2), $CHCl_3$:MeOH (1:1), $CHCl_3$:MeOH:H_2O (65:25:3), and $CHCl_3$:MeOH:H_2O (65:25:4). Product is a yellow amorphous solid. Yield: 1.28g (63.0%). ^{1}H-NMR (500MHz, $CDCl_3$) 7.56, 7.51, 7.09, 7.02 (4d, 4H, ($CONHArH_4$), 7.34 (m, 15H, ArH_5), 5.14 (m, 6H, OCH_2Ar), 4.24 (m, 2H, $PO_4CH_2CH_2NMe_3$), 3.87 (q, 2H, $(CH_2)_{17}CH_2PO_4$), 3.60 (m, 2H, $PO_4CH_2CH_2NMe_3$), 3.49 (s, 4H NCH_2CO_2), 3.10-4.20 (br m, 16H, NCH_2CH_2N), 2.55 (q, 2H, $ArCH_2(CH_2)_{17}$), 1.64 (m, 2H, ($ArCH_2CH_2(CH_2)^{16}$), 1.56 (m, 2H, $(CH_2)_{16}CH_2CH_2PO_4$), 1.45 (br m, 28H,

$CH_2(CH_2)_{14}CH_2$). HRMS: calculated for $C_{66}H_{99}N_6O_{11}P^+$ $2Na_2^+$ (M^++2Na) 614.345, found 614.345.

(7) 2-(trimethylammonio)ethyl (18-(4-(2-(4,7,10-tris(carboxymethyl)-1,4,7,10-tetraazacyclododecan-1-yl)acetamido)phenyl)octadecyl) phosphate

Compound 6 (1.22g, 1.03mmol) was dissolved in 25.0mL EtOH and palladium on carbon, 10% weight (279mg, 2.62mmol) was added. The mixture was decanted into a hydrogenation bottle. The bottle was vacuumed and filled with H2 at an initial pressure of 52.0 PSI. The reaction proceeded with shaking at RT overnight. The compound was precipitated with acetone to yield the final product, an amorphous white solid. Yield: 943 mg (65.0%). ^{1}H-NMR (500MHz, $CDCl_3$) 7.46, 7.12 (2d, 4H, ($CONHArH_4$), 4.26 (m, 2H, $PO_4CH_2CH_2NMe_3$), 3.92 (q, 2H, $(CH_2)_{17}CH_2PO_4$), 3.56 (m, 2H, $PO_4CH_2CH_2NMe_3$), 3.49 (s, 4H NCH_2CO_2), 3.38 (s, 2H, NCH_2CONH), 3.15 (s, 9H, $N(CH_3)_3$), 2.57 (t, 2H, $ArCH_2(CH_2)_{17}$), 1.58-1.65 (br m, 4H, ($ArCH_2CH_2(CH_2)_{16}$ and CH_2CH_2O), 1.30 (m, 28H, $CH_2(CH_2)_{14}CH_2$). HRMS: calculated for $C_{45}H_{81}N_6O_{11}P^+H^+$ (M^++H) 913.577, found 913.577, calculated for $C_{45}H_{81}N_6O_{11}P^+Na^+$ (M^++Na) 935.559, found 935.558, calculated for $[C_{45}H_{81}N_6O_{11}P+2H]^{2+}$ ($[M+2H]^{2+}$) 457.292, found 457.292.

(8) Gado-2-(trimethylammonio)ethyl (18-(4-(2-(4,7,10-tris(carboxymethyl)-1,4,7,10-tetraazacyclododecan-1-yl)acetamido)phenyl)octadecyl) phosphate

2-(trimethylammonio)ethyl (18-(4-(2-(4,7,10-tris(carboxymethyl)-1,4,7,10-tetraazacyclododecan-1-yl)acetamido)phenyl)octadecyl) phosphate (513mg, 0.562mmol) was dissolved in pyridine (5.00 mL) and MeOH (7mL), and solution of

gadolinium chloride hexahydrate in water (0.700mL) was added to the reaction solution. White precipitate formed immediately. Mixture was slightly warmed with a heating gun with stirring. After 10min, the precipitate was dissolved, and the slightly cloudy mixture was stirred at RT for 24hr. Silica column chromatography with $CHCl_3$:MeOH (8:2; 5:5; 10:8), then $CHCl_3$:MeOH:conc NH_4OH (10:8:2; 10:8;2.5). Compound was dried under high vacuum, redissolved in $CHCl_3$:MeOH (2mL), and acetone (50mL) was added. The mixture was evaporated, and the residue formed a white powder. Yield: 600mg (75.0%). HRMS: calculated for $C_{45}H_{78}GdN_6O_{11}P^+H^+$ (M^++H) 1068.479, found 1068.475, calculated for $C_{45}H_{78}GdN_6O11P^+Na^+$ (M^++Na) 1090.461, found 1090.457, calculated for $C_{45}H_{78}GdN_6O_{11}P^+K^+$ (M^++K) 1106.434791, found 1106.431.

Chelation of ^{64}Cu-DOTA-APC and ^{177}Lu-DOTA-APC

For ^{64}Cu and ^{177}Lu radiolabeling, DOTA was reacted with $^{64}CuCl_2$ or $^{177}LuCl_3$ in approximately 300μL of NaOAc buffer (0.1 M, pH = 4.5) at 37 ºC for 30 min, under constant shaking. The radiolabeled APC was then separated by Oasis HLB Sep Pak by loading the radioloabeled products on the column with water, and eluting the compound with EtOH.

Transmission Electron Microscopy and Scanning Transmission Electron Microscopy Studies

To observe uptake of Gd-DOTA-APC in cancer and control cells with transmission electron microscopy (TEM), U87 cells were plated on coverslips in DMEM, 10% FBS, and 1% P/S overnight. Cells were treated for 0hr, 6hr, and 24hr with 1μM of Gd-DOTA-APC,

and then fixed in 2.5% glutaraldehyde, 2.0% paraformaldehyde in 0.1M sodium phosphate buffer (PB), pH 7.4 for ~1 hrs. Cells were then rinsed and then post-fixed in 1% osmium tetroxide, 1% potassium ferrocyanide in PB for ~1hr. Cells were then dehydrated in a graded ethanol series (35, 50, 70, 80, 90% for 5 minutes, 95% for 10 minutes, 100% for 3 x 10 minutes) then transitioned in propylene oxide (PO) 2 x 7 minutes. Durcupan ACM (Fluka AG, Switzerland) resin was used during infiltration and embedding. Increasing concentrations of accelerated (10ml A/M, 10ml B, 300µl C, 100µl D components) Durcupan were used for infiltration. The cultures were embedded in open aluminum weighing dishes at 60°C in a drying oven overnight until polymerized. The samples were then treated with concentrated hydrofluoric acid, glass side down, for approximately 15 minutes to etch off the glass, revealing the embedded cell culture. Samples were sawed out in $5mm^2$ pieces, glued to prepared blank using a Leica EM UC6 ultramicrotome. Ultrathin sections were collected (100 nm) on 300 mesh Cu thin-bar grids, and contrasted with Reynolds lead citrate and 8% uranyl acetate in 50% EtOH. The sections were observed with a Philips CM120 transmission electron microscope, and images were documented with an AMT BioSprint12 (Advanced Microscopy Techniques, Corp. Woburn, MA) side mounted digital camera.

For Scanning transmission electron microscopy (STEM) imaging, U87 cells were prepared in the same fashion minus treatment with osmium tetroxide to eliminate potential heavy metal contaminations. Samples were ash treated prior to imaging. High Z-contrast scans were performed on the Technai F30 (Fei Company, Hillsboro Oregon) to detect heavy metal inside the biosamples.

Relaxivity Measurements

Relaxivity of Gd-DOTA-APC was characterized at 1.5T and 3.0T (GE Signa HDxt and Signa PET/MR, GE Healthcare, Waukesha, WI) at 37°C. Gd-DOTA-APC samples were prepared at concentrations of 0.125-1 mM in water, human plasma, and human serum albumin. Samples were held at 37°C with an MR-compatible sample holder and warm water circulation system. For T1 measurement, an inversion recovery pulse sequence with TI=50-750ms, TR=4000ms/5000ms (1.5T/3.0T), and TE=8-9ms was utilized. For T2 measurement, a CPMG sequence with TR=5000ms and TE=25-400ms was utilized. T1 and T2 times were estimated using nonlinear least squares fitting of the signal magnitude vs. inversion time and echo time, respectively. Longitudinal (r1) and transverse (r2) relaxivities of Gd-DOTA-APC were estimated from the slope of the linear relationship between relaxation rate and agent concentration.

Stability of APC-Chelate

To examine the stability of Gd3+ in the Gd-DOTA-APC complex, Chelex solid phase extraction was used to separate free Gd3+ from Gd-DOTA-APC dissolved in buffer and measured by magnetic-sector ICPMS after microwave digestion as previously reported (2) (ref).

Tumor Model Imaging

Gd-DOTA-APC was administered intravenously (approximately 0.12mg/kg) in 9 rodent models of human cancer. These models include two orthotopic glioblastoma models (U87, n=7 and a patient-derived glioblastoma stem cell model GSC 115, n=1), an

αβ-overexpressing triple negative breast cancer model (n=4), a rat glioblastoma flank xenograft model (U87, n=1), a flank model of prostate cancer (PC3, n=3), a non-small cell lung cancer (A549, n=3), colorectal cancer (HCT116, n=3), pancreatic cancer (n=3), and glioblastoma (U87, n=3). In vivo imaging was performed on a 4.7T preclinical scanner (Agilent Technologies, Santa Clara, CA) pre-contrast, following i.v. contrast administration, and at multiple time points for up to seven days. R1 maps were estimated using 3D Spoiled gradient (SPGR) acquisitions with variable flip angles and B1 field correction [3]. To compare uptake of Gd-DOTA-APC to the clinical agent Dotarem, a flank xenograft glioma model (U87) was used (n=3). To assess tumor specific uptake, the tumor to muscle R1 ratio was computed across multiple time points in two models.

A rat flank model was created to assess the dual-modality imaging potential of simultaneous PET/MR. Approximately 1 million U87 cells were injected in the right flank. Imaging was performed when the tumors reached 2.5 cm in diameter after simultaneous delivery of targeted PET and MR agents, 64Cu-DOTA-APC and Gd-DOTA-APC.

Simultaneous PET and MR Imaging

For simultaneous PET/MR of a rat tumor model, ^{64}Cu-DOTA-APC (20mCi/kg) and Gd-DOTA-APC (0.12mg/kg) were mixed and injected intravenously. Simultaneous PET/MR imaging was performed on a clinical 3T PET/MRI scanner using the built-in posterior array coil (Signa PET/MR, GE Healthcare, Waukesha, WI). Sagittal 3D T1-weighted gradient echo (TE=3.3ms, TR=7.7ms, pixel size=0.51x0.51x1 mm3, pixel bandwidth=244 Hz, flip angle=15-degree, scan time=4:53) and sagittal 3D CUBE-Flex

(TE=83.4ms, TR=2500ms, ETL=100, pixel size=0.9x1.4x1.0 mm3, pixel bandwidth=326 Hz, scan time=5:41) images were obtained.

Biodistribution studies

U87 flank-bearing mice (n=3) were injected with Gd-DOTA-APC. Seventy-two hours following administration of Gd-DOTA-APC, animals were humanely anesthetized and perfused with saline before organs were harvested. Tissue samples were sectioned and homogenized using ceramic blades and Teflon implements, and 20-25mg of homogenized wet tissue is transferred to a Teflon digestion vessel. Organic matrix removal and complete solubilization of gadolinium and other trace major elements in the tissues is effected by microwave-assisted acid digestion in Teflon mini-bombs. Gadolinium and a suite of 8-10 additional elements in the tissue digests were quantified using high-resolution (magnetic-sector) inductively-coupled plasma mass spectrometry (SF -ICPMS).

MALDI-TOF Imaging studies of Animal Tissues

Tissues were perfused and harvested from nude athymic mice bearing U87 and A549 flank xenografts. T1-weighted enhancement of the flank xenografts and organs of metabolism verified contrast uptake in the tumors before euthanasia at 24hr, 48hr, and 72hr after Gd-DOTA-APC delivery. Tissues were immediately flash frozen, then homogenized or sectioned for MALDI imaging on ITO coated glass slides at 12μm thickness. Either CHCA or DHB matrix will be applied by TM-Sprayer from HTX Imaging (Chapel Hill, NC) to the tissue and allowed to dry before imaging. MALDI mapping was

performed on the biological samples, and imaged using Bruker Ultraflex Extreme MALDI TOF/TOF mass spectrometer (Billerica, MA). Analysis of mass ranges 0 m/z to 2000 m/z will hopefully identify our Gd chelate and any potential small molecule metabolites including free Gd in the tumors and organs of interest. Further analysis of Gd binding to proteins will be performed by searching for the isotopic footprint of Gd in the protein mass ranges.

Statistical Analysis

Statistical analyses were performed with Microsoft Excel version 15.0.4779.1002 or GraphPad Prism 5.0. Paired t-Tests were used to determine differences. All p-values <0.05 were considered significant. Three mice per time point were used for biodistribution studies.

4C Results

Synthesis and Chelation of APC-chelates

Cyclen was converted into DO3A tri-benzyl ester in a procedure analogous to the preparation of DO3A tris-(t-Bu ester)[84] (Figure 4.1). Then, the fourth (unsubstituted) nitrogen in DO3A was alkylated with t-butyl bromoacetate. Deprotection of t-Bu ester resulted in DOTA tri-benzyl ester. This compound was coupled with 18-(p-amino-phenyl) octadecyl phosphocholine using COMU coupling reagent[85]. The benzyl groups were removed by the catalytic hydrogenation in the coupling product. Gd, ^{64}Cu, or ^{177}Lu was subsequently chelated onto DOTA-APC via standard methods.

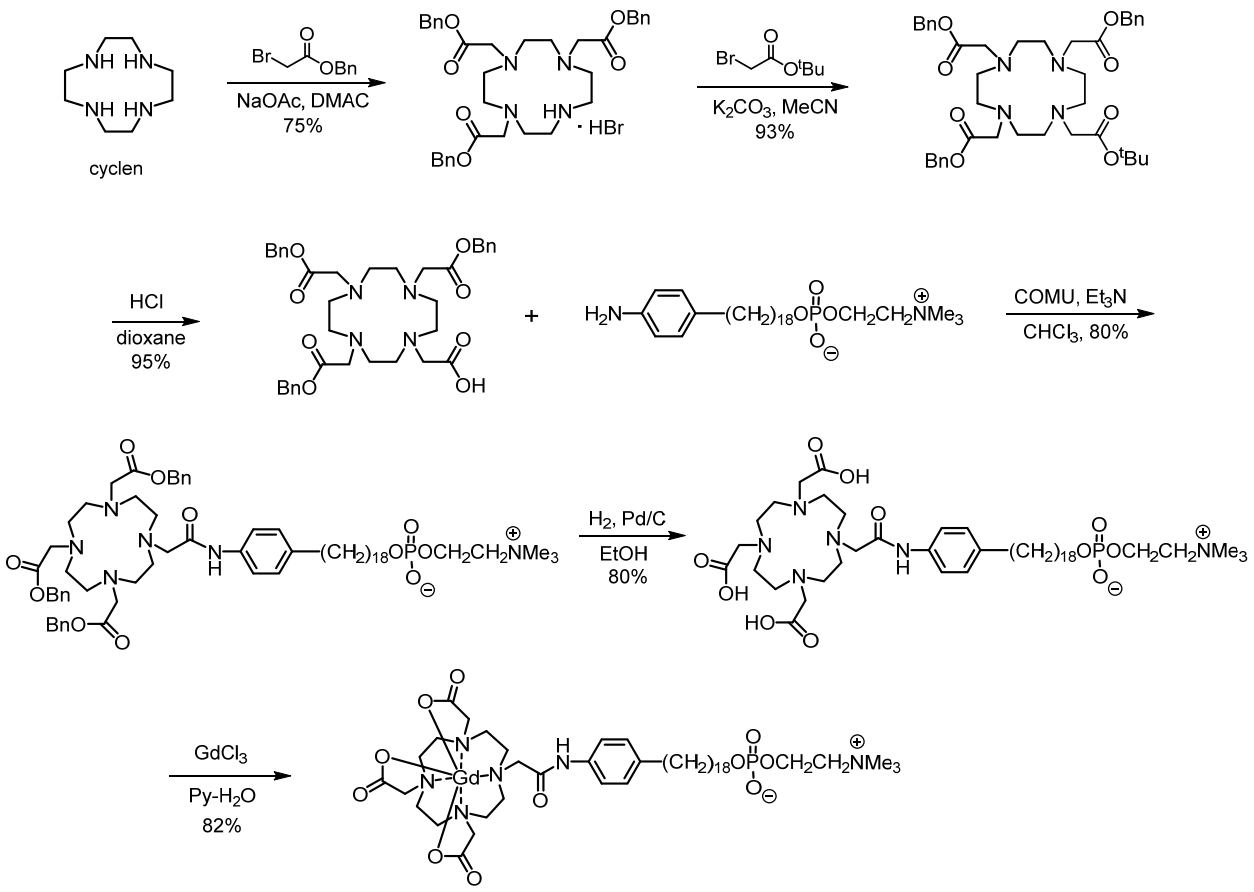

Figure 4.1. Chemical synthesis of Gd-DOTA-APC. Cyclen was converted into DO3A tri-benzyl ester, differentially protected with three benzylic acid arms and a tert-butyl acid. t-Butyl acid was deprotected and conjugated to the APC through an amide linker, subsequently followed by the chelation of Gd with $GdCl_3$.

Gd-DOTA-APC Exhibits High Relaxivity and High Stability

The T1 and T2 relaxivities of Gd-DOTA-APC in water and human plasma were measured. For relaxivity measurements, conicals containing 0.125 mM of Gd-DOTA-APC were stabilized in a water bath and warmed to 37°C (Fig 4.2). At 1.5T and 3.0T, the measured longitudinal relaxivity (r1) was between 8.45-16.5 s^{-1}/mM for all preparations, while transverse relaxivity (r2) varied from 20-25.7 s^{-1}/mM (Fig 4.2). The high longitudinal

relaxivity of this agent compares favorably to conventional agents with r1 values ranging from 3.5-7.0 s^{-1}/mM at 1.5T and 2.5-6.5 s^{-1}/mM at 3.0T[77].

The stability of Gd-DOTA-APC is of significant interest due to recent findings of Gd deposition in the brain[86,87]. It still remains unclear if contrast enhancement in the globus pallidus and dentate nucleus pose clinical concerns as no symptoms have been correlated to the enhancement. The macrocyclic chelator DOTA was specifically chosen to chelate Gd because of excellent kinetic and thermodynamic stability, and has not been shown to deposit in the brain[88-90]. Nevertheless, the stability of Gd-DOTA-APC was investigated using a Chelex solid phase extraction method[91]. A Chelex column was used to separate free Gd^{3+} from Gd-DOTA-APC dissolved in buffer and measured by magnetic-sector ICPMS after microwave digestion. The initial free fraction of Gd^{3+} in buffer at room temperature was found to be 0.081%, consistent with other macrocyclic Gd^{3+} agents[88].

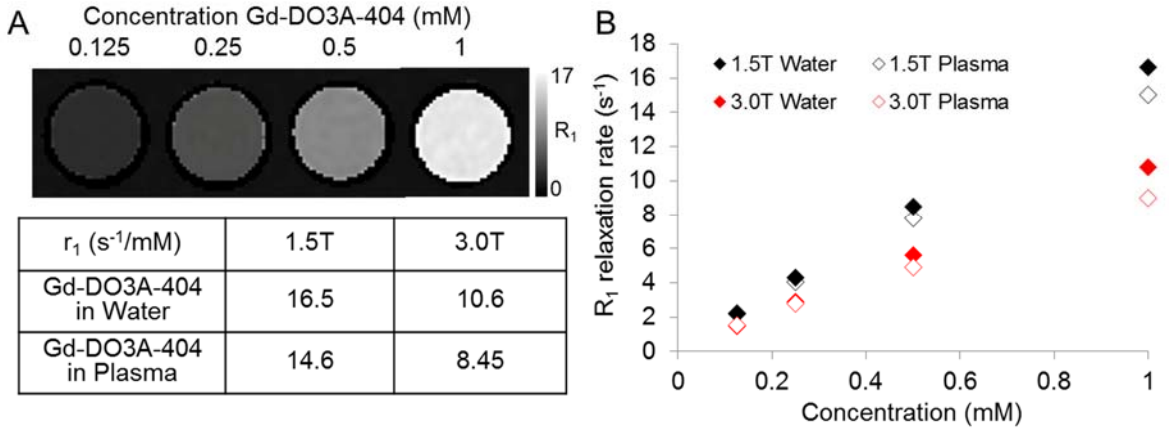

r_1 (s^{-1}/mM)	1.5T	3.0T
Gd-DO3A-404 in Water	16.5	10.6
Gd-DO3A-404 in Plasma	14.6	8.45

Figure 4.2. Relaxivities of Gd-DOTA-APC at 1.5T and 3.0T. Longitudinal relaxivity (r1) of Gd-DO3A-404. (A) Representative R1 maps of Gd-DO3A-404 in water at 1.5T and r1 values at 1.5T and 3.0T in water and plasma. (B) Longitudinal relaxivity was determined by linear fitting of R1 rate versus sample concentration at each field strength and for each solvent. Gd-DO3A-404 was found to have greater r1 values at 1.5T and when prepared in water.

Transmission Electron Microscopy Studies Confirms Selective Uptake in Cancer Cells

A time-course TEM study of U87 cells incubated with 1μM of Gd-DOTA-APC reveals a novel mechanism of selective uptake in cancer cells by APC compounds. At six hours of incubation of cells with Gd-DOTA-APC, dense clusters of Gd-rich spheres were observed within subcellular vesicles, which correspond to endosomes (Figure 4.3B-D). These clusters are not seen in untreated cells (Figure 4.3A). STEM imaging of the U87 cells confirmed heavy metal uptake inside the U87 cells corresponding to Gd (Figure 4.3 E-F). These studies point to an endosomal uptake mechanism of APC compounds, which has not been reported in the literature, suggests a mechanism of classical fluid-phase endocytic uptake. Classical fluid-phase endocytic uptake can be mediated through two mechanisms: clathrin-dependent and caveolar uptake[92-94]. As the fixation process distorts membrane architecture, it remains difficult to distinguish between these two mechanisms. However, the large numbers of Gd-DOTA-APC molecules within these cancer cells suggests a non-saturable, non-receptor mediated uptake mechanism. The evidence suggests a caveolar mechanism of uptake, which is consistent with previous confocal microscopy studies of APC and APC-like molecule uptake[2,94,95]. Notably, no dense clusters corresponding to gadolinium are observed in the nucleus, which is also consistent with previous studies that show no nuclear uptake of APCs and APC-like molecules[2,94,95] (Figure 4.3B). Taken together, these studies offer insight into a unique mechanism of selective uptake and possibly retention of APC compounds by cancer cells that may be universal across different cancer types.

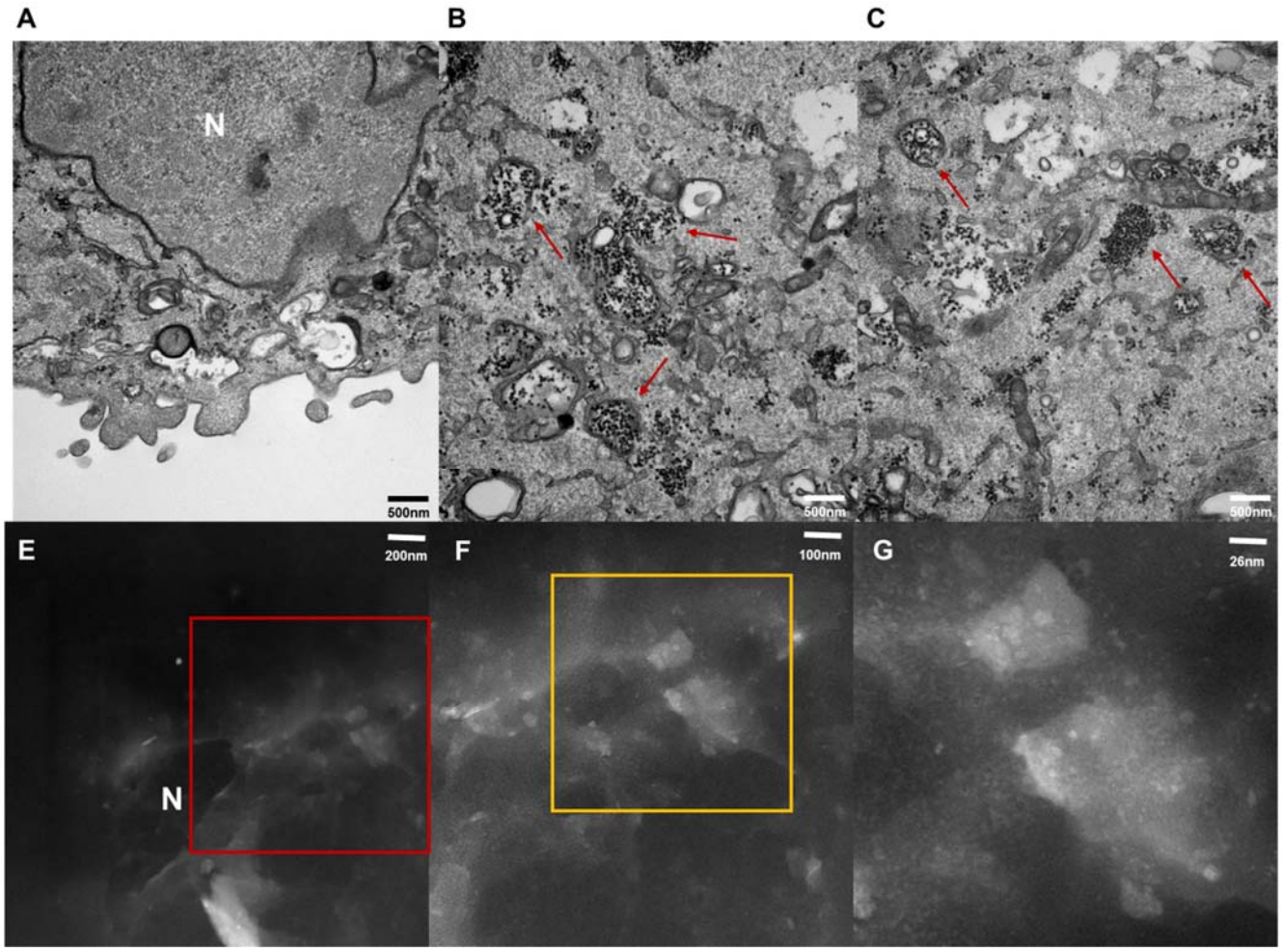

Figure 4.3. Tumor uptake of Gd-DOTA-APC in U87 in vitro. (A-C) Transmission electron microscopy images of a U87 cell treated with 1uM Gd-DOTA-APC at 25K magnification. Red arrows indicate endosomal uptake of the compound. (E-F) High Z-contrast scanning transmission electron microscopy images of a U87 indicating heavy metal inside the cell. N denotes nucleus. Red and yellow boxes are zoomed in areas, with the images on the subsequent right panels.

T1-Weighted Imaging Demonstrates Selective Uptake in Multiple Cancer Models

In vivo uptake of Gd-DOTA-APC was initially characterized in two flank xenograft models of human cancer, A549 (non-small cell lung cancer) and U87 (glioma). T1-weighted MR images and T1 maps were acquired in all subjects prior to intravenous contrast administration, and imaging was repeated at multiple time points up to seven days (Fig 4.4). Flank tumors of both models showed tumor-specific enhancement over

the 7 day period. Significantly sustained enhancement, quantified by tumor to muscle signal ratio, was maintained for up to 4 and 7 days in A549 and U87, respectively. T1 maps acquired at pre-contrast and 48 hour time points confirmed that a significant increase in R1 relaxation rate was observed at 48 hours post-contrast in both tumor models.

A number of other tumor models were investigated to further demonstrate the broad-spectrum uptake of Gd-DOTA-APC in cancer including colorectal flank xenograft models (HT29, HCT116, n=3 each), a flank xenograft prostate cancer model (PC3, n=3), an orthotopic αβ-overexpressing triple negative breast cancer model[96] (n=4), pancreatic cancer (MiaPaca, n=3), and two orthotopic brain cancer models (U87 n=7 and a cancer stem cell model n=1). Prolonged T1-weighted signal enhancement was observed in all of these models between 24hr and 96hr of imaging following Gd-DOTA-APC administration (Figure 4.4). The results suggest a broad-spectrum uptake mechanism in all cancer models tested. Importantly, with this new APC chelate, we are able to correlate gross macroscopic imaging findings with subcellular intracellular uptake (Figure 4.3). These proof-of-concept studies offer tremendous potential into discovering a unique mechanism of selective uptake in many different cancer types. Further studies will hopefully address more mechanistic insights into a broad-spectrum cancer-targeting mechanism.

The in vivo uptake of Gd-DOTA or Dotarem® (gadoterate meglumine), Gd^{3+} chelated by DOTA, was investigated in mouse hindlimb tumors to compare the temporal dynamics of MRI signal enhancement to those of Gd-DOTA-APC. Three nude athymic mice with U87 flank xenografts were scanned with a T1-weighted sequence prior to

administration of Dotarem®, immediately following contrast administration, and at multiple time points up to 24 hours. The T1-weighted tumor to muscle signal ratio with Dotarem® rapidly increased over the course of five minutes, reduced over the course of one hour, and had returned to baseline signal levels at 24hr (Figure 4.4). Dotarem® administration increased ratio of tumor to muscle T1-weighted signal from 1.15 pre-contrast to 1.67 five minutes post-contrast. In comparison, as a result of Gd-DOTA-APC administration, tumor to muscle signal ratio increased from 1.24 pre-contrast to a maximum of 2.12 at 24 hours post-contrast. This study suggests increased uptake and prolonged retention of Gd-DOTA-APC in cancer cells that is not seen with the extracellular macrocylic agent Dotarem®.

Next, biodistribution in tumor-bearing mice was assessed at 72hr following administration of Gd-DOTA-APC and quantified using ICP-magnetic sector. Organs from three U87 flank bearing mice were harvested, and the amount of Gd in the different tissues was quantified. Gd content in the tumor (14.0μg/g of tissue) was higher than in all other tissues except the organs of clearance, the liver and kidney (Figure 4.5D).

T1-weighted imaging of the whole animal over a period of 7 days was also used to observe the pharmacokinetics and circulation of Gd-DOTA-APC. T1-weighted imaging of the abdomen demonstrated Gd-DOTA-APC clearance from the liver, kidneys, and blood over the 7-day period. Twenty-four hours following contrast administration, little observable agent remained in circulation. High uptake in the liver and kidneys was observed, with maximum liver signal 24 hours and maximum kidney uptake one hour following contrast administration. The contrast enhancement in the different abdominal organs is consistent with *ex vivo* biodistribution data.

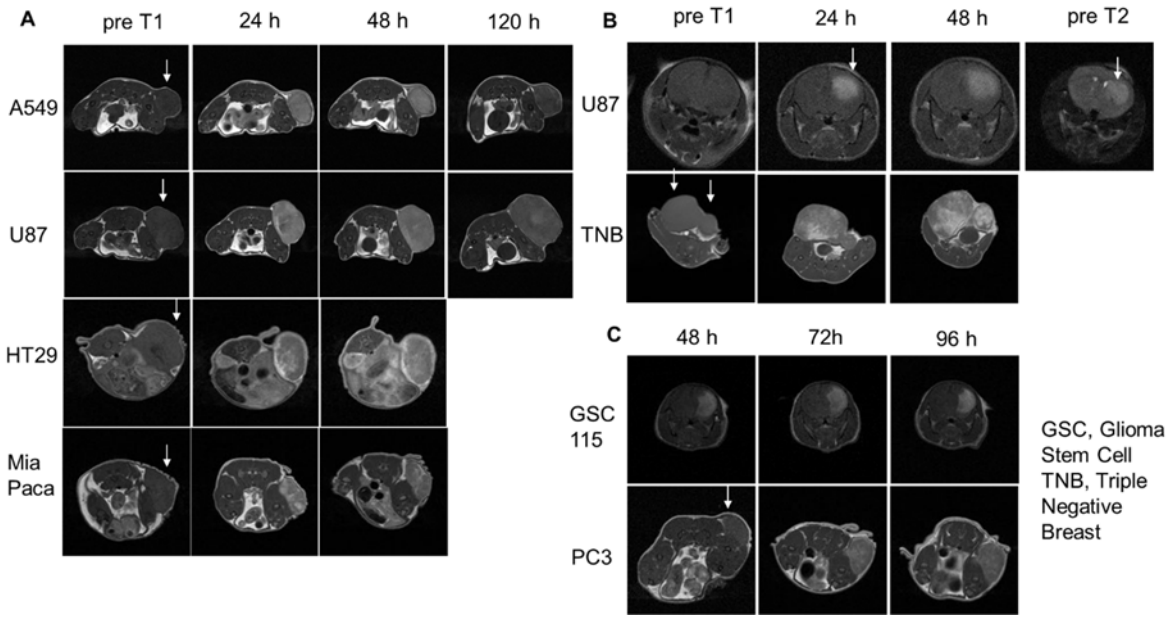

Figure 4.4. Tumor uptake of Gd-DOTA-APC in Multiple Cancer Models. (A) Representative T1-weighted images of four flank xenograft tumor models including A549 (NSCLC), U87 (GBM), HT29 (colorectal) and MiaPaca (Pancreatic cancer) pre-contrast and at multiple time points up to 5 days post-contrast. Tumor location indicated by white arrow. (B) T1-weighted images of two orthotopic tumor models - a U87 and a triple negative breast mammary cancer- pre-contrast and at multiple time points up to 5 days post-contrast. Tumor location indicated by white arrow. (C) (Supplemental) Representative T1-weighted images of a glioblastoma cancer stem cell model and a prostate cancer model pre-contrast and up to 96hr.

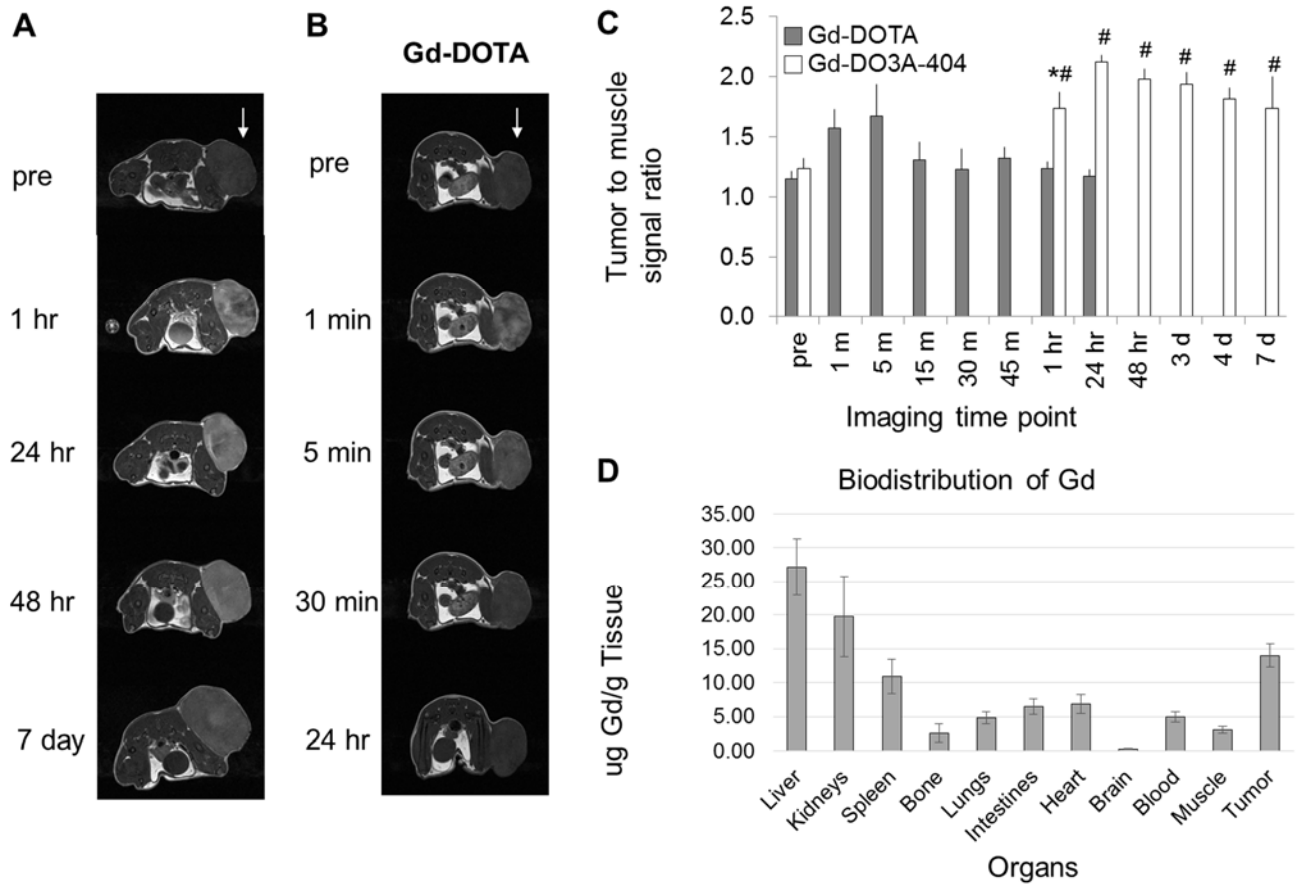

Figure 4.5. Uptake of Gd-DOTA-404 in U87 xenograft model. (A) Representative T1-weighted images of a U87 tumor pre-contrast and at multiple time points up to 7 days following Gd-DOTA-404 administration (tumor=white arrow). (B) Representative T1-weighted images of a U87 tumor following Dotarem delivery. (C) Time course of T1-weighted signal enhancement after delivery of Gd-DOTA-404 and Gd-DOTA (Dotarem) in U87 shows that Gd-DOTA-404 enhancement is greater and more prolonged, indicating that uptake reflects specific targeting and incorporation of the contrast agent in cancer cells. (*p<0.05 compared to pre-contrast, Dotarem; #p<0.05 compared to pre-contrast, Gd-DOTA-404.)

Simultaneous PET/MR Imaging of Rat Bilateral Flank Xenografts Demonstrates Proof-of-Concept Multi-modality Imaging

The proof-of-concept multi-modality imaging potential of APC chelates was demonstrated in a U87 flank xenograft in a rat co-injected with 5mCi (20mCi/kg) of ^{64}Cu-DOTA-APC and Gd-DOTA-APC. In vivo simultaneous PET/MR imaging was performed at 24 and 48 hours following contrast delivery. Co-localization of PET and T1-weighted

signal enhancement was observed in the liver, intestines, kidneys, and flank xenograft at both imaging time points, suggesting similar pharmacokinetics and biodistribution of ^{64}Cu-DOTA-APC (Figure 4.6). This is striking given that the Gd-DOTA-APC was given at >1000 mass dose compared to the 64Cu-DOTA-APC, again illustrating the potential receptor-independent mechanism of uptake and lack of saturability of APC analogs.

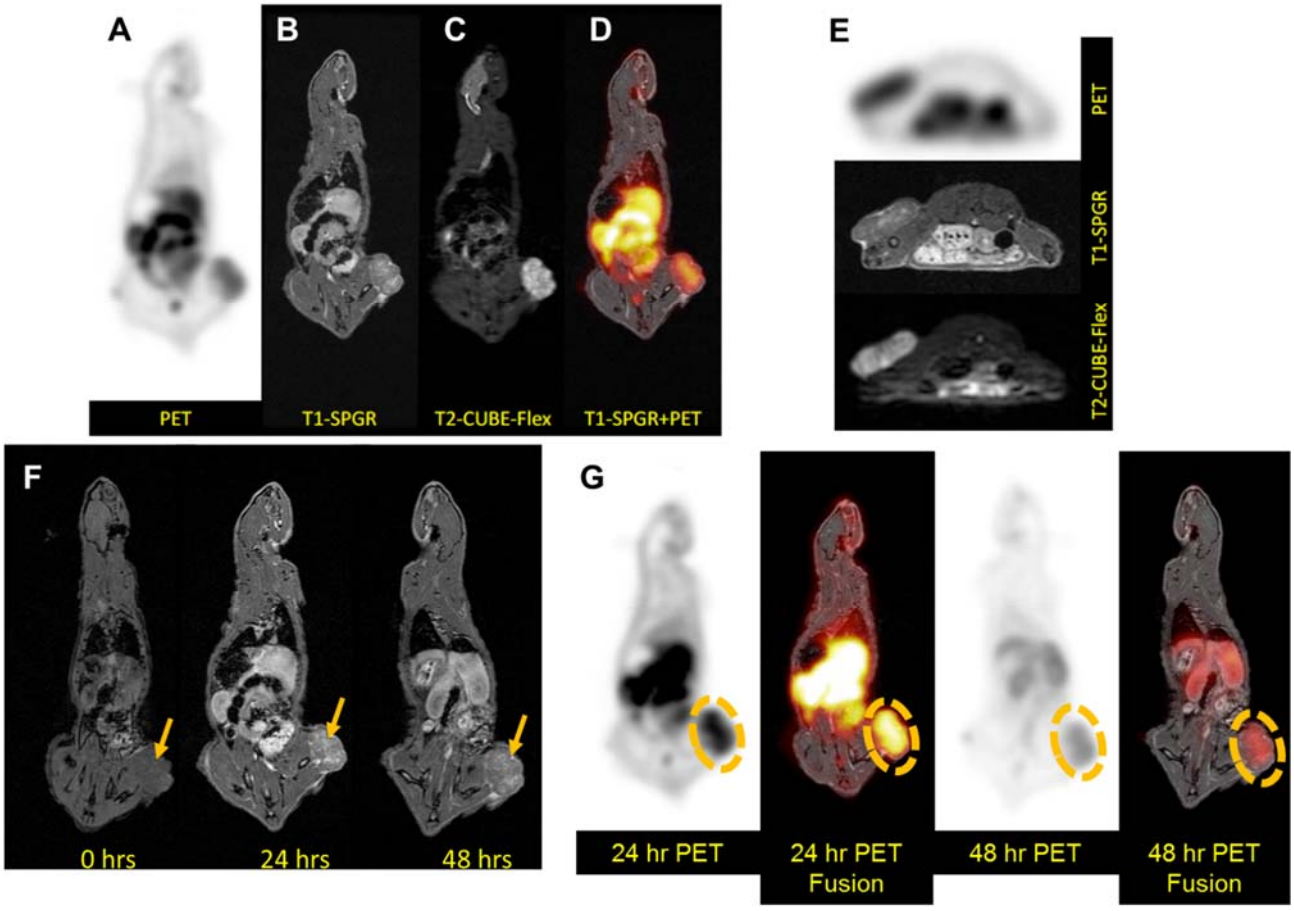

Figure 4.6. Simultaneous PET/MR Imaging of a Rat Flank Xenograft on a 3.0T Clinical Scanner (A) Sagittal PET image of a rat co-injected with 5mCi (20mCi/kg) of 64Cu-DOTA-APC and Gd-DOTA-APC 24h post-injection. (B-C) T1-weighted and T2-weighted images of the sagittal section of the rat at 24h. (D) Fused images of the A and B. (E) Axial PET and T1 and T2 weighted images of the same rat flank tumor. (F) T1-weighted scans precontrast, 24h and 48h. (G) PET and PET/MR fusion at 24h and 48h. Yellow arrows and circles denotes location of the flank xenograft.

MALDI-TOF Imaging of Gd chelates in Tissues

MALDI mass spectrometry was performed on equimolar mixture of Dotarem, Multihance, and Gd-DOTA-APC. Using this technique, the chemical speciation of these different Gd chelates was able to be resolved (Figure 4.7). The isotopic fingerprint of Gd is unique and gives high diagnostic accuracy.

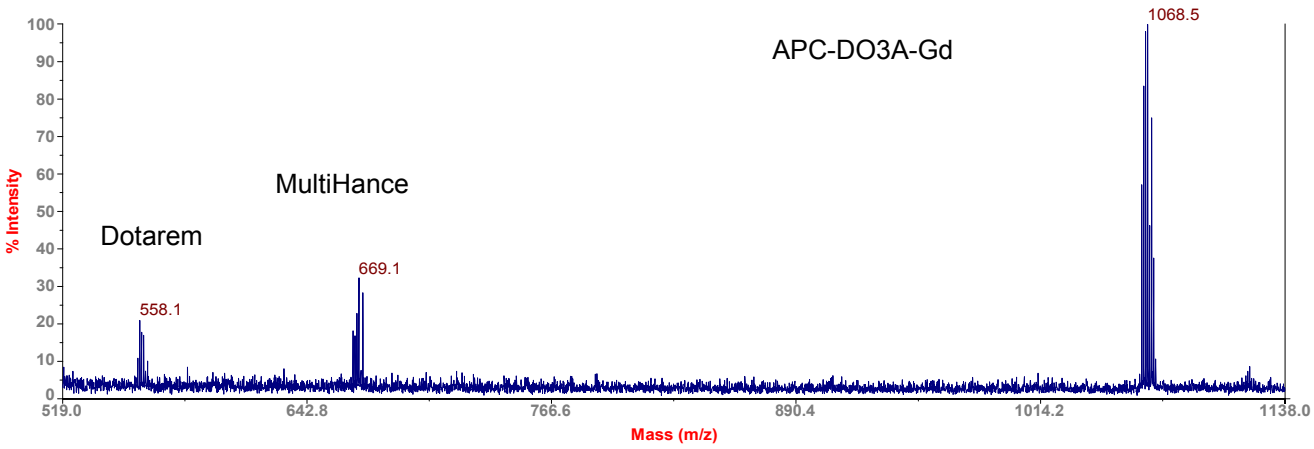

Fig 4.7. Mass spectrum of an equimolar mixture of Dotarem, Multihance, and Gd-DOTA-APC in CHCA showing unique multi-Gd isotope finger print pattern and easy mass resolution of the 3 different MR contrast agents.

MALDI mass spectra from tumor homogenates were also collected. U87 and A549 flank xenografts were harvested at 24h and 72h post-administration of Gd-DOTA-APC. Homogenates were mixed and co-crystallized with CHCA or DHB. MALDI mass spectrometry revealed presence of Gd-DOTA-APC and Gd-DOTA-APC adducts (formed from sodium and phosphorous) in both tumors (Figure 4.8). Scanning for the unique isotopic fingerprint of Gd did not reveal any Gd species in the 0-2000 *m/z* range.

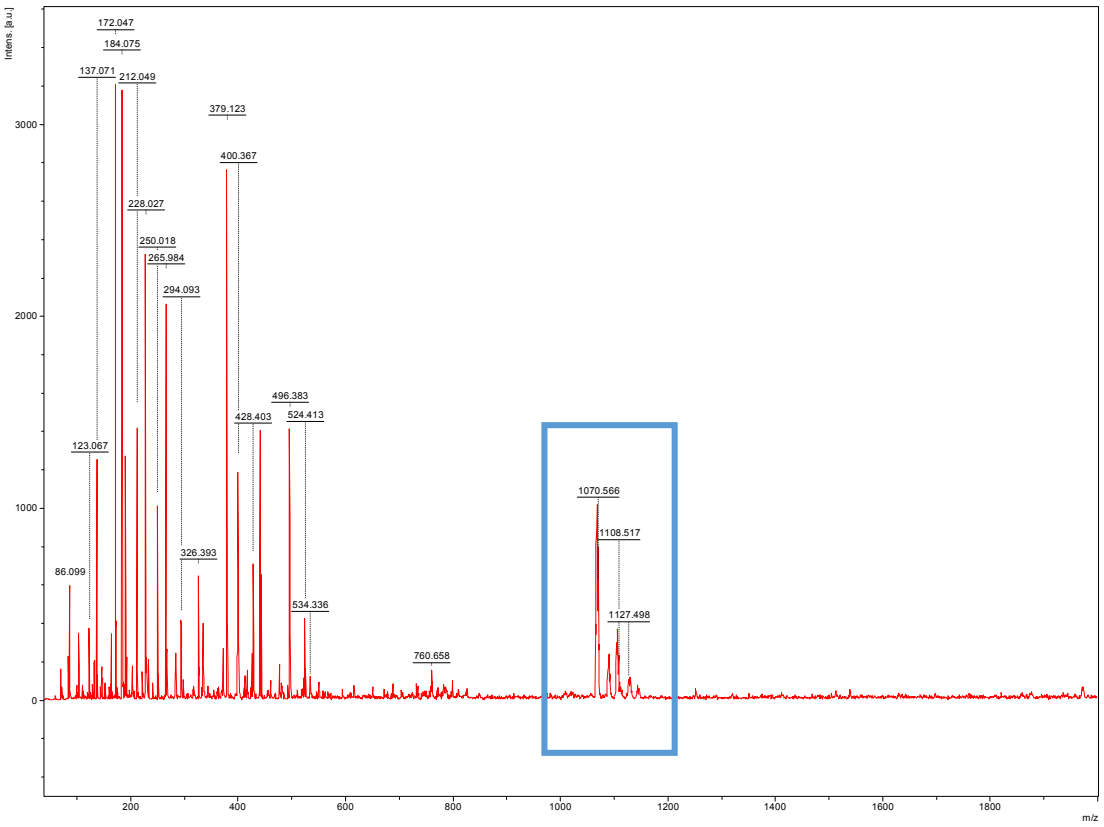
Intens. [a.u.]
172.047
184.075
137.071
212.049
379.123
400.367
228.027
250.018
265.984
294.093
496.383
428.403
524.413
123.067
1070.566
1108.517
326.393
86.099
534.336
1127.498
760.658
m/z

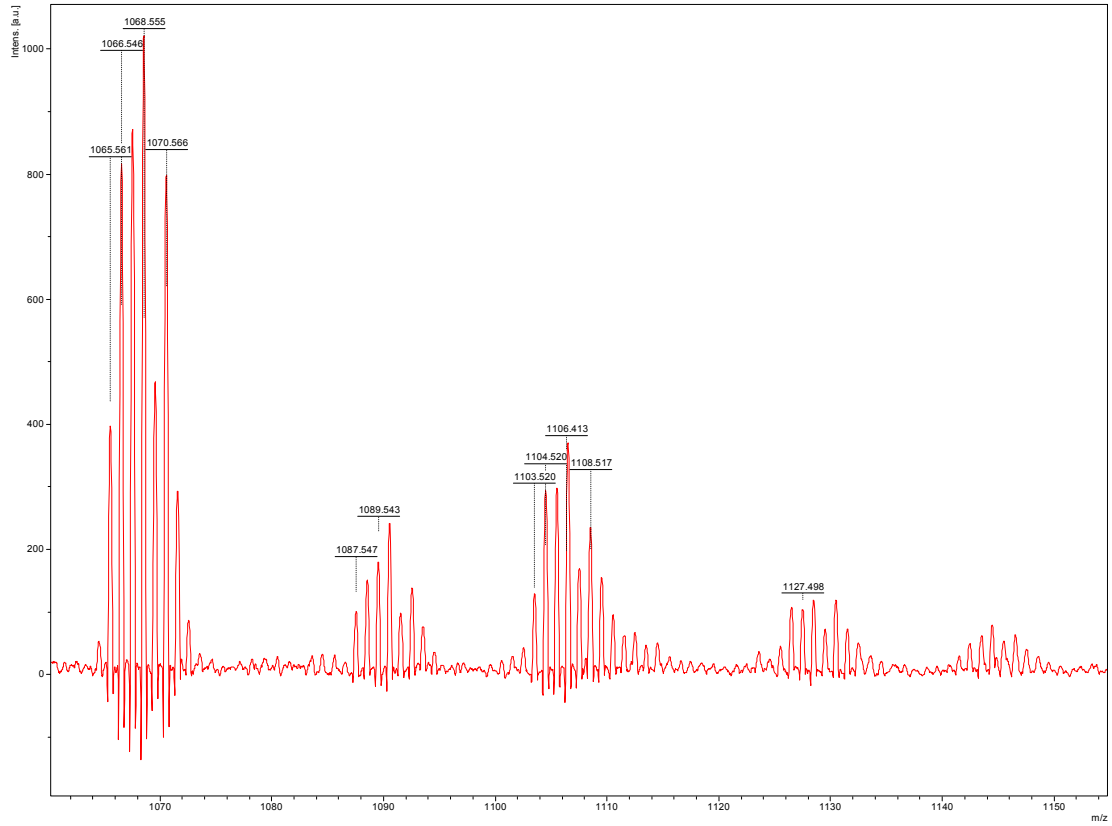
Intens. [a.u.]
1068.555
1066.546
1065.561
1070.566
1106.413
1104.520
1108.517
1103.520
1089.543
1087.547
1127.498
m/z

Fig 4.8. Mass spectrum of homogenized A549 tumor containing Gd-DOTA-APC in CHCA showing Gd from 0-2000 *m/z*. The zoomed in view of Gd-DOTA-APC and its adducts shown below.

APC Chelates of Diagnostic PET Imaging

To demonstrate the versatility of the new class of APC chelates, ^{64}Cu was conjugated to DOTA-APC and imaged in multiple models of cancer. ^{64}Cu-DOTA-APC were then injected into mice harboring U87MG, 4T1, and HCT-116 tumors (Figure 4.9). Imaging at 3hr, 24hr, and 48hr demonstrated uptake of the agent by 3hr and prolonged retention in the tumor up until 48hr. Due to the short decay half-life of ^{64}Cu, imaging at time points beyond 48hr was not feasible. These experiments offer proof-of-principle evidence that other PET isotopes can be applied to APC chelate technology. Other more suitable radioisotopes for PET imaging chelated to DOTA-APC are currently being pursued.

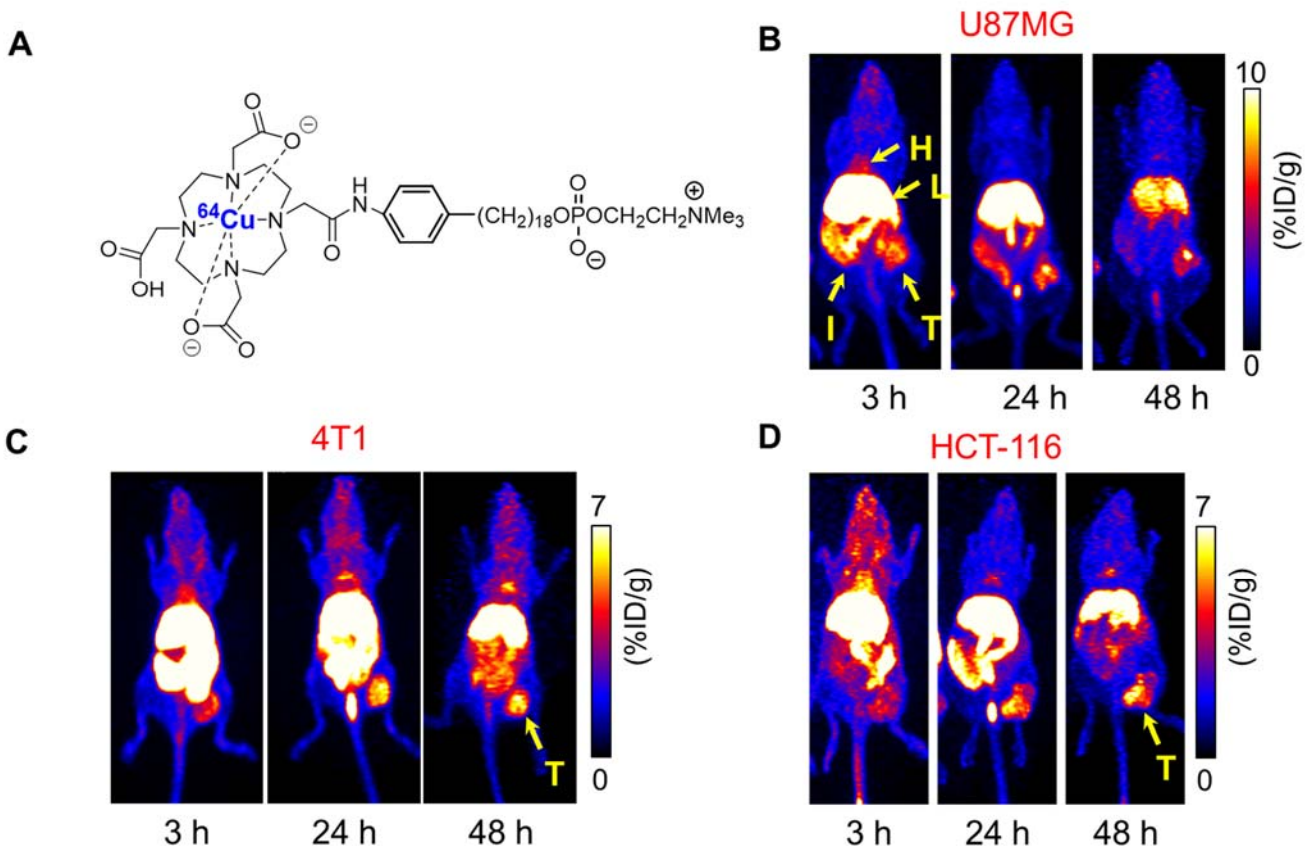

Figure 4.9. Broad-spectrum targeting of 64Cu-DOTA-APC in flank xenograft models. (A) Structure of 64Cu-DOTA-APC. Nude athymic mice harboring U87MG (n=3) (B), (C) Balb/c mice harboring murine breast cancer 4T1 (n=3), and nude athymic mice harboring (D) HCT-116 (n=3) were administered a single bolus dose of 250μCi 64Cu-DOTA-APC and imaged using positron emission tomography.

APC chelates for Targeted Radiotherapy

Radioisotopes for therapy such as ^{177}Lu can be chelated to DOTA-APC. In this proof-of-concept study, a single bolus dose of 500μCi of ^{177}Lu-DOTA-APC was injected into mice harboring 4T1 murine flank xenografts. Planar imaging at 48hr and 96hr were performed (Figure 4.10A and 4.10B), and demonstrated tumor uptake and prolonged retention of the ^{177}Lu-DOTA-APC. Three animals were sacrificed at each time-point, 48hr and 96hr, and biodistribution of the radioisotope was performed by tissue gamma-counting. Tumor growth was monitored in control mice (n=5) that received unchelated

DOTA-APC, and in mice receiving the single bolus injection of the ^{177}Lu-DOTA-APC (n=10). One-way ANOVA of the control and treatment groups demonstrated that the treatment group tumors were significantly smaller in size 4 days after initial administration, and continued to be significantly smaller in size up to12 days, at which point analysis was halted due to the large volumes of the tumors in the control group. This experiment offers proof-of-concept evidence that APC chelates represent a delivery platform for targeted radiotherapy as well as diagnostic PET imaging.

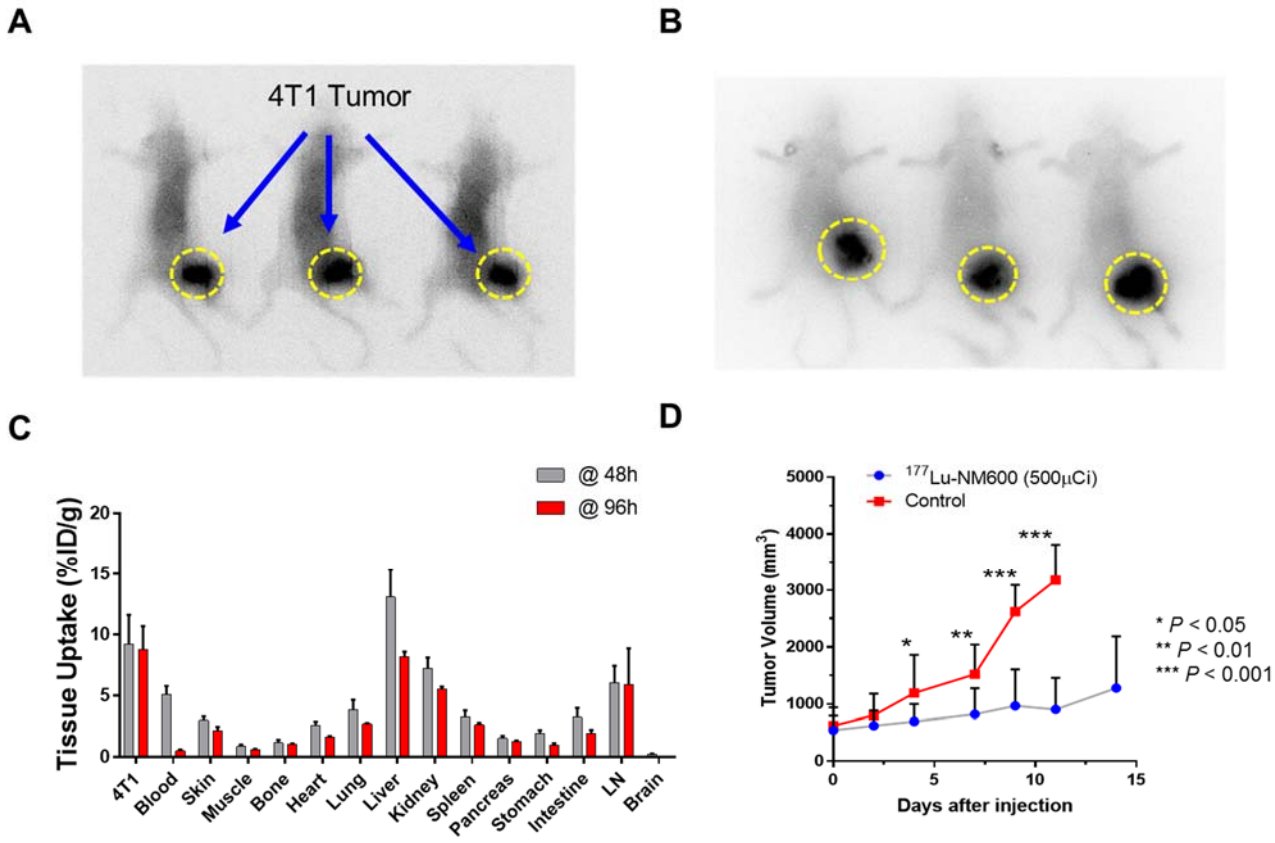

Figure 4.10. Biodistribution of ^{177}Lu-DOTA-APC and tumor growth. Balb/c mice harboring murine breast cancer 4T1 (n=5 in Control, n=10 in therapy group) were administered a single bolus dose of 500μCi ^{177}Lu-DOTA-APC or unchelated DOTA-APC at equivalent mass dose. (A-B) Planar images of the animals at 48hr and 96 hr. Yellow arrows indicate tumor. (C) Biodistribution of ^{177}Lu in various organs at 48hr and 96 hr. (D) Tumor volumes days after injection of the single bolus dose. Data are mean tumor volumes ± SEM. P values for tumor growth curves determined by one-way repeated-measurement ANOVA.

4D Discussion

In this preliminary study, we report a new cancer-targeted MR contrast agent that demonstrates tumor-specific uptake on T1-weighted images in all models that have been tested thus far, including 7 flank xenografts of different cancers and 2 orthotopic models. This APC chelate demonstrates broad selectivity for different cancers, similar to previous radioiodinated APC analogs. These previous analogs exhibited tumor avidity in over 55 models of human cancer, including transgenic, spontaneous, orthotopic and xenograft models, and are now being evaluated in clinical trials[2]. Importantly, with this new Gd^{3+}-labeled agent, we observed high intracellular uptake in endosomes on TEM imaging and identified a unique mechanism of selective uptake and retention through classical fluid-phase endocytosis. Together with TEM results, the high levels of uptake seen with this agent suggests a non-receptor mediated uptake mechanism that is amenable to delivery of high amounts of agent into tumor cells. To the best of our knowledge, this is the first time that this mechanism of endosomal transport has been demonstrated for alkylphosphocholine analogs, and it indicates increased potential for molecular MRI compared to saturable targeting mechanisms. Future studies will aim to identify key differences in the mechanism of uptake between malignant cells and normal cells to elucidate a unique and near-universal cancer targeting mechanism. An understanding of this selective mechanism of uptake may lead to the identification of new classes of cancer targeting compounds for imaging and therapeutic applications in a broad spectrum of cancer types.

In addition to being one of the first broad-spectrum cancer-targeted MR agents, Gd-DOTA-APC demonstrates impressive longitudinal relaxivity in plasma and water at

1.5T and 3.0T, which are 2-8 times higher than commercial extracellular Gd^{3+} agents[77]. This new targeted agent with favorable relaxivity characteristics can address the historical mismatch between the high spatial resolution of MRI and the low sensitivity of the imaging modality. The impressive spatial resolution and soft-tissue contrast of MRI may translate to improved diagnostic accuracy of tumors and metastases in head and neck, brain, spinal cord, breast, liver pelvic regions, and muscuoskeletal regions, where MR is the preferred imaging modality[97].

Importantly, we have synthesized and validated a tumor-specific macrocylic Gd chelate with higher relaxivities than commercial chelates and higher stability than the linear Gd chelates such as MultiHance (Gd BOPTA). The high relaxivities of MultiHance (6.3-7.9mM/s at 1.5T) offer improved diagnostic accuracy and improved contrast to noise ratio in many sites of malignancies over other commercial chelates, as well as lower doses of administration[77]. Some studies have shown that high relativities are important for detecting malignancies, and even higher concentrations of a lower relaxivity agent does not improve the contrast to the same degree[98,99]. For these reasons, radiologists prefer MultiHance over other commercial agents for the purposes of lesion enhancement[100]. However, as linear chelates have been shown to deposit in the dentate nucleus and globus pallidus, safety concerns over the linear chelates has spurred European agencies in suspending the use of the linear chelates[86,87]. The creation of a macrocyclic, tumor-specific chelate with higher relaxivities and higher stabilities than any of the linear chelates may successfully and safely fill in the gap for detection of malignancies in soft tissue areas and avoid the potential concerns of the linear chelates. This agent may have the additional benefit of being highly sensitive and specific, as this

agent's mechanism of action is not from non-specific pooling in the vasculature, but through cancer-selective uptake as demonstrated on TEM imaging. In addition, even lower doses and shorter scanning times can be achieved with this agent due to its high relaxivities compared to the current gold standard MultiHance. Furthermore, this new agent exhibits a favorable time window for cancer imaging. Signal enhancement was seen as early as 1 hour and as prolonged as 7 days (Figure 4). This pharmacokinetic profile may decrease the need for repeat administration and increase flexibility in clinical applications. These characteristics may prove useful for MRI-guided therapies that are currently limited by clinical agents that clear more quickly from the tumors[101,102] (Figure 4.4).

We have also developed a novel method to analyze the deposited chemical species in different tissues of interest. As proof-of-concept, we used MALDI-TOF to distinguish between different Gd chelates including Dotarem, Multihance, and Gd-DOTA-APC. In addition, we also analyzed tumor tissue homogenate in animals injected Gd-DOTA-APC. In both U87 and A549 flank xenografts, Gd-DOTA-APC was detected using MALDI-MS at 24h and 72h post contrast administration. Furthermore, we do not see the characteristic Gd isotopic fingerprint in any other chemical species other from that of the compound itself, suggesting that the compound is stable inside the tumor up to 72hr post administration. Future work will utilize this methodology to interrogate the behavior and deposition of Gd species that may result from our compound. Importantly, this methodology can be immediately applied to resolve the chemical form of deposited Gd in the dentate nucleus and globus pallidus.

Finally, we demonstrate the versatility of these new APC chelates through multimodality imaging. We observe similar pharmacokinetics and uptake in a U87 flank xenograft on simultaneous PET/MR agent with ^{64}Cu-DOTA-APC and Gd-DOTA-APC even though the Gd-DOTA-APC was given at >1000 the mass dose of the PET agent. This observation is non-trivial as most receptor-mediated drug delivery agents are limited in their multimodality imaging potential. The most highly expressed receptors are expressed at densities lower than a million per cell and saturation of those receptors with large doses of MR targeted agents would likely prevent other agents given at much lower doses from binding to those same receptors[103,104]. Again, this suggests a mechanism of non-receptor mediated uptake that can be exploited for delivering large quantities of APC to the sites of malignancies. Due to the versatility of these chelates, other MR active metals such as manganese and other radiometals for imaging and therapy are feasible for multi-modality imaging and therapy purposes, and are currently being investigated.

The successful demonstration of simultaneous PET and MR with our two agents may help improve the diagnostic accuracy and flexibility of cancer detection. There have been several studies that illustrate the improved diagnostic accuracy of cancer with PET/MR in soft tissue areas[75]. Tatsumi *et al.* retrospectively compared ^{18}F-FDG PET/CT with ^{18}F PET/MR in 47 patients suspected of having or known to have pancreatic cancer[97]. T1-weighted PET/MR revealed the highest diagnostic accuracy (93.0%) compared to PET/CT (88.4%). In another study prospectively comparing ^{124}I-PET/CT and ^{124}I-PET/MR for diagnosis of thyroid remnant tissue and lymph node metastases in patients with high-risk differentiated thyroid carcinoma revealed 23 lesions that were not discernable by PET/CT but discernable by PET/MR[105]. Of these, 15 lesions were smaller than 10mm in

diameter, illustrating the superior diagnostic accuracy of PET/MR especially in smaller tumors. Multimodality imaging with a targeted PET and MR agent that have the same pharmacokinetics may even further improve the sensitivity and specificity of detection of malignancies in soft tissues. In combination, targeted MR imaging may help localize cancer and resolve ambiguous findings especially in submillimeter tumors where PET is limited in its resolution. Additionally, the higher sensitivity of PET may help resolve ambiguity on MRI when the contrast is more limited due to its lower sensitivity. Together, targeted PET and targeted MR with our broad-spectrum cancer targeting APC chelates can be employed to further improve the diagnostic accuracy of cancer detection.

4E Conclusion

We have created one of the first broad-spectrum tumor-targeted MR agents for molecular MRI. Gd-DOTA-APC demonstrates high relaxivities and favorable tumor uptake and retention kinetics. This agent has great potential to bridge the historical mismatch of MRI's superior spatial resolution but limited sensitivity compared to PET's high sensitivity and low spatial resolution. Importantly, we have demonstrated a unique cancer-targeting mechanism of these APC chelates that is not receptor mediated and has thus far proven to be selective for a broad array of cancers. The versatility of these new APC chelates and the unique mechanism of non-saturable uptake allow for multi-modality imaging capabilities. Through the creation of a broad-spectrum targeted MR agent, we may improve the prognoses and survival of cancer patients by improving the diagnostic accuracy detection of malignancies.

Chapter 5: **Concluding Remarks and Future Directions**

Radiodine-labeled alkylphosphocholines have shown great promise as diagnostic imaging and targeted radiotherapy agents for a broad array of different cancer types and are currently in clinical trials testing[2,4]. In addition to their broad selectivity for many types of cancers, the PET imaging agent ^{124}I-NM404 has shown significant advantages over traditional agents like ^{18}F-FDG by avoiding areas of inflammation[2]. The sensitivity and specificity, and broad tumor selectivity offers considerable advantages of the radioiodinated APCs compared to other cancer targeting agents.

Due to their initial success, we proceeded to synthesize and validate next generation APC analogs for multi-modality imaging and therapy of cancer through substitution of bulkier substituents in place of the radioiodine. As part of the thesis work, we have synthesized and validated near-infrared fluorescent APCs, dual modality PET/fluorescent APCs, and APC chelates that greatly extend the multimodality imaging and therapy potential of these APC analogs. Importantly, we have shown that the broad uptake and retention for numerous cancer types of these new APC analogs are maintained in these new APC analogs.

With the expanded arsenal of different APC analogs for multimodality imaging and therapy, we may realize the potential of personalized management and treatment of cancer through the use of different APC analogs throughout each phase of patient care tailored to the unique needs of each cancer patient. Patients can be initially staged with the PET APC chelates or ^{124}I-NM404 and even MR APCs such as Gd-DOTA-APC for localization of soft tissue lesions. This can be followed by surgical resection of non-disseminated disease with the fluorescent APCs, illuminating surgical margins in the

operating room. Imaging with PET or MR APCs to post-operatively evaluate the residual disease and extent of resection. Treatment of cancer patients who do not qualify for surgery or post-adjuvant treatment with a targeted radiotherapy can be uniquely tailored by using a variety of radiotherapy analogs including ^{131}I-NM404, ^{177}Lu-DOTA-APC or ^{90}Y-DOTA-APC. This personalized diapeutic approach to cancer treatment and management is achievable due to the purported identical mechanism of uptake and retention conferred by the same targeting APC backbone, which ensures successful targeting that can be easily evaluated on diagnostic imaging in the first phases of care.

Future work will encompass continued synthesis and validation of new APC analogs including the dual-modality analogs and the new class of APC chelates. In addition to the synthesis and validation of the tumor targeting, a better understanding of how the structure impacts the tumor-targeting and other ADME properties is a continued interest this will allow optimization of the lead compounds that are most likely to be successful clinically. A more nuanced understanding of the mechanism of action of these APC analogs can lead to the discovery of cancer-targeting strategies that are shared in many different types of cancers. These avenues will continue to be explored by the Weichert lab and many close collaborators.

References

1 Pinchuk, A. N. *et al.* Synthesis and Structure−Activity Relationship Effects on the Tumor Avidity of Radioiodinated Phospholipid Ether Analogues. *Journal of Medicinal Chemistry* **49**, 2155-2165, doi:10.1021/jm050252g (2006).

2 Weichert, J. P. *et al.* Alkylphosphocholine analogs for broad-spectrum cancer imaging and therapy. *Science translational medicine* **6**, 240ra275-240ra275 (2014).

3 van Blitterswijk, W. J. & Verheij, M. Anticancer mechanisms and clinical application of alkylphospholipids. *Biochimica et Biophysica Acta (BBA)-Molecular and Cell Biology of Lipids* **1831**, 663-674 (2013).

4 Lubner, S. J. *et al.* A Phase 1, Multi-Center, Open-Label, Dose-Escalation Study of 131I-NM404 in Subjects with Relapsed or Refractory Advanced Solid Malignancies. *Cancer investigation* **33**, 483-489 (2015).

5 Grudzinski, J. J. *et al.* A Phase 1 Study of ¹³¹I-NM404 in Patients with Relapsed or Refractory Advanced Solid Tumors: Dosimetry, Biodistribution, Pharmacokinetics, and Safety. *PLoS ONE* **9**, e111652, doi:10.1371/journal.pone.0111652 (2014).

6 Chao, S. T., Suh, J. H., Raja, S., Lee, S.-Y. & Barnett, G. The sensitivity and specificity of FDG PET in distinguishing recurrent brain tumor from radionecrosis in patients treated with stereotactic radiosurgery. *International Journal of Cancer* **96**, 191-197, doi:10.1002/ijc.1016 (2001).

7 Kelloff, G. J. *et al.* Progress and Promise of FDG-PET Imaging for Cancer Patient Management and Oncologic Drug Development. *Clinical Cancer Research* **11**, 2785-2808, doi:10.1158/1078-0432.ccr-04-2626 (2005).

8 Hegi, M. E. *et al.* Clinical Trial Substantiates the Predictive Value of O-6-Methylguanine-DNA Methyltransferase Promoter Methylation in Glioblastoma Patients Treated with Temozolomide. *Clinical Cancer Research* **10**, 1871-1874, doi:10.1158/1078-0432.ccr-03-0384 (2004).

9 Nicolaides, N. C., O'shannessy, D. J., Albone, E. & Grasso, L. Co-development of diagnostic vectors to support targeted therapies and theranostics: Essential tools in Personalized Cancer Therapy. *Frontiers in Oncology* **4**, doi:10.3389/fonc.2014.00141 (2014).

10 Zhang, R. R., Swanson, K. I., Hall, L. T., Weichert, J. P. & Kuo, J. S. Diapeutic cancer-targeting alkylphosphocholine analogs may advance management of brain malignancies. *CNS oncology* **5**, 223-231 (2016).

11 Ramogida, C. F. & Orvig, C. Tumour targeting with radiometals for diagnosis and therapy. *Chemical Communications* **49**, 4720-4739 (2013).

12 Swanson, K. I. *et al.* Fluorescent cancer-selective alkylphosphocholine analogs for intraoperative glioma detection. *Neurosurgery* **76**, 115 (2015).

13 Korb, M. L. *et al.* Breast Cancer Imaging Using the Near-Infrared Fluorescent Agent, CLR1502. *Molecular imaging* **13**, 1-9 (2014).

14 Deming, D. A. *et al.* Phospholipid ether analogs for the detection of colorectal tumors. (2014).

15 Hafeez, B. B. *et al.* Genetic Ablation of PKC Epsilon Inhibits Prostate Cancer Development and Metastasis in Transgenic Mouse Model of Prostate Adenocarcinoma. *Cancer Research* **71**, 2318-2327, doi:10.1158/0008-5472.can-10-4170 (2011).

16 Benet, L. Z., Kroetz, D., Sheiner, L., Hardman, J. & Limbird, L. Pharmacokinetics: the dynamics of drug absorption, distribution, metabolism, and elimination. *Goodman and Gilman's the pharmacological basis of therapeutics*, 3-27 (1996).

17 Bohnert, T. & Gan, L. S. Plasma protein binding: from discovery to development. *Journal of pharmaceutical sciences* **102**, 2953-2994 (2013).

18 Knox, S. J. *et al.* Yttrium-90-labeled anti-CD20 monoclonal antibody therapy of recurrent B-cell lymphoma. *Clinical Cancer Research* **2**, 457-470 (1996).

19 Kaminski, M. S. *et al.* Radioimmunotherapy of B-cell lymphoma with [131I] anti-B1 (anti-CD20) antibody. *New England Journal of Medicine* **329**, 459-465 (1993).

20 Lane, D. *et al.* Radioimmunotherapy of metastatic colorectal tumours with iodine-131-labelled antibody to carcinoembryonic antigen: phase I/II study with comparative biodistribution of intact and F (ab') 2 antibodies. *British journal of cancer* **70**, 521 (1994).

21 Steiner, M. & Neri, D. Antibody-radionuclide conjugates for cancer therapy: historical considerations and new trends. *Clinical Cancer Research* **17**, 6406-6416 (2011).

22 Hutchinson, L. & Kirk, R. (Nature Publishing Group, 2011).

23 Kennedy, T. Managing the drug discovery/development interface. *Drug discovery today* **2**, 436-444 (1997).

24 Van De Waterbeemd, H. & Gifford, E. ADMET in silico modelling: towards prediction paradise? *Nature reviews Drug discovery* **2**, 192-204 (2003).

25 van de Waterbeemd, H., Smith, D. A. & Jones, B. C. Lipophilicity in PK design: methyl, ethyl, futile. *J Comput Aided Mol Des* **15**, 273-286 (2001).

26 Kitchen, D. B., Decornez, H., Furr, J. R. & Bajorath, J. Docking and scoring in virtual screening for drug discovery: methods and applications. *Nat Rev Drug Discov* **3**, 935-949, doi:http://www.nature.com/nrd/journal/v3/n11/suppinfo/nrd1549_S1.html (2004).

27 Colmenarejo, G. In silico prediction of drug-binding strengths to human serum albumin. *Medicinal research reviews* **23**, 275-301 (2003).

28 Zhang, R. R. *et al.* Beyond the margins: real-time detection of cancer using targeted fluorophores. *Nat Rev Clin Oncol* **advance online publication**, doi:10.1038/nrclinonc.2016.212

http://www.nature.com/nrclinonc/journal/vaop/ncurrent/abs/nrclinonc.2016.212.html#supplementary-information (2017).

29 Guo, S. *et al.* Structural basis of transport of lysophospholipids by human serum albumin. *Biochemical Journal* **423**, 23-30, doi:10.1042/bj20090913 (2009).

30 Kelley, E. E., Modest, E. J. & Burns, C. P. Unidirectional membrane uptake of the ether lipid antineoplastic agent edelfosine by L1210 cells. *Biochemical Pharmacology* **45**, 2435-2439, doi:http://dx.doi.org/10.1016/0006-2952(93)90224-K (1993).

31 Jiang, H. *et al.* Quantification of CLR1401, a novel alkylphosphocholine anticancer agent, in rat plasma by hydrophilic interaction liquid chromatography–tandem

mass spectrometric detection. *Journal of Chromatography B* **878**, 1513-1518 (2010).

32 Ashbrook, J. D., Spector, A. A., Santos, E. C. & Fletcher, J. E. Long chain fatty acid binding to human plasma albumin. *Journal of Biological Chemistry* **250**, 2333-2338 (1975).

33 Bhattacharya, A. A., Grüne, T. & Curry, S. Crystallographic analysis reveals common modes of binding of medium and long-chain fatty acids to human serum albumin1. *Journal of Molecular Biology* **303**, 721-732, doi:http://dx.doi.org/10.1006/jmbi.2000.4158 (2000).

34 Curry, S., Brick, P. & Franks, N. P. Fatty acid binding to human serum albumin: new insights from crystallographic studies. *Biochimica et Biophysica Acta (BBA) - Molecular and Cell Biology of Lipids* **1441**, 131-140, doi:http://dx.doi.org/10.1016/S1388-1981(99)00148-1 (1999).

35 Curry, S., Mandelkow, H., Brick, P. & Franks, N. Crystal structure of human serum albumin complexed with fatty acid reveals an asymmetric distribution of binding sites. *Nat Struct Mol Biol* **5**, 827-835 (1998).

36 He, X. M. & Carter, D. C. Atomic structure and chemistry of human serum albumin. *Nature* **358**, 209-215 (1992).

37 Petitpas, I., Grüne, T., Bhattacharya, A. A. & Curry, S. Crystal structures of human serum albumin complexed with monounsaturated and polyunsaturated fatty acids1. *Journal of Molecular Biology* **314**, 955-960, doi:http://dx.doi.org/10.1006/jmbi.2000.5208 (2001).

38 Richieri, G. V., Anel, A. & Kleinfeld, A. M. Interactions of long-chain fatty acids and albumin: Determination of free fatty acid levels using the fluorescent probe ADIFAB. *Biochemistry* **32**, 7574-7580, doi:10.1021/bi00080a032 (1993).

39 Choi, J.-K. *et al.* Interactions of very long-chain saturated fatty acids with serum albumin. *Journal of Lipid Research* **43**, 1000-1010, doi:10.1194/jlr.M200041-JLR200 (2002).

40 Ho, J. K., Moser, H., Kishimoto, Y. & Hamilton, J. A. Interactions of a very long chain fatty acid with model membranes and serum albumin. Implications for the pathogenesis of adrenoleukodystrophy. *Journal of Clinical Investigation* **96**, 1455-1463 (1995).

41 Weichert, J. P., Van Dort, M. E., Groziak, M. P. & Counsell, R. E. Radioiodination via isotope exchange in pivalic acid. *International Journal of Radiation Applications and Instrumentation. Part A. Applied Radiation and Isotopes* **37**, 907-913 (1986).

42 Chung, B. H., Wilkinson, T., Geer, J. C. & Segrest, J. P. Preparative and quantitative isolation of plasma lipoproteins: rapid, single discontinuous density gradient ultracentrifugation in a vertical rotor. *Journal of Lipid Research* **21**, 284-291 (1980).

43 Barré, J., Chamouard, J. M., Houin, G. & Tillement, J. P. Equilibrium dialysis, ultrafiltration, and ultracentrifugation compared for determining the plasma-protein-binding characteristics of valproic acid. *Clinical Chemistry* **31**, 60-64 (1985).

44 Rodríguez-Sureda, V. c., Julve, J., Llobera, M. & Peinado-Onsurbe, J. Ultracentrifugation Micromethod for Preparation of Small Experimental Animal

Lipoproteins. *Analytical Biochemistry* **303**, 73-77, doi:http://dx.doi.org/10.1006/abio.2001.5546 (2002).

45 Waters, N. J., Jones, R., Williams, G. & Sohal, B. Validation of a rapid equilibrium dialysis approach for the measurement of plasma protein binding. *Journal of Pharmaceutical Sciences* **97**, 4586-4595, doi:10.1002/jps.21317 (2008).

46 Seeliger, D. & de Groot, B. Ligand docking and binding site analysis with PyMOL and Autodock/Vina. *J Comput Aided Mol Des* **24**, 417-422, doi:10.1007/s10822-010-9352-6 (2010).

47 Trott, O. & Olson, A. J. AutoDock Vina: Improving the speed and accuracy of docking with a new scoring function, efficient optimization, and multithreading. *Journal of Computational Chemistry* **31**, 455-461, doi:10.1002/jcc.21334 (2010).

48 Fischer, G., Wilson, S., Hunter, K. & Mease, A. Diminished bacterial defences with intralipid. *The Lancet* **316**, 819-820 (1980).

49 Vuong, T. D. *et al.* Hypoalbuminemia increases lysophosphatidylcholine in low-density lipoprotein of normocholesterolemic subjects. *Kidney Int* **55**, 1005-1010 (1999).

50 Brocks, D. R. & Wasan, K. M. The influence of lipids on stereoselective pharmacokinetics of halofantrine: Important implications in food-effect studies involving drugs that bind to lipoproteins. *Journal of Pharmaceutical Sciences* **91**, 1817-1826, doi:10.1002/jps.10182 (2002).

51 Brocks, D. R., Ala, S. & Aliabadi, H. M. The effect of increased lipoprotein levels on the pharmacokinetics of cyclosporine A in the laboratory rat. *Biopharmaceutics & drug disposition* **27**, 7-16 (2006).

52 Su, J., He, L., Zhang, N. & Ho, P. C. Evaluation of Tributyrin Lipid Emulsion with Affinity to Low-Density Lipoprotein: Pharmacokinetics in Adult Male Wistar Rats and Cellular Activity on Caco-2 and HepG2 Cell Lines. *Journal of Pharmacology and Experimental Therapeutics* **316**, 62-70, doi:10.1124/jpet.105.090464 (2006).

53 Sleep, D., Cameron, J. & Evans, L. R. Albumin as a versatile platform for drug half-life extension. *Biochimica et Biophysica Acta (BBA) - General Subjects* **1830**, 5526-5534, doi:http://dx.doi.org/10.1016/j.bbagen.2013.04.023 (2013).

54 Shah, A. K. & Sawchuk, R. J. Effect of co-administration of intralipidTM on the pharmacokinetics of cyclosporine in the rabbit. *Biopharmaceutics & drug disposition* **12**, 457-466, doi:10.1002/bdd.2510120607 (1991).

55 Rosenthal, E. L. *et al.* Successful Translation of Fluorescence Navigation During Oncologic Surgery: A Consensus Report. *Journal of Nuclear Medicine* **57**, 144-150 (2016).

56 Rosenthal, E. L., Warram, J. M., Bland, K. I. & Zinn, K. R. The status of contemporary image-guided modalities in oncologic surgery. *Annals of surgery* **261**, 46-55 (2015).

57 Michel Lacroix *et al.* A multivariate analysis of 416 patients with glioblastoma multiforme: prognosis, extent of resection, and survival. *Journal of Neurosurgery* **95**, 190-198, doi:doi:10.3171/jns.2001.95.2.0190 (2001).

58 Matthew J. McGirt *et al.* Independent association of extent of resection with survival in patients with malignant brain astrocytoma. *Journal of Neurosurgery* **110**, 156-162, doi:doi:10.3171/2008.4.17536 (2009).

59 McGirt, M. J. *et al.* EXTENT OF SURGICAL RESECTION IS INDEPENDENTLY ASSOCIATED WITH SURVIVAL IN PATIENTS WITH HEMISPHERIC INFILTRATING LOW-GRADE GLIOMAS. *Neurosurgery* **63**, 700-708, doi:10.1227/01.neu.0000325729.41085.73 (2008).

60 Stummer, W. *et al.* Fluorescence-guided surgery with 5-aminolevulinic acid for resection of malignant glioma: a randomised controlled multicentre phase III trial. *The Lancet Oncology* **7**, 392-401, doi:http://dx.doi.org/10.1016/S1470-2045(06)70665-9 (2006).

61 Hope-Ross, M. *et al.* Adverse Reactions due to Indocyanine Green. *Ophthalmology* **101**, 529-533, doi:http://dx.doi.org/10.1016/S0161-6420(94)31303-0 (1994).

62 Marshall, M., Draney, D., Sevick-Muraca, E. & Olive, D. M. Single-Dose Intravenous Toxicity Study of IRDye 800CW in Sprague-Dawley Rats. *Molecular Imaging and Biology* **12**, 583-594, doi:10.1007/s11307-010-0317-x (2010).

63 Marshall, M. V. *et al.* Near-Infrared Fluorescence Imaging in Humans with Indocyanine Green: A Review and Update. *Open surgical oncology journal (Online)* **2**, 12-25, doi:10.2174/1876504101002010012 (2010).

64 Obana, A. *et al.* Survey of complications of indocyanine green angiography in Japan. *American journal of ophthalmology* **118**, 749-753 (1994).

65 Zhu, B. & Sevick-Muraca, E. A review of performance of near-infrared fluorescence imaging devices used in clinical studies. *The British journal of radiology* **88**, 20140547 (2014).

66 Mondal, S. B. *et al.* Real-time fluorescence image-guided oncologic surgery. *Advances in cancer research* **124**, 171 (2014).

67 Chi, C. *et al.* Intraoperative imaging-guided cancer surgery: from current fluorescence molecular imaging methods to future multi-modality imaging technology. *Theranostics* **4**, 1072-1084 (2014).

68 Swanson, K. I. *et al.* Fluorescent Cancer-Selective Alkylphosphocholine Analogs for Intraoperative Glioma Detection. *Neurosurgery* **76**, 115-124, doi:10.1227/neu.0000000000000622 (2015).

69 Frangioni, J. V. In vivo near-infrared fluorescence imaging. *Current Opinion in Chemical Biology* **7**, 626-634, doi:http://dx.doi.org/10.1016/j.cbpa.2003.08.007 (2003).

70 Kusumi, A. *et al.* in *Seminars in cell & developmental biology.* 126-144 (Elsevier).

71 Deming, D. A. *et al.* Phospholipid Ether Analogs for the Detection of Colorectal Tumors. *PLoS ONE* **9**, e109668, doi:10.1371/journal.pone.0109668 (2014).

72 Moses, W. W. Fundamental limits of spatial resolution in PET. *Nuclear Instruments and Methods in Physics Research Section A: Accelerators, Spectrometers, Detectors and Associated Equipment* **648**, S236-S240 (2011).

73 Rudin, M. & Weissleder, R. Molecular imaging in drug discovery and development. *Nature reviews Drug discovery* **2**, 123-131 (2003).

74 Antoch, G. *et al.* Whole-body dual-modality PET/CT and whole-body MRI for tumor staging in oncology. *Jama* **290**, 3199-3206 (2003).

75 Torigian, D. A. *et al.* PET/MR imaging: technical aspects and potential clinical applications. *Radiology* **267**, 26-44 (2013).

76 Boss, A. *et al.* Hybrid PET/MRI of intracranial masses: initial experiences and comparison to PET/CT. *Journal of Nuclear Medicine* **51**, 1198-1205 (2010).

77 Rohrer, M., Bauer, H., Mintorovitch, J., Requardt, M. & Weinmann, H.-J. Comparison of magnetic properties of MRI contrast media solutions at different magnetic field strengths. *Investigative radiology* **40**, 715-724 (2005).

78 Caravan, P. Protein-targeted gadolinium-based magnetic resonance imaging (MRI) contrast agents: design and mechanism of action. *Accounts of chemical research* **42**, 851-862 (2009).

79 Sun, C., Sze, R. & Zhang, M. Folic acid-PEG conjugated superparamagnetic nanoparticles for targeted cellular uptake and detection by MRI. *Journal of Biomedical Materials Research Part A* **78**, 550-557 (2006).

80 Xue, S. *et al.* Protein MRI contrast agent with unprecedented metal selectivity and sensitivity for liver cancer imaging. *Proceedings of the National Academy of Sciences* **112**, 6607-6612, doi:10.1073/pnas.1423021112 (2015).

81 Caravan, P. Strategies for increasing the sensitivity of gadolinium based MRI contrast agents. *Chemical Society Reviews* **35**, 512-523 (2006).

82 Bulte, J. W. & Kraitchman, D. L. Iron oxide MR contrast agents for molecular and cellular imaging. *NMR in Biomedicine* **17**, 484-499 (2004).

83 Mollinedo, F. & Gajate, C. Lipid rafts as major platforms for signaling regulation in cancer. *Advances in biological regulation* **57**, 130-146 (2015).

84 Moore, D. A. Selective Trialkylation of Cyclen with tert-Butyl Bromoacetate. *Organic Syntheses*, 10-14 (2008).

85 El-Faham, A. & Albericio, F. COMU: A third generation of uronium-type coupling reagents. *Journal of Peptide Science* **16**, 6-9 (2010).

86 McDonald, R. J. *et al.* Intracranial gadolinium deposition after contrast-enhanced MR imaging. *Radiology* **275**, 772-782 (2015).

87 Kanda, T., Ishii, K., Kawaguchi, H., Kitajima, K. & Takenaka, D. High signal intensity in the dentate nucleus and globus pallidus on unenhanced T1-weighted MR images: relationship with increasing cumulative dose of a gadolinium-based contrast material. *Radiology* **270**, 834-841 (2013).

88 Frenzel, T., Lengsfeld, P., Schirmer, H., Hütter, J. & Weinmann, H.-J. Stability of gadolinium-based magnetic resonance imaging contrast agents in human serum at 37 C. *Investigative radiology* **43**, 817-828 (2008).

89 Morcos, S. Extracellular gadolinium contrast agents: differences in stability. *European journal of radiology* **66**, 175-179 (2008).

90 Radbruch, A. Are some agents less likely to deposit gadolinium in the brain? *Magnetic Resonance Imaging* **34**, 1351-1354 (2016).

91 Raju, C. S. K., Lück, D., Scharf, H., Jakubowski, N. & Panne, U. A novel solid phase extraction method for pre-concentration of gadolinium and gadolinium based MRI contrast agents from the environment. *Journal of Analytical Atomic Spectrometry* **25**, 1573-1580 (2010).

92 Kaksonen, M., Toret, C. P. & Drubin, D. G. Harnessing actin dynamics for clathrin-mediated endocytosis. *Nature reviews Molecular cell biology* **7**, 404-414 (2006).

93 Mayor, S. & Pagano, R. E. Pathways of clathrin-independent endocytosis. *Nature reviews Molecular cell biology* **8**, 603-612 (2007).

94 Gajate, C. & Mollinedo, F. Edelfosine and perifosine induce selective apoptosis in multiple myeloma by recruitment of death receptors and downstream signaling molecules into lipid rafts. *Blood* **109**, 711-719 (2007).

95 Gajate, C. & Mollinedo, F. The antitumor ether lipid ET-18-OCH3 induces apoptosis through translocation and capping of Fas/CD95 into membrane rafts in human leukemic cells. *Blood* **98**, 3860-3863 (2001).

96 Malin, D. *et al.* αB-crystallin: a Novel Regulator of Breast Cancer Metastasis to the Brain. *Clinical cancer research : an official journal of the American Association for Cancer Research* **20**, 56-67, doi:10.1158/1078-0432.CCR-13-1255 (2014).

97 Tatsumi, M. *et al.* 18F-FDG PET/MRI fusion in characterizing pancreatic tumors: comparison to PET/CT. *International journal of clinical oncology* **16**, 408-415 (2011).

98 Seidl, Z. *et al.* Does higher gadolinium concentration play a role in the morphologic assessment of brain tumors? Results of a multicenter intraindividual crossover comparison of gadobutrol versus gadobenate dimeglumine (the MERIT Study). *American Journal of Neuroradiology* **33**, 1050-1058 (2012).

99 Kanal, E., Maravilla, K. & Rowley, H. Gadolinium contrast agents for CNS imaging: current concepts and clinical evidence. *American Journal of Neuroradiology* **35**, 2215-2226 (2014).

100 Rowley, H. *et al.* Contrast-enhanced MR imaging of brain lesions: a large-scale intraindividual crossover comparison of gadobenate dimeglumine versus gadodiamide. *American Journal of Neuroradiology* **29**, 1684-1691 (2008).

101 Schenck, J. F. *et al.* Superconducting open-configuration MR imaging system for image-guided therapy. *Radiology* **195**, 805-814 (1995).

102 Jaffray, D. A. Image-guided radiotherapy: from current concept to future perspectives. *Nature Reviews Clinical Oncology* **9**, 688-699 (2012).

103 Bae, Y. S. *et al.* Epidermal growth factor (EGF)-induced generation of hydrogen peroxide Role in EGF receptor-mediated tyrosine phosphorylation. *Journal of Biological Chemistry* **272**, 217-221 (1997).

104 Wu, M., Gunning, W. & Ratnam, M. Expression of folate receptor type α in relation to cell type, malignancy, and differentiation in ovary, uterus, and cervix. *Cancer Epidemiology and Prevention Biomarkers* **8**, 775-782 (1999).

105 Nagarajah, J. *et al.* Diagnosis and dosimetry in differentiated thyroid carcinoma using 124I PET: comparison of PET/MRI vs PET/CT of the neck. *European journal of nuclear medicine and molecular imaging* **38**, 1862-1868 (2011).